Universidad del País Vasco
Euskal Herriko Unibertsitatea

Department of Systems Engineering and Automation

Doctoral Program in Control Engineering, Automation and Robotics

DOCTORAL THESIS

Design and Optimization of a Three Phase Inductive Power Transfer System

presented by:

Ugaitz Iruretagoyena Alustiza

Supervised by:

Prof. Haritza Camblong Ruiz (UPV-EHU)

Dr. Irma Villar Iturbe (IK4-IKERLAN)

2018

Acknowledgments

To be honest, I think that the decision of beginning this thesis that I took three years ago is the most important and life changing decision I have ever taken. At that time, Ion Etxeberria was the head of the Power Electronics Area at IK4-IKERLAN and gave me the opportunity to start this thrilling journey. After three months, I was send to Zürich for 6 months (it ended up being 8), to work with Roman Bosshard under the supervision of Prof. Kolar. I could not have imagined that I would learn so much and be so comfortable far from my home, family and friends. And yet, I met a lot of new friends there and even my girlfriend. I would like to thank each of you, that made that period possible and so great.

When I got back we had a new head of the department Unai. I also want to thank you, for helping me getting back to the wheel of IKERLAN. Thank to my initial PhD mates, Gus, DJ, Alejandro, Victor and a special thank to Andoni that helped me continuing when the mood was down, too down sometimes. And also a special thanks to Endi, one of my closest friends and college during the first years at IKERLAN.

Also thanks to the PhD students that started after me, Ander, Aitor and Fer. And to the students Lander, Unai and Aitor, for helping me with the prototypes. Many thanks to the power electronic department team, Jon, Amaia, Haizea, Sergio, Milo, Crego, Igor, Rafa, Asier, Alex, Karlos, Maitan, Valentin, Ander. Special thanks go to Victor and Atxur that helped me with their limitless wisdom, each one in his 'particular' way. Thanks also to the new department head Luis.

Many thanks to Prof. Haritza Camblong, that gave me the opportunity to begin this PhD.

I really really (is not a misspelling) want to thank my supervisor

at IKERLAN Irma Villar. Without your help this would not be possible. Not only technically but personally you have been an unbeatable supervisor.

I would like to thank also to my friends. Without knowing, you helped me getting my mind away from this thesis, so afterwards I could retake it again with renewed energy.

Finally, thanks to my new family in Uruguay. Thank you for making me feel at home at ten thousand kilometers far away. Last but not least, I would like to thank to my parents. You helped me all the time, in the good days in the bad days, did not matter. And most of all, I really want to thank my girlfriend Magda, I met you during this journey and you have become the most important person for me. You are the one that really knows how I am feeling in every time and you always have the right words to keep me up.

This words are too short to describe the gratitude that I feel.

Eskerrik asko danori,
Muchas gracias a todos,
Many thanks to all,
Vielen Dank an alle.
Ugaitz

Abstract

The concept of a sustainable transportation system within cities must be reconsidered in order to achieve healthier urban areas. Many cities are currently suffering from significant pollution problems. Mainly, due to the fact that private motor vehicles, with large CO_2 emissions, represent over the 50% of the modal share. Thus, it is clear that public transportation must be stimulated. Particularly talking, railway conveyance is very attractive, as no direct emissions are produced.

Railway transportation systems, such as trams and metros, are very advantageous in efficiency, user price, safety and comfort. However, compared to a vehicle, the initial and maintenances costs are very high. The high initial cost is mainly due to the high price of the batteries. On the other hand, the maintenance is enormously affected due to corrosion and environmental exposure that suffers part the power supply system, the pantograph and the catenaries, being these the most critical components. In addition in big cities with many tram lines, the overhead catenaries have a great visual impact. In order to ease these problems, one of the most promising solutions is to endow the railway vehicle with an Inductive Power Transfer (IPT) system. This way the catenary could be removed and the charing will be done wirelessly with the transmitter coils buried in the ground.

Between different possible IPT systems, this work is focused on Dynamic Inductive Power Transfer (DIPT) systems, i.e charging while the vehicle is moving. Particularly taking, this thesis delves in the design of meander type coils. The objective of this work is to propose a method for designing three-phase inductive charging systems. For that purpose, the fundamental working principles of IPT system is introduced in the first part of this thesis. The equations are presented and the pole-splitting limit are calculated. Validating them with a 3.3kW

prototype.

Afterwards, the meander type coil working principles are described. The equations that model this coils are shown and the possibility of achieving constant coupling with multiple phases is highlighted. Moreover, with the presented modifications, the multi-phase system can be modeled by an equivalent single-phase system. Thank to this, the pole-splitting limit can easily be calculated. Using this limit a design procedure is described and experimentally validated in a 50W prototype. This prototype shows the potential of this type of coils, achieving constant power transmission with an efficiency of 70%.

Based on this design procedure an optimization methodology is proposed, so as to improve the size, weight and cost of the DIPT. The trade-offs between these performance indicators are highlighted. Finally, this optimization is applied for a 9kW system and is validated in a real test bench with an efficiency of 90%, for any position and output power with a coil separation of 100mm.

Resumen

El concepto de transporte sostenible dentro de las ciudades debe ser reconsiderado para poder así tener áreas urbanas más saludables. Es un hecho bien conocido que en las grandes ciudades sufren de grandes problemas de contaminación. Principalmente, debido los vehículos de combustión interna, con grandes emisiones de CO_2. Estos representan más del 50% de los vehículos utilizados diariamente. Es por ello que el transporte público debe ser estimulado. Particularmente hablando, el transporte ferroviario es muy atractivo, ya que no se producen emisiones directas.

Los sistemas de transporte ferroviario, como los tranvías y los metros, son muy ventajosos en términos de eficiencia, precio del usuario, seguridad y comodidad. Sin embargo, en comparación con un vehículo de combustión interna, los costos iniciales y de mantenimiento son muy altos. El alto costo inicial se debe principalmente al alto precio de las baterías. Por otro lado, el mantenimiento se ve enormemente afectado por la corrosión y la exposición ambiental que sufre parte del sistema de alimentación, el pantógrafo y las catenarias, siendo estos los componentes más críticos. Además, en las grandes ciudades, con muchas líneas de tranvía, las catenarias tienen un gran impacto visual. Para solucionar estos problemas, una de las opciones más prometedoras es dotar al vehículo ferroviario de un sistema de transferencia inductiva (IPT). De esta forma, la catenaria podría eliminarse y la carga se realizará de forma inalámbrica con las bobinas del transmisor enterradas en el suelo.

Entre los diferentes sistemas posibles de IPT, este trabajo se centra en los sistemas de transferencia de energía inductiva dinámica (DIPT), es decir, cuando se está cargando mientras el vehículo se está moviendo. En concreto, esta tesis se adentra en el diseño de bobinas tipo meandro.

El objetivo de este trabajo es proponer un método para diseñar sistemas de carga inductiva trifásicos. Para ello, los principios fundamentales de funcionamiento del sistema IPT se introducen en la primera parte de esta tesis. Las ecuaciones se presentan y se calcula el límite de división de polos. Validándolos en un prototipo de 3.3kW.

Posteriormente, se describen los principios de trabajo de la bobina del tipo meandro. Se muestran las ecuaciones que modelan estas bobinas y se resalta la posibilidad de lograr un acoplamiento constante con múltiples fases. Además, con las modificaciones presentadas, el sistema multifásico se puede modelar mediante un sistema monofásico equivalente. Gracias a esto, el límite de división de polos se puede calcular fácilmente. Utilizando este límite, se describe un procedimiento de diseño y se valida experimentalmente en un prototipo de 50W. Este prototipo muestra el potencial de este tipo de bobinas, logrando una transmisión de potencia constante con una eficiencia del 70%.

Sobre la base de este procedimiento de diseño, se propone una metodología de optimización para mejorar el tamaño, el peso y el costo del DIPT. Se resaltan los compromisos existentes entre estos indicadores. Finalmente, esta optimización se aplica para un sistema de 9kW y se valida en un banco de prueba real, con una eficiencia medida del 90%, para cualquier posición y potencia de salida con una separación de bobina de 100mm.

Laburpena

Garraio jasangarriaren kontzeptua birplanteatu beharra dago hiri osasuntsuagoak lortzeko. Gaur egun poluzio arazo handiak jasaten hari baitira. Gehienbat, garraio pribatuak, CO_2 emisio handiekin, bidai guztien %50 suposatzen dutelako. Beraz, argi dago garraio publikoa sustatu beharra dagoela. Zehazki hitz eginda, bereziki tren garraioa sustatu beharra dago, isuri zuzenak ez bait ditu.

Trenbide garraioa, bai trenak bai metroak, oso onuragarriak dira efizientzia, erabiltzailearendako prezioa, segurtasuna eta erosotasunari dagokionez. Hala ere, barne errekuntzadun ibilgailu batekin alderatuz, hasierako eta mantentze kostuak oso altuak dira. Hasierako kostua gehienbat baterien prezio altuarengatik da. Bestalde, mantzea ikaragarri kaltetua ikusten da korrosioagatik eta ingurumenak zati batzuengan, pantografoa eta katenaria esaterako, duen efektu negatiboagatik. Gainera, hiri handietan, non tren linea asko dauden, katenariak itxura txarra ematen du. Arazo hauek konpontzeko, aukera itxaropentsu bat ibiligailu hauei indukzio bidezko energia transferentzia (IPT) sistema bat jartzean datza. Era honetan, katenaria ken daiteke, karga era inalambrikoan egiten delako, non zati igorlearen bobinak lur azpian kokatuan dauden.

IPT sistema ezberdinen artean, lan hau indukzio bidezko energia transferentzia dinamikoan (D-IPT) du arreta, hau da karga ibilgailua mugimenduan dagoenean egiten da. Zehazki, tesi hau 'meander' motako bobinen diseinura zuzendua dago. Horretarako, lehen zatian IPT sistemaren oinarrizko printzipioak azaltzen dira. Ekuazioak aurkezten dira eta poloen banaketaren limiteak kalkulatzen dira. Hauek 3.3kW-ko prototipo batean balioztatzen dira.

Aurrerago, 'meander' motako bobinaren funtzionamendua deskribatzen da. Sistema hau modelatzen duen ekuazioak aztertzen dira eta

akoplamendu konstatea lortzeko aukera nabarmentzen da. Gainera, aurkeztutako aldaketekin, sistema multifasikoa baliokidea den sistema monofasiko batekin aztertu daiteke. Honi esker, poloen banaketaren limitea erraz kalkulatu daiteke. Limite hau erabiltzen, IPT sistema diseñatzeko prozedimendua deskribatzen da eta 50Wko prototipo batean balioztatzen da. Prototipo honek bobina hauen potentziala erakusten du, edozein posiziorako potentzia konstatea transmititzea lortzen baita, %70ko efizientziarekin.

Diseñu prozedimendu honetan oinarrituz, optimizazio prozedura bat proposatzen da, DIPT sistemare tamaina, pisua eta kostua hobetzeko. Adierazle haue arteko konpromisoa nabarmentzen da. Azkenik, optimizazio prozedura hau 9kWko sistema batean aplikatzen da eta prototipo batean balioztatzen da, %90ko efizientzia lortuz, edozein posizio eta potentziarako, bobinen artean 100mmko bereizketa izanda.

Glossary

Abbreviations

AC	Alternating Current
CAD	Computer Aided Design
CSI	Current Source Inverter
CO_2	Carbon Dioxide
DAB	Dual Active Bridge
DC	Direct Current
DD	Double-D
DIPT	Dynamic Inductive Power Transfer
ESR	Equivalent Series Resistance
EV	Electric Vehicle
FEM	Finite Element Method
GaN	Gallium Nitrate
ICE	Internal Combustion Engine
ICC	Isolated Conductive Charger
ICNIRP	International Commission on Non-Ionizing Radiation Protection
IGBT	Insulated Gate Bipolar Transistor
IPT	Inductive Power Transfer
LED	Light Emitting Diode
LV	Low Voltage
MF	Medium Frequency
MMC	Modular Multilevel Converter
MOSFET	Metal Oxide Semiconductor Field Effect Transistor
MV	Medium Voltage
NPC	Neutral Point Clamped

PET	Power Electronic Transformer
PFC	Power Factor Corrector
PHEV	Plug-in Hybrid Electric Vehicle
RT	Railway transportation
SAB	Single Active Bridge
Si	Silicon
SiC	Silicon Carbide
SST	Solid State Transformer
UC	UltraCapacitors
VSI	Voltage Source Inverter
ZVS	Zero Voltage Switching

Greek Symbols

δ	[m]	Skin depth
η		Efficiency
γ		Round conductor penetration ratio
λ	[m]	Geometric period of meander coil
μ_0	[H/m]	Permeability of vacuum
μ_r		Relative permeability
ϕ	[rad]	Electric delay angle
φ	[rad]	Geometric delay angle
ω	[rad/s]	Pulsation frequency
ω_0	[rad/s]	Resonance pulsation frequency
χ		Inductance ratio
χ_lim		Inductance ratio limit
ρ	[W/m^3]	Electrical conductivity

Roman Symbols

€	[€]	Cost of the coil
A_c	[m^2]	Coil Area
A_w	[m^2]	Winding Area
$\vec{B}$	[T]	Magnetic field vector
B_max	[T]	Maximum magnetic field

B_{x}	[T]	Magnetic field in x direction
B_{z}	[T]	Magnetic field in z direction
C_1	[F]	Transmitter or primary side resonant capacitor
C_2	[F]	Receiver or secondary side resonant capacitor
C_{eq}	[F]	Equivalent capacitance
C_{oss}	[F]	Semiconductor output capacitance
D		Duty Cycle
d_{s}	[m]	Strand diameter
$\vec{E}$	[V]	Electromotive force vector
E_{ON}	[J]	Turn on energy
E_{OFF}	[J]	Turn off energy
E_{REC}	[J]	Recovery energy
f	[Hz]	Working frequency
f_{sw}	[Hz]	Switching frequency
f_0	[Hz]	Resonance frequency
$i_{1,\mathrm{DC}}$	[A]	Transmitter or primary side DC current
$i_{2,\mathrm{DC}}$	[A]	Receiver or secondary side DC current
$\hat{i}_1$	[A]	Transmitter or primary side AC peak current
$i_{1,0}$	[A]	Transmitter or primary side initial AC current
$\hat{i}_2$	[A]	Receiver or secondary side AC peak current
$i_{2,0}$	[A]	Receiver or secondary side initial AC current
i_{DS}	[A]	Drain to source current
J_{max}	[A/m^2]	Maximum current density
k		Coupling coefficient
k_{lim}		Coupling coefficient bifurcation limit
k_{w}	[A/m^2]	Wire filling factor
l	[m]	Flux path length
$L_{\sigma 1}$	[H]	Leakage inductance of the transmitter or primary winding
$L_{\sigma 2}$	[H]	Leakage inductance of the receiver or secondary winding
L_{M}	[H]	Magnetizing inductance of a transformer
L_1	[H]	Self inductance of the transmitter or primary winding
L_2	[H]	Self inductance of the receiver or secondary winding
L_{T}	[m]	Length of the transmitter
L_{R}	[m]	Length of the receiver
$L_{\mathrm{x,x}}$	[H]	Self inductance of phase x

$L_{\mathrm{x},\Delta}$	[H]	Self inductance of phase x in triangle connection
$L_{\mathrm{x,Y}}$	[H]	Self inductance of phase x in star connection
M	[H]	Mutual inductance
$\hat{M}$	[H]	Mutual inductance peak value
$M_{\mathrm{x,y}}$	[H]	Mutual inductance between phase x and phase y
N		Number of turns
$N_{\mathrm{Fe,S}}$		Number of ferrites in series
$N_{\mathrm{Fe,P}}$		Number of ferrites in parallel
n_{T}		Turns ratio
p_{f}		Porosity factor
P_{C}	[W]	Capacitor losses
P_{out}	[W]	Output power
$P_{\mathrm{out,lim}}$	[W]	Output power bifurcation limit
$P_{\mathrm{out,max}}$	[W]	Output maximum power
$P_{\mathrm{sw,ON}}$	[W]	Semiconductor turn on losses
$P_{\mathrm{sw,OFF}}$	[W]	Semiconductor turn off losses
P_{sw}	[W]	Switching losses
P_{s}	[W]	Magnetic core losses
P_{int}	[W]	Internal proximity effect losses
P_{ext}	[W]	External proximity effect losses
P_{MOSFET}	[W]	MOSFET conduction losses
P_{Diode}	[W]	Diode conduction losses
P_{skin}	[W]	Skin effect losses
P_{Al}	[W]	Losses in the aluminum
P_{Fc}	[W]	Losses in the ferrite cores
P_{T}	[W]	Losses in the transmitter
P_{R}	[W]	Losses in the receiver
Q_{G}	[C]	Gate charges
r_{b}	[m]	Bundle radius
r_{s}	[m]	Strand radius
R_{AC}	[Ω]	Equivalent AC resistance
R_1	[Ω]	Transmitter wire inherent resistance
R_2	[Ω]	Receiver wire inherent resistance
$R_{2,\mathrm{DC}}$	[Ω]	Secondary side DC resistance
R_{DC}	[Ω]	Wire DC resistance
R_{DS}	[Ω]	Drain to source resistance
$R_{\mathrm{Dth,jc}}$	[k/W]	Diode junction to case thermal resistance
$R_{\mathrm{Tth,jc}}$	[k/W]	Transistor junction to case thermal resistance
s_{z}	[m^2]	Size of the coil

t_{d}	[s]	Dead-time
T	[s]	Electric period
$\hat{v}_1$	[V]	Transmitter or primary side AC peak voltage
$\hat{v}_2$	[V]	Receiver or secondary side AC peak voltage
$V_{1,\mathrm{DC}}$	[V]	Transmitter or primary side DC voltage
$V_{2,\mathrm{DC}}$	[V]	Receiver or secondary side DC voltage
V_{CE}	[V]	Collector-emitter blocking voltage
V_{Coss}	[V]	Voltage of the output capacitance
V_{Ceq}	[V]	Voltage of the equivalent capacitance
$V_{\mathrm{Ceq,0}}$	[V]	Initial voltage of the equivalent capacitance
V_{DS}	[V]	Drain to source voltage
V_{F}	[V]	Diode forward voltage
W_{T}	[m]	Width of the transmitter
W_{R}	[m]	Width of the receiver
W_{w}	[m]	Winding width
w_{g}	[g]	Weight of the coils
z	[m]	Distance or separation between the coils
Z_{in}	[Ω]	Input impedance
Z_1	[Ω]	Transmitter or primary impedance
Z_2	[Ω]	Receiver or secondary impedance

List of Publications

Within this research project, several scientific contributions to the literature were published. These are listed below.

JOURNAL ARTICLES:

a. **U. Iruretagoyena**, A. Garcia-Bediaga, L. Mir, H. Camblong, I. Villar, *Design, Optimization and Experimental Validation of a 9kW/100kHz Three-Phase IPT*, submitted to IEEE Journal of Emerging and Selected Topics in Power Electronics, May 2018.

b. A. Avila, A. Garcia-Bediaga, **U. Iruretagoyena**, I. Villar, A. Rujas, *Comparative evaluation of front and back end PFC IPT systems for a contactless battery charger*, accepted for publication in IEEE Transactions on Industry Applications, 2018.

c. **U. Iruretagoyena**, I. Villar, A. Garcia-Bediaga, L. Mir, H. Camblong, *Design and Characterization of a Meander-Type Dynamic Inductively Coupled Power Transfer Coil*, in IEEE Transactions on Industry Applications, vol. 53, no. 4, pp. 3950-3959, Apr. 2017.
DOI: 10.1109/TIA.2017.2692199

d. R. Bosshard, **U. Iruretagoyena**, J.W. Kolar, *Comprehensive Evaluation of Rectangular and Double-D Coil Geometry for 50 kW/85 kHz IPT System*, in IEEE Journal of Emerging and Selected Topics in Power Electronics, vol. 4, no. 4, pp. 1406-1415, Dec. 2016.
DOI: 10.1109/JESTPE.2016.2600162

CONFERENCE ARTICLES:

e. I. Villar, A. Garcia-Bediaga, **U. Iruretagoyena**, R. Arregi, P. Estevez *Design and experimental validation of a 50kW IPT for Railway Traction Applications*, in: IEEE Energy Conversion Congress and Exposition (ECCE), Portland, 2018

f. F. Gonzalez–Hernando, **U. Iruretagoyena**, M. Arias, I. Villar, *Diseño de sistema de transferencia dinamica de energia por induccion con bobinas concentradas en aplicacion ferroviaria*, in: Seminario Anual de Automatica y Electronica Industrial e Instrumentacion (SAAEI), Valencia, Spain, 2017.

g. **U. Iruretagoyena**, A. Garcia-Bediaga, L. Mir, H. Camblong, I. Villar, *Bifurcation phenomenon limits for three phase IPT systems with constant coupling coefficient*, in: IEEE Energy Conversion Congress and Exposition (ECCE), Cincinnati, 2017, pp. 4851-4858.
DOI: 10.1109/ECCE.2017.8096824

h. A. Avila, A. Garcia-Bediaga, **U. Iruretagoyena**, I. Villar, A. Rujas, *Comparative evaluation of front and back end PFC IPT systems for a contactless battery charger*, in: IEEE Energy Conversion Congress and Exposition (ECCE), Cincinnati, 2017, pp. 118-125.
DOI: 10.1109/ECCE.2017.8095770

i. **U. Iruretagoyena**, A. Garcia-Bediaga, A. Rujas, H. Camblong, I. Villar, *Operation boundaries of single/three phase inductive power transfer systems with series-series compensation*, in: European Conference on Power Electronics and Applications (EPE), Warsaw, 2017, pp. 1-9.
DOI: 10.23919/EPE17ECCEEurope.2017.8099214

j. F. Gonzalez–Hernando, **U. Iruretagoyena**, M. Arias, I. Villar, *Dynamic IPT system with lumped coils for railway application*, in: European Conference on Power Electronics and Applications (EPE), Warsaw, 2017, pp. 1-9.
DOI: 10.23919/EPE17ECCEEurope.2017.8099345

k. **U. Iruretagoyena**, I. Villar, A. Garcia-Bediaga, L. Mir, H. Camblong, *Design and Characterization of a Meander-Type Dynamic*

Inductively Coupled Power Transfer Coil, in: IEEE Energy Conversion Congress and Exposition (ECCE), Milwaukee, 2016, pp. 1-8.
DOI: 10.1109/ECCE.2016.7855003

l. **U. Iruretagoyena**, I. Villar, A. Garcia-Bediaga, A. Rujas, H. Camblong, *Desarrollo de un Cargador Inalambrico para Vehiculo Electrico basado en SiC*, in: Seminario Anual de Automatica y Electronica Industrial e Instrumentacion (SAAEI), Elche, Spain, 2016.

m. I. Villar, **U. Iruretagoyena**, A. Rujas, A. Garcia-Bediaga, I. Perez–de–Arenaza, *Design and implementation of a SiC based contactless battery charger for electric vehicles*, in: IEEE Energy Conversion Congress and Exposition (ECCE), Montreal, 2015, pp. 1294-1300.
DOI: 10.1109/ECCE.2015.7309841

Contents

Chapter 1

Introduction

Future sustainable transportation largely depends on how power electronics will manage to achieve smaller, lighter and more efficient power converter and systems.

Over the XXI. century, the public awareness on the environmental impact of the green house emissions has greatly increased. Even though there have been efforts to turn around the situation, still there is much work to do.

Despite the increasing number of Electric Vehicles (EV), the absolute number of EV is yet far from the petrol based (ICE) vehicles, representing less than 1% of the market share [Global EV outlook, 2016]. In the two biggest world economies, the EV represents 0.7% of the total cars sold in 2015 in the United States and 1% in China. In other technology spearhead countries, such as Japan and South Korea, the market share is even lower, being 0.6% and 0.2% respectively. Only four countries beat the 1% barrier in the world, Denmark 2.2%, Sweden 2.4%, the Netherlands 9.7 % and standing out among all Norway with 23.3% (see Figure 1.1).

The reason behind this difference between north European countries and the rest is not technological, it is mainly economical. The reason comes from the high initial purchase cost of electric vehicles. Even though at long term EV are amortized, since fuel costs are reduced to the minimum, the initial cost is considerably higher. In [The Boston Consulting Group, 2009] is detailed that the price is almost the double

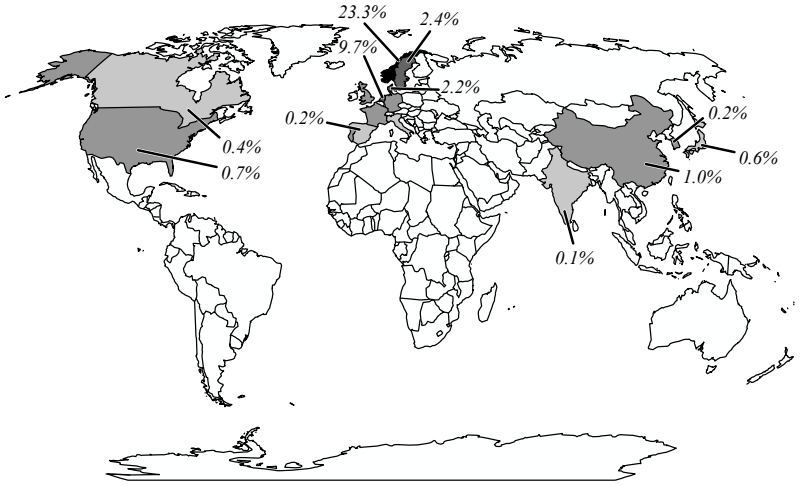

Figure 1.1: World map, representing the market share of electric cars in 2015. Norway 23.3%, Netherlands 9.7% and Sweden 2.4% are the top 3 countries in the world, data taken from [Global EV outlook, 2016].

for the EV compared to an ICE [1]. In countries like Norway, governments have adopted fiscal policies that benefit environmental friendly technologies, reducing taxes, giving fundings with beneficial conditions and penalizing big pollutants [Global EV outlook, 2016].

In order to push further the irruption of EV in the rest of the countries, three issues must be addressed:

- **Ownership cost reduction**

  Either by reducing the production costs, mainly attributed to batteries which are 30% of the total ownership cost [Nykvist and Nilsson, 2015], or by more aggressive policy support schemes, e.g tax benefits.

[1] Estimated value for a five year total ownership cost (TCO), with an oil barrel of 50 USD.

- **Range extension**

  Increasing the efficiency or reducing the weight of the power train on board will lead to a higher mileage. Nowadays, still EV mileage is half of combustion's, being a considerable dissuading factor.

- **Charging convenience improvement**

  Reducing the time and simplifying the charging process is necessary, as users seek comfortable, easy to use systems [IRENA, 2017].

It can be noticed that the main drawbacks in EV are mainly related to the storage system, i.e. the batteries. Their energy storage capacity is low (compared to petrol), they need a long period to be fully charged and they are expensive. Therefore, recent research is focused in this particular element. Either by improving the battery itself (better chemistry [The Boston Consulting Group, 2010]) or by reducing its use (other supply sources, e.g hybridization).

Among many others, one of the most promising concepts under study is the Inductive Power Transfer (IPT) [Bolger et al., 1978, Eghtesadi, 1990, Elliott et al., 1995, Esser, 1995]. New power semiconductor technologies (SiC [Onar et al., 2013a, Villar et al., 2015] and GaN [Cai and Siek, 2017]) have enabled the merge of reasonably high switching frequencies (kHz order) in high power converters (kW order) [Vandevoorde and Puers, 2001]. It permitted long time known technologies, such as IPT (Tesla's patent is from 1914 [Tesla, 1914]), become reality [Covic and Boys, 2013].

IPT can be the solution to the aforementioned issues. The ownership cost of EV will be greatly decreased, since part of the batteries could be replaced for a receiver coil, much cheaper. The car will not need to carry with all the necessary energy, after all, it could be charged at any stop, e.g traffic lights, parkings... This term is known in the literature as *opportunity charging* [Bosshard, 2015]. Therefore, the range anxiety will also be partially solved. As long as there are charging points the range can be considered infinite. Finally, also the charging process will be improved. The user will not need to plug-in the vehicle. Placing the car above the transmitter coil will start the charging procedure.

Even though IPT systems are commercially in an early stage, (see Section 1.2.2) academia is already working on the next idea; transmitting the power inductively while the vehicle is moving. This concept

is known as Dynamic IPT (D-IPT) [Lukic and Pantic, 2013, Lee et al., 2014, Turki et al., 2015]. The essential idea is to create a track that will supply power continuously, analogous to the catenaries, but wireless. This way, the batteries could be fully or partially removed from the vehicle, reducing weight and increasing the efficiency.

1.1 The Global Picture: From Conductive to Inductive Power Transmission

Since the main objective of IPT systems is to compete with Isolated Conductive Chargers (ICC), in the following section a brief review of the current state of this technology is going to be carried out.

1.1.1 Conductive charger conversion structure

According to SAE J1772, depenging on the charging power, conductive chargers for EV or plug-in electric vehicle PHEV vehicles can be classified into three different groups [Yilmaz and Krein, 2013], see Table 1.1.

Power Level Types	**Level 1** (Opportunity)	**Level 2** (Primary)	**Level 3** (Fast)
Voltage	120 VAC (US) 230 VAC (EU)	240 VAC (US) 400 VAC (EU)	208-600 VAC or VDC
Power Level	1.4kW (12A) 4-11 hours (PHEV)	4kW (17A) 1-4 hours (PHEV)	50kW 0.4-1 hour (EV)
	1.9kW (20A) 11-36 hours (EV)	8kW (32A) 2-6 hours (EV)	100kW 0.2-0.5 hour (EV)
		19.2kW (80A) 2-3 hours (EV)	

Table 1.1: Isolated Conductive Charging levels according to SAE J1772.

Level 1 chargers (opportunity charging)

Level 1 chargers are also known as slow charger or opportunity chargers. Level 1 chargers are directly connected to standard house outlets,

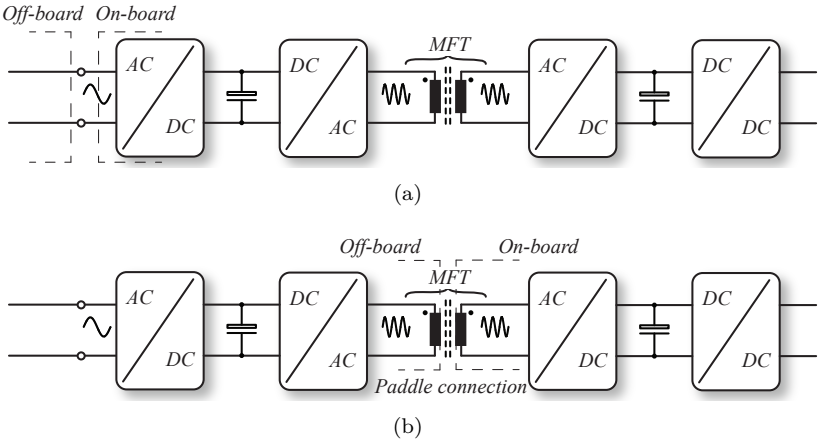

Figure 1.2: Energy supply circuit of an Isolated Conductive Charger (ICC) with a Medium Frequency Transformer (MFT) and output voltage regulation. (a) direct connection to socket. (b) connection with a paddle.

120V/15A for US and 230/16A in EU [Dubey and Santoso, 2015]. For that reason the power that can be delivered with this chargers is less than 3.5kW.

Level 1 chargers are intended to be used during overnight charging or when there is an emergency. For that reason, Level 1 conductive chargers are usually placed inside the vehicle, see Figure 1.2(a). Alternatively they can be connected with a 'paddle' for easy connection, see Figure 1.2(b), [Yilmaz and Krein, 2013, Khaligh and Dusmez, 2012].

Being the space and weight critical factors, EV chargers are required to have high power densities. In any power electronic conversion system, the biggest and heaviest components are the cooling and the passive elements. So, in order to increase the power density, the operation frequency is increased [Huber, 2016]. The 50/60Hz input voltage is converted into a kHz order voltage with a DC/AC converter (typically a full-bridge converter), which is connected to the primary winding of a medium frequency transformer MFT. At the secondary side an AC/DC rectifier is connected (typically a full-bridge or a diode bridge). This conversion structure is also known as Power Electronic Transformer PET and is already used in high power systems, such as wind conversion or railway traction power sources [Villar, 2010, Garcia Bediaga, 2014].

The main drawback of Level 1 chargers is that fully charging a battery can take up to 4-11 hours in a hybrid vehicle or 11-36 hours in a fully electric vehicle.

Level 2 chargers (primary charging)

Level 2 is the primary charging method for private and public facilities [Yilmaz and Krein, 2013]. Existing Level 2 equipments can charge from 240V US or 400V EU up to 80A, 19.2kW [Dubey and Santoso, 2015]. These charger require a dedicated equipment and special connection points for home or public points. Level 2 chargers are almost fully located outside the vehicle, see Figure 1.3. Even though compared with a Level 1 charger the size and weight are not that restrictive, a medium-frequency transformer is also used in Level 2 chargers, so the conversion structure is basically the same as Level 1.

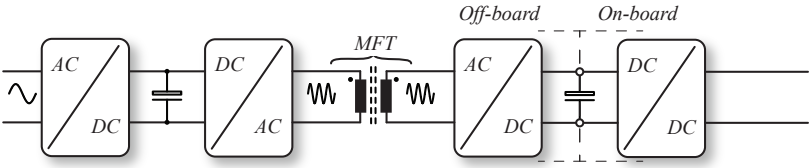

Figure 1.3: Level 2 off-board charger.

There are exceptions such as the Tesla EVs that incorporate the Level 2 chargers already in the vehicles [Yilmaz and Krein, 2013]. However, they require a power connection of 400V in EU, which is not typically available in the houses. Therefore, extra installation is required at private garages.

With Level 2 chargers, the charging time for a Plug-in Hybrid Electric Vehicle PHEV is between 1-4 hours, whereas for an EV between 2-6 hours.

Level 3 chargers (fast charging)

Finally Level 3 chargers have the highest power capacity installed. They are also known as fast chargers. These chargers are connected to the three phase mains, 600V in EU, and are intended to be installed in highways rest areas and refueling points, similar to gas stations.

Due to the higher power, the power conversion structure is simplified. A low frequency (50/60Hz) transformer is used to step-down the voltage [Dusmez et al., 2011]. Afterwards with a controlled AC/DC rectifier a DC voltage is created. Due to the higher voltages, typically multilevel converters are used, such as the Neutral Point Clamped NPC or the cascaded H-bridge [Khaligh and Dusmez, 2012].

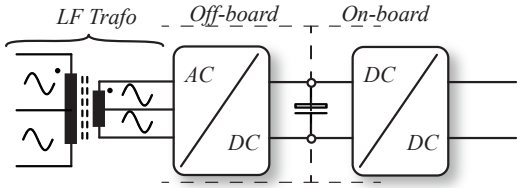

Figure 1.4: Level 3 EV charging. Low frequency transformers and multilevel topologies are typically used.

With a Level 3 charger of 100 kW, an EV can be charged in approximately 10 to 30 minutes [Yilmaz and Krein, 2013].

1.1.2 Inductive charger conversion structure

The energy conversion structure of an IPT is basically the same compared to a Level 1 charger, see Figure 1.2. In this case, instead of having a magnetic core in the medium frequency transformer, the windings are separated by the air.

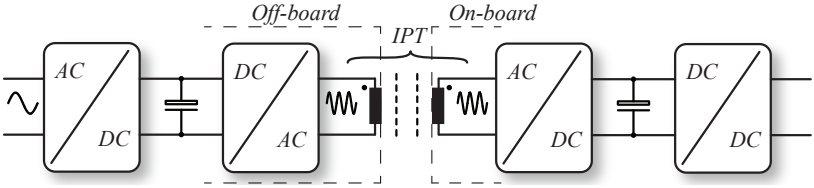

Figure 1.5: Energy supply circuit: Inductive Power Transfer (IPT) solution with loosely coupled transformer. Comparing to an ICC the air-gap is increased.

Even thought the power electronics are the same, the fact of having a large air-gap changes drastically the behavior of the system. In IPT systems the leakage inductance is much higher than in conductive chargers. This large inductance produces an output power reduction

and lowers the efficiency. Thus, resonance configurations are necessary. These resonance arrangements are achieved using compensation techniques which will be discussed in section 2.4 and section 3.3.

In the following sections a review of the current state of the art of static and dynamic IPT systems is carried out. Two different trends are going to be analyzed: academy research and industrial solutions.

1.1.3 Main challenges

Although ICC and IPT conversion structures offer interesting advantages over conventional solutions, currently their high power application faces four main challenges [Villar, 2010, Garcia Bediaga, 2014]:

1. Higher efficiency requirements.
2. Wider technical and commercial deployment of key components (semiconductors, wires...).
3. Higher reliability levels.
4. Higher power densities, to reduce boarded equipment.

In addition, IPT systems have to deal with the problem of the magnetic and electric fields. This fact has propitiated a number of standards and norms specifying the reference levels regarding the exposure of humans to this electromagnetic fields. For instance the guidelines published by the International Commission on Non-Ionizing Radiation Protection (ICNIRP) [Lin et al., 2010].

1.2 State of the Art

In order to deal with the aforementioned challenges, recently, great research has been carried out in IPT and D-IPT systems, from both academy and industry. Many universities and companies, sometimes even working together, have proposed a wide variety of solutions.

1.2.1 Academy Research

For static IPT systems, from the design point of view, academy is searching for ways of reducing the size of the coils and magnetic emissions, and increasing the efficiency of the receiver equipment, either by

improving the magnetic design with enhanced coil structures, such as *Double-D* (DD) coils [Budhia et al., 2011b, Budhia et al., 2013, Ongayo and Hanif, 2015], or alternatively, searching for the highest converter power density [Bosshard et al., 2015] (see Table 1.2).

In [Bosshard et al., 2016] it is shown that by using DD coils the emitted magnetic field is almost 50% smaller compared with a square coil of the same size and same power. As a consequence the efficiency is reduced about 2%. In addition, [Bosshard, 2015] demonstrates that a power density of 2.7 kW/dm^3 with a specific power of 2.0kW/kg can be achieved using newly developed 1200V, 90A SiC MOSFETs. It has to be remarked that the specific power of a high energy Li-Ion battery is of approximately 0.3kW/kg [Panasonic, 2010]. This IPT prototype of 50kW is working at 85kHz with an overall efficiency of 95.8%. Among academia, it can be considered as the most compact static charging solution.

This trend of making the system as small as possible is clearly described in [Covic and Boys, 2013], where it is stated that the current static IPT solutions require 10-100 times smaller clearances and tolerances for similar efficiency comparing with 15 years ago IPT systems. Also the evolution of the power electronics have pushed the frequency from ∼10-20kHz to 85kHz and beyond. Consequently, the power ratings have increased from 3kW to the actual 50kW solutions and the pace is still going forward.

The trend regarding dynamic IPT charging has taken two clearly defined paths [Lukic and Pantic, 2013, Turki et al., 2015]. On the one hand, there are the segmented or distributed D-IPT systems [Choi et al., 2013, Sampath et al., 2016, Liu et al., 2016], depicted in Figure 1.6(a). Here, the systems are built concatenating stationary charging topologies, creating a charging lane. This way, each of the coils will be turned on when the receiver coil, i.e. the vehicle, is placed on top of it. On the other hand, single coil solutions extend the size of the transmitter coil so that the receiver coil will always be within the magnetic field [Huh et al., 2010, Huh et al., 2011] (see Figure 1.6(b)). In this case, the transmitter coil will always be delivering power independently of where the receiver coil is placed, of course, only if the receiver is inside the magnetic field.

Depending on the chosen solution, in addition to the efficiency and power density targets, different challenges have to be faced. With a segmented solution, the sizes of the transmitter coils are smaller. This

Table 1.2: Academy examples [Dai and Ludois, 2015].

Institute	P(kW)	η(%)	f(kHz)	z(mm)	A(dm^2)
Saitama Univ., Japan, 2010 [a]	1.5	95	20	70	6
ORNL, USA, 2013[b]	2	91	23.5	75	11.34
Univ. of Auckland, New Zealand, 2011[c]	2	85	50	200	38.49
IK4-IKERLAN, Spain, 2015[d]	3.3	∼90	100	80	28.27
Utah State Univ., USA, 2012[e]	5	90	20	246	21.63
ORNL, USA, 2011[f]	6∼7	95	48∼81	125∼254	∼36
Univ. of Auckland, New Zealand, 2017[g]	10	-	40	250∼400	23.01
KAIST, Korea, 2010	3∼25	71∼87	20	10∼250	9.9∼13.39
Univ. of Auckland, New Zealand, 2005[h]	30	-	20	45	48
ETH Zürich, Switzerland, 2016[i]	50	95.8	85	200	24

[a] [Nagatsuka et al., 2010, Chigira et al., 2011]
[b] [Ning et al., 2013, Onar et al., 2013b]
[c] [Budhia et al., 2011a, Budhia et al., 2011b, Wu et al., 2011]
[d] [Villar et al., 2015]
[e] [Wu et al., 2012]
[f] [Chinthavali et al., 2013]
[g] [Nagendra et al., 2017]
[h] [Wang et al., 2004, Wang et al., 2005]
[i] [Bosshard and Kolar, 2016a, Bosshard and Kolar, 2016b]

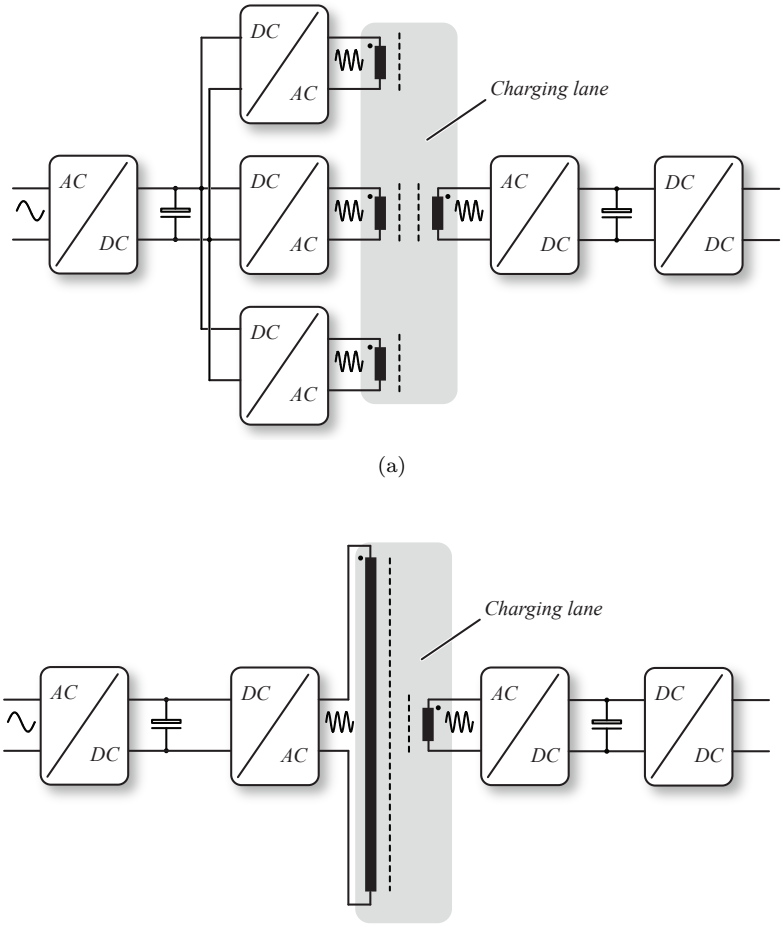

Figure 1.6: Coil distribution architectures for D-IPT energy supply systems: (a) Segmented coil distribution, each of the coils is supplied by an independent inverter. (b) Single coil solutions, all the supply track is covered by a single coil supplied by a single inverter.

entails that the inductance value will be smaller, and as a consequence, the voltage that must withstand too. However it does not come for free. The movement of the vehicle makes the control very complex,

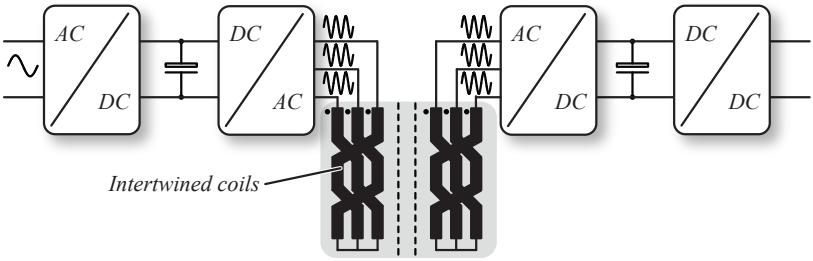

Figure 1.7: Three phase D-IPT systems with intertwined coils. Each of the transmitter coils covers all the charging lane length. The magnetic fields of the coils are combined to transmit the power to the receiver wingdings.

since the equivalent circuit keeps changing all the time. The control must be very accurate to manage those changes and the circuit must be designed to operate at the worst case. With this configuration, at the present time, the power densities and efficiencies are identical to the static systems, around 90%, and most of the publications are focused on implementing different control strategies [Swain et al., 2014, Huang et al., 2015, Gati et al., 2017] . Besides, with a single coil solution, the control becomes simpler, but the large size of the transmitter coils complicates the voltage insulation and, in addition, losses are increased, being the efficiency at the current state around 70%, with an air-gap of 10cm [Huh et al., 2010, Huh et al., 2011, Choi et al., 2015].

In order to improve single coil deficiencies, the solution presented in the literature is using multi-phase intertwined transmitter coils [Winter et al., 2013, Turki et al., 2015] (see Figure 1.7). Combining their magnetic fields, the output power can be controlled to deliver constant power to the receiver [Sato et al., 1996, Sato et al., 1998, Sato et al., 1999, Gao, 2007]. This way, the large voltages through the inductors are reduced, since each coil will carry only part of the total power. Even though there are works related to this kind of topologies [Meins and Struve, 2013, Meins and Vollenwyder, 2013, Vollenwyder et al., 2014], no design process nor experimental efficiency data is available in the literature concerning high power (over >1kW) applications. Thus, further research is necessary to exploit its full potential.

1.2.2 Industry Solutions

In industry, the objectives are not only the same as for the academy, high power density and efficiency, but primarily the overal cost reduction is targeted. Among high power (>50kW) IPT products, the most representative are resumed in Table 1.3.

At the present time, commercial IPT charger are thriving but still not many products can be found in the market. The solutions of Table 1.3 are some of the developed current solutions from various companies and research institutes.

It can be appreciated in Table 1.3 that all the solutions are based on settled technologies. The converter type is always a full-bridge and the newly developed SiC devices are not used, since the switching frequency is still low. This is clearly due to the high costs of SiC MOSFETs compared to Si IGBTs.

However, with the upcoming production growth of SiC devices, these costs will go down and we will start having higher frequencies in IPT systems. This will offer smaller, lighter and cheaper solutions.

1.3 IPT in railway transportation

Even though the objective of IPT is to be the main charging option for EV in the future, nowadays public transportation seems to be the niche were IPT and specially D-IPT can be installed. Among all, railway transportation appears the most realistic due to a simple fact, the rails set the position of the vehicle. This matter simplifies drastically the designing process, since the misalignment of one of the axis can be neglected. Moreover, not only the transmission coil can be optimized. As trains typically run the same route, the whole charging equipment can be designed optimally, setting the best charging points [Herrera et al., 2016].

The main advantage of IPT systems in railway transportation is the opportunity of removing the pantograph. This element is one of the components whose maintenance is the most expensive [Mir et al., 2009]. The pantograph suffers from friction and adverse climatology conditions. Moreover, the catenary itself could also be removed. Another element that is exposed to friction, climatology and vandalism.

Other ways of removing this element have already put into practice. For instance, a solution is to endow the train with a storage system,

Table 1.3: Practical examples

	Conductix-Wampfler [a]	Bombardier [b]	Kaist-OLEV [c]		WAVE [d]
Type	Static	Static Dynamic	Static Dynamic		Static
Aplication	Bus Tram	Bus	Bus	Tram Train	Bus
Power	60/120/180kW	200kW	100kW	180kW	50kW
Frequency	20kHz	20kHz	20kHz	60kHz	23.4kHz
Max. Distance	5cm Approach system.	6.5cm Approach system.	20cm	10cm	17.8cm
Efficiency	90%	92%	85%	74%	90%
Misalignment	- - -	- - -	30cm	- - -	15cm
Comp. Topology Primary/Secondary	Series/Series	Series/Series	Series/Series	Series/Series	LCL-T/Parallel
Coil Type	Circular	Meander	Monorail		Circular
Converter Type	- - -	Full-bridge	Full-bridge		Full-bridge

[a] [Conductix Wampfler, 2012]
[b] [Bombardier, 2010, Desire et al., 2015]
[c] [Choi et al., 2015]
[d] [Wu and Masquelier, 2015]

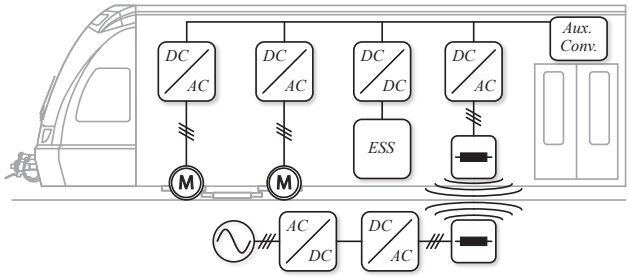

Figure 1.8: Train's internal power converters supplied by an IPT system. Energy storage system (ESS) is added to recover energy during breaks.

batteries and ultracapacitors (UC), that could be recharged in the stops [Mir et al., 2009, Herrera et al., 2015, Herrera et al., 2016]. However, these solutions do not solve the problem of the high costs of the batteries and the infrastructure maintenance costs.

Regarding D-IPT, at first sight, the full removal of the storage system seems the ideal solution. Nevertheless, the cost of installing an inductive power transmission system through all the way, seems unfeasible. It could never compete with catenaries nor batteries in price. Even having less maintenance costs, long railway systems can have over 300km. Dynamic charging solutions could be useful during accelerations or in the places where there are high peak consumptions, e.g ramps.

This way, the storage system could be optimized in energy and not in power. Indeed, the main power peaks would be delivered by the D-IPT charger. Furthermore, the benefit of the energy recovery feature of the batteries will be kept.

1.4 Motivation and Objectives

The design of an IPT system is an engineering problem with multiple, some times counterpart, objectives, such as: efficiency, size, weight and cost. Therefore, the understanding of the interdependencies among them is essential. Thus, the main objective of this work is to clarify this dependencies and develop a design and optimization process that is capable of giving the optimal solution. Particularly, the objective is going to be focused on the design of a three-phase inductive power transfer system.

For that purpose, all the equations set for modeling the three-phase system have to be developed. In this work a special configuration of intertwined coils is going to be used, the meander type coil. This arrangement offers unique features such as constant coupling, which is specially convenient for inductive charging, as the control can be greatly simplified.

In addition, for proper comparison between solutions, another objective is to model the high frequency effects in the conductors, such as skin effects and proximity effects, and afterwards use them for the proper wire selection.

Apart from that, the compensation topologies used in the single phase IPT systems are translated to the three-phase system. Taking into account the coupling among transmitters, another objective of this work is to properly calculate the resonance capacitor values. Due to this compensations, the 'pole-splitting' appears. This is widely discussed in the literature for the single phase system, but there is no analysis for three-phase IPT systems. Thus, a thorough analysis has to be carried out in this regard.

In order to validate the theory and the optimization process, two prototypes are going to be built, the first one of 50W and the second one of 9kW.

1.5 Outline of the Thesis

Within this introductory chapter, the state of the art of inductive power transfer has been summarized, emphasizing the differences between academia and industry. The most remarkable solutions have been listed and described. Once the background of the work has been described, the motivation and the objectives of this thesis have been presented.

In Chapter 2, in order to make the transition from conductive to inductive charging smoother, first, the working principles of classical grid connected transformers are introduced. Afterwards, the Isolated Conductive Charger (ICC) is explained. Being the Inductive Power Transfer a ICC without core, the power capability differences are outlined. In order to improve such capability, compensation topologies are presented. However, pole-splitting may occur. This effect is caused due to the interaction between resonant tank. So, in the following, the pole-splitting limits are calculated for a single phase system. Finally, the theory is validated with a 3.2kW prototype.

In Chapter 3, first, the meander type coil is introduced. With its unique shape, it is demonstrated that a sinusoidal mutual inductance can be achieved. Adding more phases, combining the sinusoidal magnetic fields, a constant induced voltage can be achieved. It is demonstrated that three phases are required to achieve a constant power transmission. For that reason the set of equations that model an IPT system with three transmitters and three receivers is developed. It is demonstrated that with a few modifications a single phase equivalence can be obtained. Once the model is known, the compensation topologies are revisited and adapted for the three-phase system. Here also, the pole-splitting limits are calculated. Afterwards, a design procedure is detailed. To conclude this chapter, a 50W demonstrator is built.

In Chapter 4, first, the different optimization techniques are analyzed. Being the Pareto-Front the most suitable, an optimization flowchart is presented. Afterwards, this optimization is applied to a 9kW 100kHz system. The Pareto-Front comparing efficiency, weight, coil voltage and cost are shown. Here, the effect of different parameters such as number of ferrites and coil dimensions are discussed. Afterwards, from the previous optimization, a solution is chosen. This solution is thoroughly analyzed, and finally, it is experimentally validated in the laboratory.

Finally, in Chapter 5, the main conclusions of this thesis are underlined, the contributions are discussed and future works are pointed out.

Chapter 2

Inductive Power Transfer Basics

In order to make the transition smoother from more conventional power transmission systems to IPT systems, this chapter first analyzes the working principles of classical grid connected transformer in Section 2.1. Afterwards, the single-phase Isolated Conductive Charger (ICC) will be discussed in Section 2.2. Basically the concept of ICC is a classical transformer that is working at medium frequencies (kHz), supplied by an inverter. As it will be shown, the size and the weight are reduced, therefore material is economized. In addition, introducing power electronics enables ICC to control the power flow between the primary and secondary sides. In Section 2.3, the transition to IPT will be detailed. Having air between the primary and the secondary windings instead of a ferromagnetic core, reduces the coupling and dramatically changes the behavior of the system. Besides, more appropriate equivalent circuits will be reviewed, that better represent the interaction between the coils. In Section 2.4, compensation topologies will be analyzed. It will be shown that with resonant configurations, the power transmission is greatly improved, mainly in efficiency and power capability. Finally, in Section 2.5 the different parts that make the system less efficient, such as the wires, the cores and the semiconductors, are going to be analyzed.

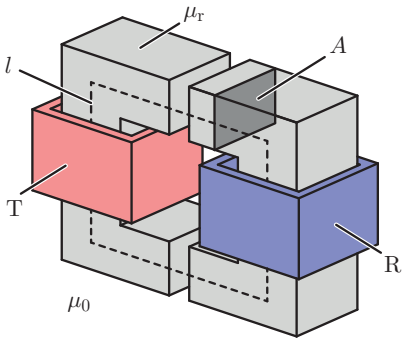

Figure 2.1: Representation of a transformer with a transmitter or primary coil T and a receiver or secondary coil R. l, stands for the field path through the core. A represents the area, where this field circulates.

2.1 Classical transformer

In almost any power transmission system electric isolation is required between the source and the load. The classical way of obtaining this isolation is by placing a transformer in the conversion chain [Garcia Bediaga, 2014].

The very basic working principle of transformers can be explained by two laws, *Ampère's* (2.1) and *Faraday's* (2.2). The first one states that due to a circulating electric current $\vec{i}$, a proportional magnetic field $\vec{B}$ is created

$$\oint_A \vec{B} \mathrm{d}\vec{A} = \mu_r \mu_0 \vec{i}, \tag{2.1}$$

where μ_0 is the permeability of the vacuum, μ_r is the relative permeability of the material and A is the enclosed area, see Figure 2.1. The second one describes that due to a enclosed varying magnetic field, a electromotive force $\vec{E}$ is induced in the circuit,

$$\oint_l \vec{E} \mathrm{d}\vec{l} = -\oint_A \frac{\mathrm{d}\vec{B}}{\mathrm{d}t} \mathrm{d}\vec{A}. \tag{2.2}$$

Thus, basically electric energy can be transformed into magnetic energy and then back again. Finally, the induced voltage $\vec{V}$ is proportional to $\vec{E}$ and multiple of the number of turns N. So, both equations can be combined to get

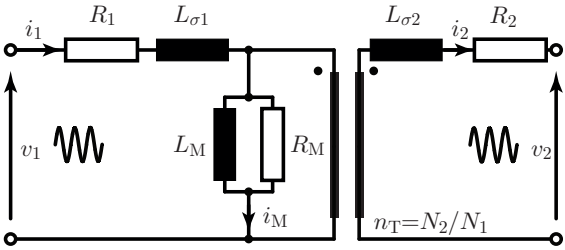

Figure 2.2: Transformer T-equivalent circuit. The resistances R_1 and R_2 represent the losses in the wiring. Whereas, R_M represents the losses in the core.

$$\vec{V} = N\frac{\mu_r\mu_0 A}{l}\frac{\mathrm{d}\vec{i}}{\mathrm{d}t}. \tag{2.3}$$

The middle term that relates how much voltage is generated due to the variation of the current is known as inductance,

$$L = N\frac{\mu_r\mu_0 A}{l}. \tag{2.4}$$

Thus, the conclusion from (2.4) is that the transformer consists of a circuit comprised of various inductances, that represent different voltage generations due to the varying current.

2.1.1 T-equivalent circuit

Depending on where is this counterpart voltage generated, the inductances get a different naming. The inductance generated through the core path that actually reaches the secondary coil, is known as magnetizing inductance L_M. Whereas the inductance generated by other paths, typically air, that is not linked, is known as stray inductance L_σ. Different equivalent circuits that represent transformers can be found in the literature. The most common one in transformers is the T-equivalent circuit [Van Schuylenbergh and Puers, 2009] represented in Figure 2.2. Neglecting the losses, the equivalent differential equation

is given by

$$\begin{aligned} \vec{v_1} &= L_{\sigma 1}\frac{\mathrm{d}\vec{i_1}}{\mathrm{d}t} + L_{\mathrm{M}}\frac{\mathrm{d}\vec{i_{\mathrm{M}}}}{\mathrm{d}t} \\ \vec{v_2} &= n_{\mathrm{T}} L_{\mathrm{M}}\frac{\mathrm{d}\vec{i_{\mathrm{M}}}}{\mathrm{d}t} + L_{\sigma 2}\frac{\mathrm{d}\vec{i_2}}{\mathrm{d}t}, \end{aligned} \tag{2.5}$$

were n_{T} stands for the turns ratio.

The target during the design of a transformer is to have the lowest possible stray inductance and the highest magnetizing inductance. For that reason, materials with very high relative permeability $\mu_{\mathrm{r}} \gg 1000$ are used. In classical transformers, 50∼60 Hz, Silicon-steel is used with a relative permeability of 4000, [Villar, 2010].

Here, the main characteristic of ideal low frequency transformers can be identified:

- **Fixed voltage ratio**. Being, $L_{\mathrm{M}} \gg L_{\sigma}$ makes possible to further simplify (2.5) into

$$\vec{v_2} = \frac{N_2}{N_1}\vec{v_1}. \tag{2.6}$$

  In a real system, it will depend on the stray inductances value, the inherent resistances of the windings and the power that is being transmitted.

- **Fixed current ratio** given by

$$\vec{i_2} = \frac{N_1}{N_2}\vec{i_1}. \tag{2.7}$$

  It will depend on the current flowing towards L_{M} and R_{M}. In almost any design, it can be considered constant.

- **Equal operating frequency** at both sides.

$$f_1 = f_2 \tag{2.8}$$

The main advantages of low frequency transformers are the low cost due to the simplicity, high reliability and robustness. In addition, the lifetime is also large and the achieved efficiency is higher than 98% [Ortiz, 2014].

However, there are also some drawbacks. Among them, susceptibility to DC currents that can saturate the core and losses in no load

situations, due to the permanent magnetizing current, are the most remarkable. In addition, depending on the application the size can be a problem. In low frequency transformers the core makes the transformer very big and heavy.

2.1.2 Transformer size

In any application with on-board equipment, the available space is usually very limited, and carrying large weights is counterproductive. The required core area A_c, equation (2.9), depends on the input voltage, the frequency f, the number of turns N_1, and the maximum magnetic flux B_{max} in the core [Ortiz, 2014].

$$A_c = \frac{1}{\sqrt{2}\pi} \frac{\hat{v}_1}{N_1 \ f \ B_{max}} \tag{2.9}$$

In addition, the winding area A_w should also be taken into account. This value depends on the circulating current density J_{rms}, the number of turns, the filling factor k_w and the maximum rms current density $J_{rms,max}$.

$$A_w = \frac{2\hat{i}_1}{k_w J_{rms,max}} N_1 \tag{2.10}$$

This leads to a total transformer area of

$$A_c \ A_w = \frac{\sqrt{2}}{\pi} \frac{P}{k_w J_{rms,max} f B_{max}}. \tag{2.11}$$

From (2.11) it can be deduced that the size of the transformer can be reduced increasing the frequency. Thus, in order to vary the frequency of a certain load, a power electronic converter is connected, interfacing the source and the transformer. Thanks to it, extra functionalities are obtained. The reactive power can be decoupled from the grind, the power flow can be controlled and over-current and over-voltage protections can be implemented. The combination of these power electronic converter and transformer is known as power electronic transformer (PET) or solid state transformer (SST) [Huber, 2016]. This same principle is used in Isolated Conductive Chargers (ICC).

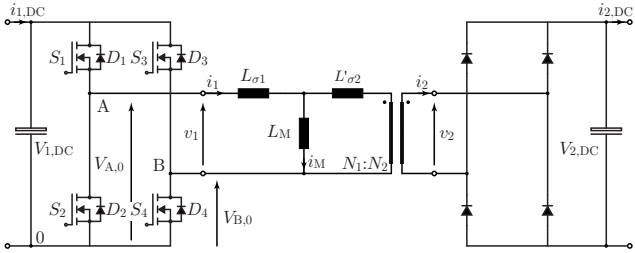

Figure 2.3: Single-phase Isolated Conductive Charging equivalent circuit with a Single-Active-Bridge converter topology.

2.2 Isolated Conductive Charger

Many works can be found in the literature regarding the design and optimization of isolated medium frequency converters [Villar, 2010, Garcia Bediaga, 2014, Ortiz, 2014, Huber, 2016]. In this work only the operation principles will be analyzed in order to move ahead towards IPT systems.

In literature, many converter configuration alternatives can be found for the medium voltage (MV) and low voltage (LV) sides, such as, Modular Multilevel Converters (MMC) [Huber, 2016], Neutral Point Clamped (NPC) [Ortiz, 2014] or Dual Active Bridge (DAB) [Villar, 2010, Garcia Bediaga, 2014]. During this thesis, the single active bridge **SAB** is going to be analyzed as in [Garcia Bediaga, 2014]. This converter offers a very good and robust solution when unidirectional power flow is required.

2.2.1 Single Active Bridge converter

Figure 2.3, shows the SAB topology. The primary coil is supplied by a Full-Bridge, being this topology the most common solution in industry, see Table 1.3. On the other side, the receiver is rectified by a diode bridge. The following nomenclature is going to be used throughout this work: $V_{1,DC}$-$V_{2,DC}$ and $i_{1,DC}$-$i_{2,DC}$ are the DC voltages and DC currents for the input and output respectively, whereas v_1-v_2 and i_1-i_2 are the AC voltages and AC currents for n the primary and secondary coils respectively.

The functioning of this converter is rather simple. Each of the semiconductor is complementary to its counterpart, i.e when the upper (S_1

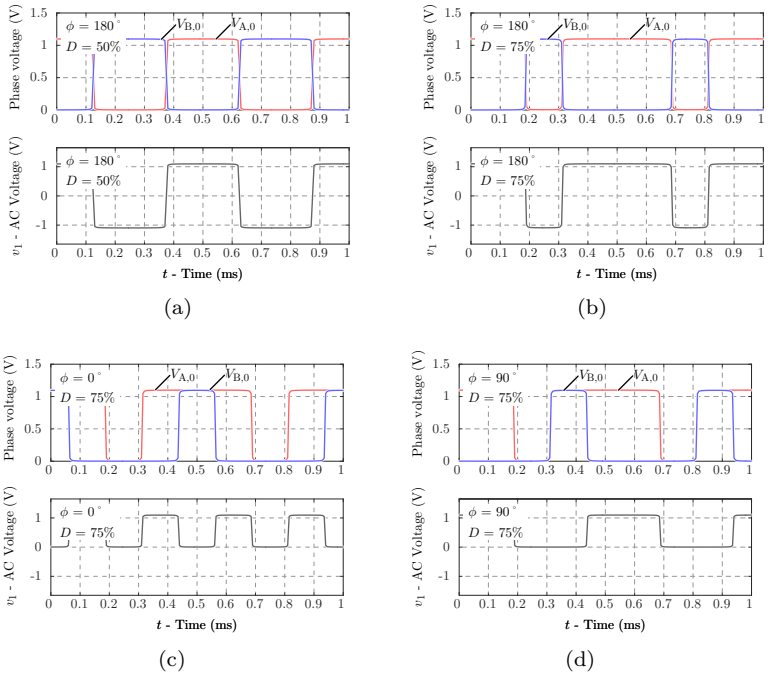

Figure 2.4: Different output voltages can be obtained by varying ϕ and D, described by equation (2.12). With an angle of 180°, the output voltage varies from -$V_{1,\mathrm{DC}}$ to $V_{1,\mathrm{DC}}$ and an equal duty cycle, in (a) $D = 50\%$ and in (b) $D = 75\%$. Besides, if the angle between the voltages is changed different voltage levels can be obtained. For example in (c), with $\phi = 0°$ and $D = 75\%$, the output voltage only varies from 0 to $V_{1,\mathrm{DC}}$ but the frequency is doubled. In addition, a single leg behavior can be also achieved. In (d) with $\phi = 90°$ and $D = 75\%$, the voltage also varies from 0 to $V_{1,\mathrm{DC}}$, with the same frequency and duty cycle as a single leg would perform.

or S_3) is ON the lower (S_2 or S_4) is OFF and vice versa. The control can implemented by varying the time that each of the semiconductors is conducting, called the duty-cycle D. Or, in addition, the phase between the legs ϕ can also be modified. This way, many output voltage waveforms can be achieved, see Figure 2.4.

Regardless of the chosen strategy, all the waveforms are periodical, so they can be represented by Fourier transforms. Thus, the input AC

voltage v_1 of the transformer will be given by

$$v_1(t) = \underbrace{(2D-1)V_{1,\mathrm{DC}}}_{\text{DC component}} + \underbrace{\sum_{n=1}^{\infty} \frac{2V_{1,\mathrm{DC}}}{n\pi} \sin(n\pi D)\left(\cos(n\omega t) + (-1)^n \cos(n(\omega t + \phi))\right)}_{\text{AC component}}, \tag{2.12}$$

where n stands for the harmonic number and ω is the angular speed ($\omega = 2\pi f$). When $\phi = 180°$ the two legs are in counter-phase.

According to [Garcia Bediaga, 2014], the most well-known control and modulation strategies that are implemented by varying f, D and φ are:

- Square-wave modulation: a constant frequency with a duty-cycle of 50% is implemented and the angle between the two phases is $\varphi = 180°$, see Figure 2.4(a). This way, the DC component, useless in magnetic power transfer (only adds losses), is removed. In addition, Zero-Voltage-Switching (ZVS) is achieved for almost all power ranges.

- Frequency modulation: also with $D = 50\%$, the frequency enables the regulation of the voltage of the converter. Nevertheless, high-frequency operation is limited, due to the increased device losses and their thermal limits.

- Phase-shift modulation: varies the angle between the phases φ. The main drawbacks are the existing DC current and the fact that ZVS may be lost when it operates in discontinuous mode.

2.2.2 Square wave modulation

During this procedure towards IPT, square-wave modulation with constant frequency will be used, since it will be the final control developed in Chapter 3 and Chapter 4. Thus, with $D = 50\%$ and $\varphi = 180°$, equation (2.12) is simplified into

$$v_1(t) = \sum_{n=1}^{\infty} \frac{4V_{1,\mathrm{DC}}}{n\pi} \sin(\frac{1}{2}n\pi)\cos(n\omega t)\,. \tag{2.13}$$

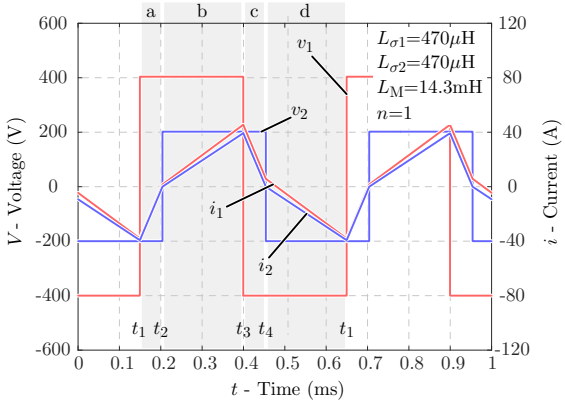

Figure 2.5: v_1 and v_2 AC voltages and i_1 and i_2 AC currents, for $V_{1,\mathrm{DC}} = 400$, $V_{2,\mathrm{DC}} = 200$ and $f = 2\mathrm{kHz}$. The difference between i_1 and i_2 is the magnetizing current i_{M} neglected in (2.15).

The sequence of the square-wave modulation eases soft switching, reducing considerably the total switching losses of the power converter. Using as example the transformer designed in [Villar, 2010], Figure 2.5 represents the current and voltage waveforms of a SAB. It has to be mentioned that in [Villar, 2010] this transformer was supplied a DAB but it can also be used with a SAB, since it is a particular case of a DAB. This transformer, is designed to work at a switching frequency of $f_{\mathrm{sw}} = 2\mathrm{kHz}$ and a power of 3.9kW with both DC voltages that can increase up to 400kV.

Four states can be differentiated (see Figure 2.6):

- State a, Figure 2.6(a): the diode D_1 is in conduction. The semiconductor S_1 has to be turned-on before the transition t_2, while the diode is conducting. This way, zero voltage switching ZVS is achieved.

- State b, Figure 2.6(b): the transition t_2 happens when the sign of the current changes and S_1 starts conducting, reaching state b. During this state S_1 and S_4 conduct the current. This state is finished when S_1 and S_4 are turned off in t_3. Since the switching is done while the current is circulating, it will generate losses.

- State c, Figure 2.6(c): since the current can no longer go form the

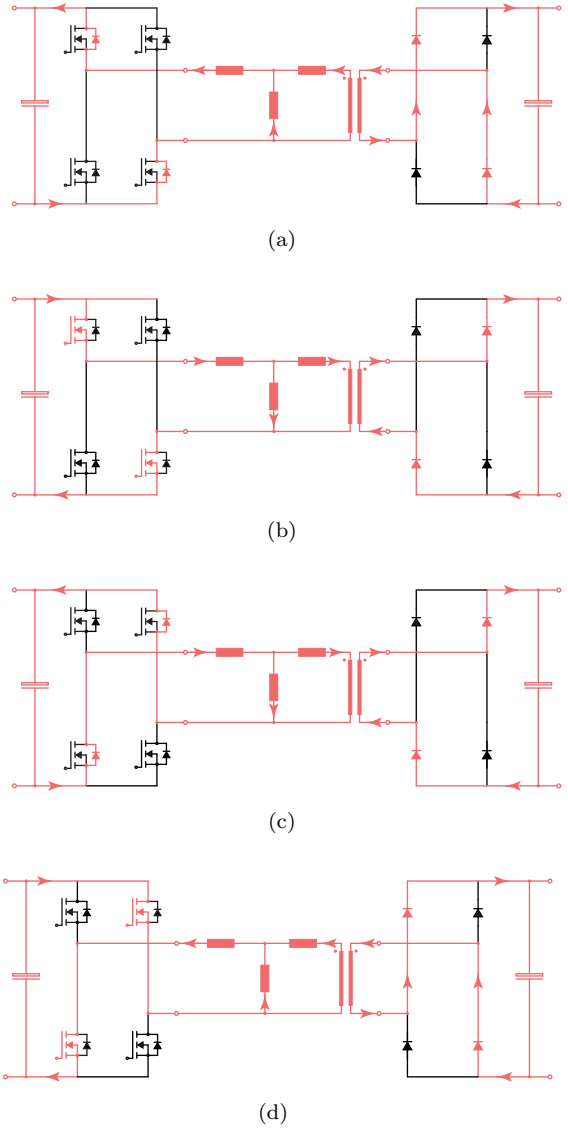

Figure 2.6: States of a SAB converter with square-wave modulation.

semiconductors, the diodes D_2 and D_3 start conducting. During this state, S_2 and S_3 are turned on, also in ZVS. Once the current changes polarity in t_4 state d starts.

- State d, Figure 2.6(d): during this state S_2 and S_3 are conducting until t_1 when they are turned off, with losses, and the cycle starts again.

Similar to the grid connected transformers, conductive chargers use ferromagnetic cores. In this case, as a higher frequency is used, the core materials change. Between 1kHz and 25kHz, nanocrystalline or amorphous alloy cores are used. With their relatively high-saturation magnetic induction, 1.5T and ∼1.2T respectively, losses are greatly reduced, that make them suitable for this frequency range. Above 25kHz, ferrite cores are used. The low-loss densities make them appropriate for higher frequencies [Villar, 2010]. Thanks to this cores, as for the grid connected transformers, the magnetizing inductance is much larger than the stray one. Thus, as for the low frequency transformer, for the calculation of the transmitted power, the current circulating through the magnetizing inductance, i.e i_{M} becomes negligible.

2.2.3 SAB output power

As previously stated, one of the advantages of ICC is the power flow control. With the square wave modulation, the control is done by varying the DC voltages at the input ($V_{1,\mathrm{DC}}$) and the output ($V_{2,\mathrm{DC}}$) by external DC/AC converters. Since i_{M} is neglected, the power flow can be represented by just the leakage inductances $L_{\sigma 1}$ and $L_{\sigma 2}$. In [Chéron, 1992], this calculation was done for a AC inverter connected to a diode bridge interfaced by an inductance connected in series. In [Garcia Bediaga, 2014] this equation was adjusted for a transformer, taking into account the transformation relation n_{T}. Thus, the average output current is

$$i_{2,\mathrm{DC}_{\mathrm{av}}} \approx \frac{n_{\mathrm{T}} \left(V_{1,\mathrm{DC}}^2 - (n_{\mathrm{T}} V_{2,\mathrm{DC}})^2\right)}{8(L_{\sigma 1} + n_{\mathrm{T}} L_{\sigma 2}) V_{1,\mathrm{DC}} f}, \tag{2.14}$$

and the output power will be given by

$$P_{\mathrm{out}} = V_{2,\mathrm{DC}} i_{2,\mathrm{DC}_{\mathrm{av}}} \approx \frac{V_{2,\mathrm{DC}} n_{\mathrm{T}} \left(V_{1,\mathrm{DC}}^2 - (n_{\mathrm{T}} V_{2,\mathrm{DC}})^2\right)}{8(L_{\sigma 1} + n_{\mathrm{T}} L_{\sigma 2}) V_{1,\mathrm{DC}} f}. \tag{2.15}$$

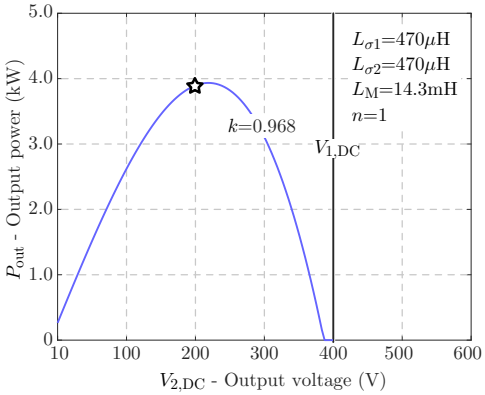

Figure 2.7: Ideal output power with respect to the output voltage. The transformer was designed in [Villar, 2010] for a DAB. The waveforms of the star point are represented in Figure 2.5.

Figure 2.7 represents the output power P_{out} for different output voltages, $V_{2,DC}$. The start points indicate the output power for the waveforms previously presented in Figure 2.5.

2.3 Transition to Inductive Power Transfer (IPT)

In the very basic concept conductive charges or IPT systems are equal. The difference is that in IPT systems, instead of having a magnetic core, the transmission is done through the air. This way, the space in which the secondary can be moved is greatly increased, which is specially convenient when this coil is placed in a moving environment, like for example a vehicle. Removing the core changes the proportion between the leakage inductances and the mutual inductance. L_σ is increased up to values comparable to L_M. Hence, the magnetizing current can no longer be ignored.

2.3.1 Voltage equivalent circuit

Since in IPT applications the voltage conversion is not so important or at least is not the first objective, a different equivalent circuit is

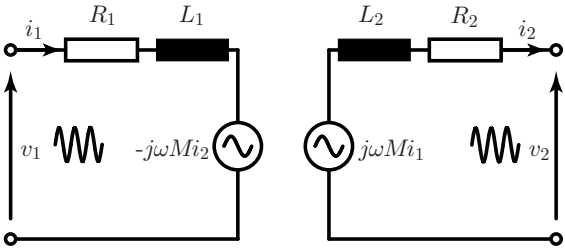

Figure 2.8: Voltage equivalent circuit. The resistances R_1 and R_2 represent the losses in the wiring.

typically used: the *Voltage Equivalent Circuit* [Van Schuylenbergh and Puers, 2009], see Figure 2.8.

In this case, the magnetic field representation is done slightly different. The field that is generated by the transmitter coil is represented by L_1. It represents both, the stray field and the linked one. So, it is obtained by adding up both terms, i.e

$$L_1 = L_{\sigma 1} + L_{\mathrm{M}}. \tag{2.16}$$

The linked magnetic field is represented by the mutual inductance M. It is introduced in the voltage source that represents the opposition effect that is created, as explained in *Faraday's law* (2.2). The difference with the magnetizing inductance is just the transformation ratio, i.e

$$M = \frac{L_{\mathrm{M}}}{n}. \tag{2.17}$$

Finally, the field that is created by the secondary coil is represented by L_2. In this case, considering a magnetizing inductance referred to the secondary, the value is obtained by

$$L_2 = L_{\sigma 2} + \frac{L_{\mathrm{M}}}{n^2}. \tag{2.18}$$

Measuring these values is rather simple. L_1 and L_2 can be measured having the counterpart coil in open circuit. Besides, M can be obtained measuring the induced voltage at the coil that is not carrying current.

In order to have a value that quantifies how much of the created field is actually being used, the coupling coefficient k is defined

$$k = \frac{M}{\sqrt{L_1 L_2}}. \tag{2.19}$$

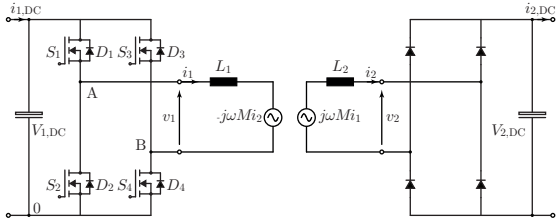

Figure 2.9: Inductive power transfer equivalent circuit. The primary coil is supplied by a Full-Bridge and the secondary side is rectified by a diode bridge.

This value varies between 0 and 1, where 0 is no coupling at all and 1 will represent a completely linked field. In classical transformers and conductive chargers, this value is close to 1, 0.97 for the graphs shown in Section 2.3. In IPT applications this value is typically below 0.5.

So, equation (2.5) can be rearranged as

$$\begin{aligned} \vec{v_1} &= L_1 \frac{\mathrm{d}\vec{i_1}}{\mathrm{d}t} - M \frac{\mathrm{d}\vec{i_2}}{\mathrm{d}t} \\ \vec{v_2} &= M \frac{\mathrm{d}\vec{i_1}}{\mathrm{d}t} - L_2 \frac{\mathrm{d}\vec{i_2}}{\mathrm{d}t}, \end{aligned} \tag{2.20}$$

leading to a equivalent circuit depicted in Figure 2.9.

2.3.2 Square wave modulation in IPT systems

For the square wave modulation in IPT systems the switching sequence is exactly equal to the one presented for the ICC. In Figure 2.10 the waveforms are depicted for a input voltage of $V_{1,\mathrm{DC}} = 400$ and three different coupling coefficients: $k = 0.968$ (the same as Figure 2.5 only with different $V_{1,\mathrm{DC}}$), $k = 0.8$ and $k = 0.5$. In each variation of k, M is recalculated, keeping the same value of L_1 and L_2.

The effect of the coupling coefficient can be explained by analyzing equation (2.20). Since for this particular example $L_1 = L_2$ then $M = kL_1$ is fulfilled and the currents will be given by

$$\frac{\mathrm{d}\vec{i_1}}{\mathrm{d}t} = \frac{k\vec{v_2} - \vec{v_1}}{L_1\left(k^2 - 1\right)} \tag{2.21a}$$

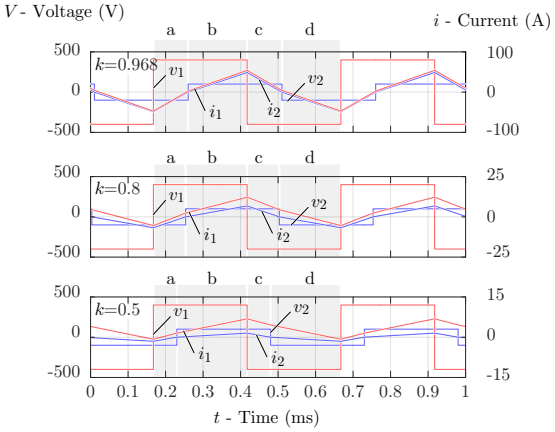

Figure 2.10: Input and output voltage and current waveforms for $V_{2,\mathrm{DC}} =$ 200V for coupling coefficients k =0.968, 0.8 and 0.3 of Figure 2.11.

$$\frac{\mathrm{d}\vec{i_2}}{\mathrm{d}t} = \frac{\vec{v_2} - k\vec{v_1}}{L_1\left(k^2 - 1\right)}. \tag{2.21b}$$

In Figure 2.10 it can be observed that the time that each state is given varies with the coupling coefficient. The lower the coupling the shorter the time that the diodes are conducting, i.e. a and c states. Thus, since the period is equal, the states b and d become larger. Apart from the state time variations, decreasing the coupling separates the input and output currents since the numerator of both currents tend to separate. Since v_1 has to be larger than v_2 to polarize the diodes, i_2 will decrease faster than i_1. Up to the point that the secondary current can be almost extinct but still current in the primary coil will be circulating. Apart from that, the magnitude of both currents is also reduced, due to the incement of the denominator. Already with a coupling of 0.8 the current is almost 10 times smaller than for 0.968.

2.3.3 SAB output power

In Figure 2.11 the output power with respect to the output voltage is represented for different coupling coefficients. As expected, considering that the currents have decreased by an order of magnitude, the power has greatly decreased with the reduction of the coupling. Comparing

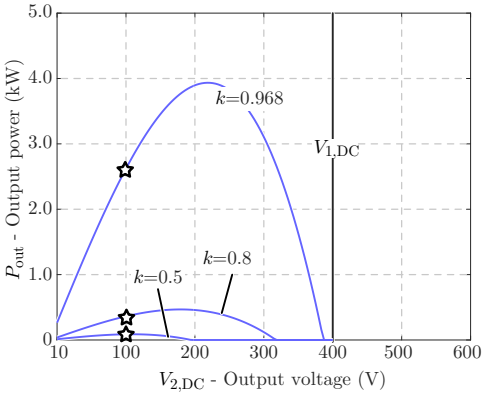

Figure 2.11: Output power respect to the output voltage for different coupling coefficients, varying the self inductances and the mutual inductance. The star point are depicted in Figure 2.10.

the three star points, (whose waveforms were depicted in Figure 2.10), it can be seen that with a coupling coefficient 0.5 the power that is being transmitted is 300W. It is 80 times smaller than when the coupling is 0.968. In addition, the control range is shrunk. The divider created by the self and the magnetizing inductance reduce the voltage seen by the AC side of the diode bridge, thus the maximum $V_{2,DC}$ that will actually transmit power is only $kV_{1,DC}$. In order to improve the power capability and efficiency of the system resonant capacitors are used. This way, the self impedances of the primary and secondary coils are compensated and the impedance divider disappears.

2.4 Resonant IPT

Basically by introducing capacitors in the system a band pass filter is created, see Figure 2.12. The low frequency harmonics are stopped by the capacitance, with a damping of 20dB/dec, and the high frequencies by the series inductances similarly with a damping factor of 20dB/dec. At the resonant frequency (f_0), the input impedance is at its minimum. In addition, as the input square wave voltage has also a drop of 20dB/dec, the current that circulates through the primary side, exhibits a 40dB/dec attenuation. It entails that the third current harmonic is already almost 20dB smaller than the fundamental and the

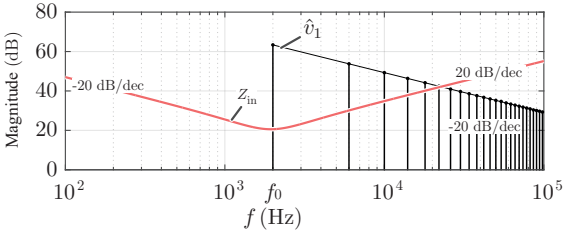

Figure 2.12: Bode diagram of a RLC resonant system. Below resonance frequency (f_0) the impedance amplitude decreases by 20dB/dec. Above f_0 it increases by 20dB/dec.

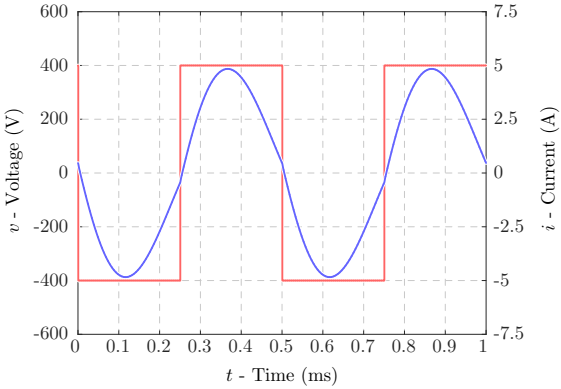

Figure 2.13: Waveform of a IPT system with resonant capacitors. The current is practically fully described by the first harmonic.

fifth one is about 30dB smaller. Therefore, the waveform of the current is almost fully described by just the first harmonic, see Figure 2.13. Furthermore, the current and the voltage are completely in phase. So it can be concluded that the input impedance is purely resistive or in other words the imaginary part of it is zero.

This enables the simplification of the analysis and design of SAB for IPT systems. The primary side inverter can be substituted by an AC voltage source, being the voltage the first harmonic of the square wave (2.13)

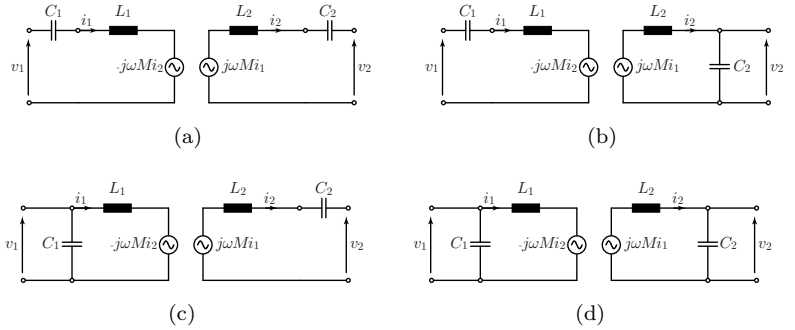

Figure 2.14: Compensation topologies used in IPT systems. (a) Series-Series compensation. (b) Series-Parallel compensation. (c) Parallel-Series compensation. (d) Parallel-Parallel compensation.

$$\vec{v}_1 = \frac{4V_{1,\mathrm{DC}}}{\pi}\cos(\omega t)\,. \tag{2.22}$$

Apart from that, also the load can be substituted. In this case by an equivalent resistance, whose value will depend on compensation topology. Unlike in ICC, since in IPT systems the coupling is low the compensation of the each coil is done separately. In single phase IPT systems mainly four compensation configurations are used:

- Series-Series compensation, Figure 2.14(a).
- Series-Parallel compensation, Figure 2.14(b).
- Parallel-Series compensation, Figure 2.14(c).
- Parallel-Parallel compensation, Figure 2.14(d).

Series resonant sides are fed by voltage-type converters, i.e. the energy is stored in capacitive buses. In contrast, parallel resonant circuits are supplied by current-type converters, i.e the energy is stored in inductances. Other type of combinations can also be found in literature, such as the CCL [Villa et al., 2012] or the CLCL [Thrimawithana and Madawala, 2013, Swain et al., 2014]. In this work, as the SAB is a voltage driven converter, the first two topologies are going to be analyzed.

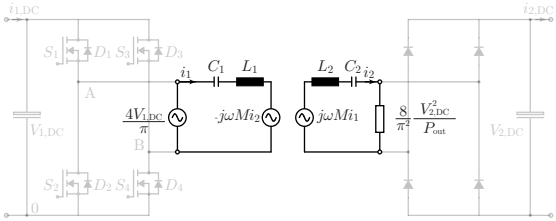

Figure 2.15: Series-series compensation first harmonic equivalent circuit. The primary inverter is replaced by a voltage source and the rectifier plus the load is substituted by an equivalent resistance.

2.4.1 Series-Series compensation

The Series-Series compensation is used when both sides of the inductive link are driven by voltage source converters. In the case of a SAB converter, considering a constant voltage $V_{2,\mathrm{DC}}$ at the DC side of the diode bridge, the AC magnitude $\hat{v}_2$ is given by

$$\hat{v}_2 = \frac{4}{\pi} V_{2,\mathrm{DC}}. \tag{2.23}$$

Then, as the DC current $i_{2,\mathrm{DC}}$ is a rectified sinusoidal wave, the relation between AC i_2 and DC is

$$i_{2,\mathrm{DC}} = 2f \int_0^{\frac{1}{2f}} \hat{i}_2 \sin(\omega t) = \frac{2}{\pi} \hat{i}_2. \tag{2.24}$$

Thus, the equivalent AC resistance R_{AC} is

$$R_{\mathrm{AC}} = \frac{\hat{v}_2}{\hat{i}_2} = \frac{\frac{4}{\pi} V_{2,\mathrm{DC}}}{\frac{\pi}{2} i_{2,\mathrm{DC}}} = \frac{8}{\pi^2} R_{2,\mathrm{DC}} = \frac{8}{\pi^2} \frac{V_{2,\mathrm{DC}}^2}{P_{\mathrm{out}}}. \tag{2.25}$$

Once the equivalent input voltage and the output load are known, as depicted in Figure 2.15 , the equations of the SAB (2.20) are rearranged as

$$\begin{aligned} \vec{v_1} &= \underbrace{\left(\frac{1}{j\omega C_1} + j\omega L_1\right)}_{\mathrm{Z_1}} \vec{i_1} - j\omega M \vec{i_2} \\ R_{\mathrm{AC}} \vec{i_2} &= j\omega M \vec{i_1} - \underbrace{\left(j\omega L_2 + \frac{1}{j\omega C_2}\right)}_{\mathrm{Z_2}} \vec{i_2} \end{aligned} \tag{2.26}$$

So, in order to make the system resonate at f_0, Z_1 and Z_2 must be zero. Hence, the capacitors should be tunned by

$$C_1 = \frac{1}{w_0^2 L_1} \tag{2.27a}$$

$$C_2 = \frac{1}{w_0^2 L_2}. \tag{2.27b}$$

Developing the equation, the mutual inductance that must have the IPT system can be obtained. In a typical IPT system the value of the mutual inductance changes depending on the distance. Thus, this equation should be applied to the point where maximum coupling is expected. As it can be noticed, even though it may sound senseless, when the mutual inductance decreases the output increases. Clearly, up to the limit that the inverters can handle, in and ideal case,

$$M = \frac{8}{\pi^2} \frac{V_{1,\mathrm{DC}} V_{2,\mathrm{DC}}}{w_0 P_{\mathrm{out}}}. \tag{2.28}$$

Besides, the input impedance of the system will be given by

$$Z_{\mathrm{in}} = \frac{\vec{v_1}}{\vec{i_1}} = \frac{\left(\omega^2 M\right)^2 + j\omega L_1 \left(\omega^2 - \omega_0^2\right) R_{\mathrm{AC}} - L_1 L_2 \left(\omega^2 - \omega_0^2\right)^2}{\omega \left(j \left(\omega^2 - \omega_0^2\right) L_2 + \omega R_{\mathrm{AC}}\right)} \tag{2.29}$$

So it is in resonance when

$$\Im\left(Z_{\mathrm{in}}\right) = \frac{\left(\omega^2 - \omega_0^2\right)\left(\left(\omega^2 - \omega_0^2\right)^2 L_1 L_2^2 + L_1 R_{\mathrm{AC}}^2 \omega^2 - \left(\omega^2 M\right)^2 L_2\right)}{\omega\left(\left(\omega^2 - \omega_0^2\right)^2 L_2^2 + \omega^2 R_{\mathrm{AC}}^2\right)} = 0. \tag{2.30}$$

According to (2.30) the imaginary part can be zero more than ones. The first one is clear that when $\omega = \omega_0$ is fulfilled. This point is independent on the parameters of the inductive link, as long as the capacitor is well selected to be in resonance. So, the input impedance will be

$$Z_{\text{in},\omega=\omega_0} = \frac{\omega_0^2 k^2 L_1 L_2}{R_{\text{AC}}} \tag{2.31}$$

The other two resonance points directly depend on the parameters of the system. This effect is known in the literature as bifurcation or pole-splitting [Wang et al., 2004]. Typically, it is analyzed finding the limits for k (2.32a) and P_{out} (2.32b).

$$k_{\text{lim}} = \frac{8}{\pi^2} \frac{V_{2,\text{DC}}^2}{w_0 L_2 P_{\text{out}}} \tag{2.32a}$$

$$P_{\text{out,lim}} = \frac{8}{\pi^2} \frac{V_{2,\text{DC}}^2}{k w_0 L_2} \tag{2.32b}$$

Figure 2.16 shows the input impedance magnitude and phase for different output powers and coupling coefficient for the transformer designed in [Villar, 2010] but with a nominal coupling coefficient of 0.3 and an output power of 30kW. The coupling limit is established in 0.1761 and the power limit is 17.6kW. In Figure 2.16(a) different coupling coefficients are analyzed. It can be seen that exceeding the limit creates more than one zero crossing at the phase angle. Figure 2.16(b) shows the same input impedance but varying the output power. Depending on the power being transmitted, the impedance varies.

The intuitive explanation behind pole-splitting is as follows. Increasing the coupling makes the self inductance interact with the capacitor of the counterpart coil, creating an extra resonance. Identically, increasing the output power, increases the current circulating, thus the effect between the coils is magnified. This also creates new resonant points, separated from f_0.

Apart form the two aforementioned limits, in [Iruretagoyena et al., 2017a] another limit is described. In this study a system with a constant mutual inductance given by (2.28) is analyzed. The relation between the receiver self inductance and the transmitter self inductance, χ (2.33), is used as parameter. It has to be remarked that unlike the coupling and the output power, the inductance ratio does not change during operation. Thus, this limit only applies during the design process.

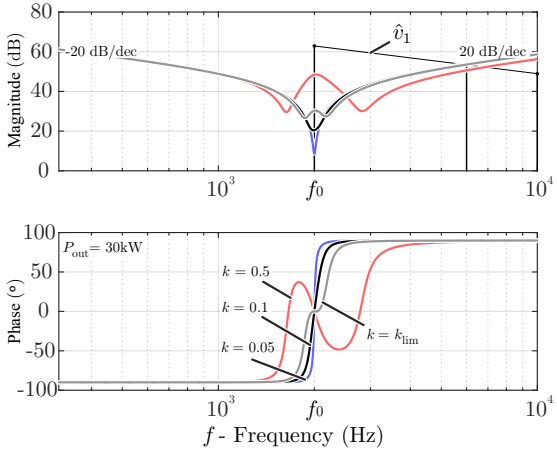

(a)

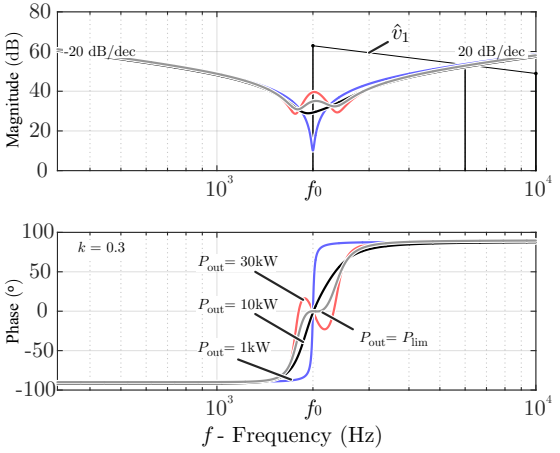

(b)

Figure 2.16: Input impedance magnitude and amplitude (a) varying the coupling coefficient and (b) varying the output power.

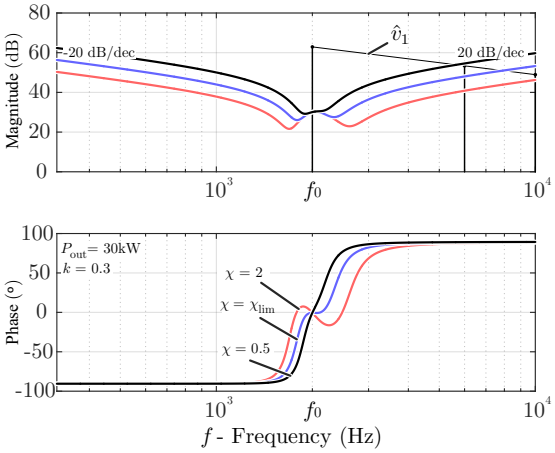

Figure 2.17: Input impedance magnitude and amplitude varying the relation between self inductances.

$$\chi = \frac{L_2}{L_1} \tag{2.33}$$

The inductance ratio limit is given by

$$\chi_{\text{lim}} = \left(\frac{V_{2,\text{DC}}}{V_{1,\text{DC}}}\right)^2. \tag{2.34}$$

So for the presented example the limit is when $\chi = 1$. Figure 2.17 depict the input impedance for different inductance ratio. It is observed that any system with any power or coupling coefficient can be free of pole-splitting if during the design process (2.34) is fulfilled.

2.4.2 Series-Parallel compensation

The Series-Parallel compensation is used when the primary side is voltage source driven and the secondary side current source driven, see Figure 2.18. During this analysis the secondary DC side current $i_{2,\text{DC}}$ is a controlled parameter. The relation of the DC and AC current is identical to the voltage for the primary side, i.e.

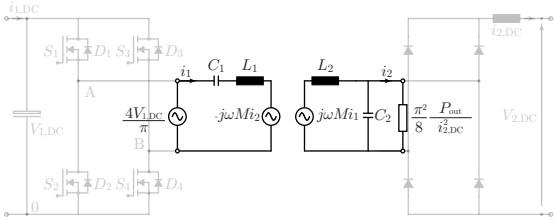

Figure 2.18: Series-parallel compensation first harmonic equivalent circuit. The primary inverter is replaced by a voltage source and the rectifier plus the load is substituted by an equivalent resistance.

$$\hat{i}_2 = \frac{4}{\pi} i_{2,\mathrm{DC}}. \tag{2.35}$$

Similarly to the primary side current, the secondary voltage is given by

$$V_{2,\mathrm{DC}} = \frac{2}{\pi} \hat{v}_2. \tag{2.36}$$

So, for the Series-Parallel compensation, the equivalent resistance will be

$$R_{\mathrm{AC}} = \frac{\pi^2}{8} \frac{P_{\mathrm{out}}}{i^2_{2,\mathrm{DC}}}. \tag{2.37}$$

Therefore, the equivalent circuit equations can be described by the following equations

$$\begin{aligned}
\vec{v_1} &= \underbrace{\left(\frac{1}{j\omega C_1} + j\omega L_1\right)}_{\mathrm{Z_1}} \vec{i_1} - j\omega M \vec{i_{2,\mathrm{L}}} \\
j\omega M \vec{i_1} &= \underbrace{j\omega L_2 \vec{i_{2,\mathrm{L}}} + \frac{1}{j\omega C_2} \vec{i_{2,\mathrm{C}}}}_{Z_2} \\
\frac{1}{j\omega C_2} \vec{i_{2,\mathrm{C}}} &= R_{\mathrm{AC}} \vec{i_2} \\
\vec{i_{2,\mathrm{L}}} &= \vec{i_{2,\mathrm{C}}} + \vec{i_2}.
\end{aligned} \tag{2.38}$$

The simplest way of calculating the value of the resonance capacitor is to set C_2 equal to (2.27b) [Knecht and Kolar, 2017]. Then, the primary side resonance capacitor C_1 is

$$C_1 = \frac{L_2}{\omega_0^2 \left(L_1 L_2 - M^2\right)} = \frac{1}{\omega_0^2 L_1 (1 - k^2)}. \tag{2.39}$$

It can be observed that the value that is needed varies with the mutual inductance. In other words, if the coupling coefficient changes, as the capacitor will have a fixed value, the resonance frequency will change. Furthermore, the resonance frequency of the primary and secondary will be different, thus adjusting the switching frequency can not solve the problem. Despite this drawback, the main advantage of a Series-Parallel compensation is that the current circulating through the capacitor is much lower than for the Series-Series. It is specially convenient at very high power [Bosshard et al., 2015], where it can be difficult and expensive to find a capacitor capable of withstanding all the current.

Continuing the calculations, the desired mutual inductance to transmit a certain power is given by

$$M = \frac{8}{\pi^2} \frac{V_{1,\mathrm{DC}} L_2 i_{2,\mathrm{DC}}}{P_{\mathrm{out}}}, \tag{2.40}$$

and the input impedance will be

$$Z_{\mathrm{in}} = \frac{L_1(\omega - \omega_0)^2(k^2 - 1)\left(R_{\mathrm{AC}}(\omega - \omega_0) - jL_2\omega\omega_0^2\right) + L_1 R_{\mathrm{AC}}(k\omega\omega_0)^2}{\omega\left(L_2\omega\omega_0^2 + jR_{\mathrm{AC}}\left(\omega^2 - \omega_0^2\right)\right)}. \tag{2.41}$$

The imaginary part of the input impedance is given by

$$\Im\left(Z_{\mathrm{in}}\right) = \frac{L_1\left(\omega_0^2 - \omega^2\right)\left(A + \left(\omega\omega_0^2 L_2\right)^2\left(k^2 - 1\right)\right)}{\omega\left((L_2\omega\omega_0^2)^2 + R_{\mathrm{AC}}\left(\omega^2 - \omega_0^2\right)^2\right)} \tag{2.42}$$

where

$$A = R_{\mathrm{AC}}^2\left(\left(\omega^2 - \omega_0^2\right)^2\left(k^2 - 1\right) + k^2\omega^2\omega_0^2\right). \tag{2.43}$$

Once again, the straightforward zero is given when $\omega = \omega_0$. At this point the input impedance is

$$Z_{\mathrm{in},\omega=\omega_0} = \frac{L_1 k^2 R_{\mathrm{AC}}}{L_2} \tag{2.44}$$

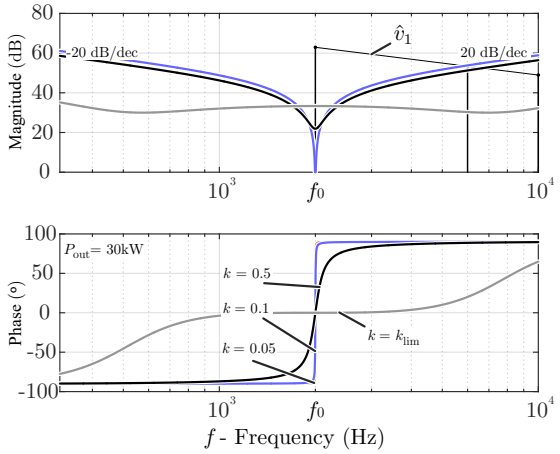

(a)

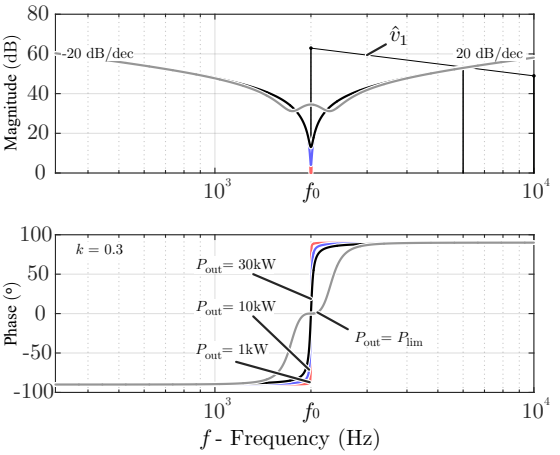

(b)

Figure 2.19: Input impedance magnitude and amplitude (a) varying the coupling coefficient and (b) varying the output power for the Series-Parallel compensation.

Also, more than one zero can be obtained. Given the coupling coefficient and power limits by

$$k_{\text{lim}} = \frac{L_2 i_{2,\text{DC}}^2 \omega_0}{\sqrt{\left(L_2 i_{2,\text{DC}}^2 \omega_0\right)^2 + \left(\frac{\pi^2}{8} P_{\text{out}}\right)^2}} \tag{2.45a}$$

$$P_{\text{out,lim}} = \frac{8}{\pi^2} \frac{\omega_0 L_2 i_{2,\text{DC}}^2 \sqrt{1-k^2}}{k} \tag{2.45b}$$

Figure 2.19(a) and Figure 2.19(b) show some interesting behavior compared to the series-series compensation. The coupling limit and transferred power limit are much higher with Series-Parallel topology (see Figure 2.16(a) and Figure 2.16(b)). It is due to the fact that the current circulating through the secondary capacitor is much smaller. Being so, reduces the interaction between the two resonant tanks. Up to the point that the bifurcation appears way over the nominal point of the system.

However, the bifurcation problems in Series-Series topologies can be avoided by design, respecting the aforementioned limits. Still, the problem of varying the resonance point in Series-Parallel systems must be handled.

Summarizing, in applications where the secondary side is driven by a current source, with a coupling that does not change and for very high power applications, Series-Parallel is preferred. On the contrary, for the rest of the cases (i.e voltage sources, varying coupling or low power), Series-Series compensation is the better choice.

2.4.3 Resonant SAB output power

As previously mentioned, the main objective of introducing resonance is to make the system capable of transmitting power at low coupling coefficients. Rearranging equation 2.28 leads to

$$P_{\text{out}} = \frac{8}{\pi^2} \frac{V_{1,\text{DC}} V_{2,\text{DC}}}{\omega M}. \tag{2.46}$$

From equation (2.46), it can be deduced that if the frequency is kept constant at the resonance value, the transmitted power is going to be linear to the input and output DC voltages. However, in a real situation working at the exact resonance is almost impossible, since

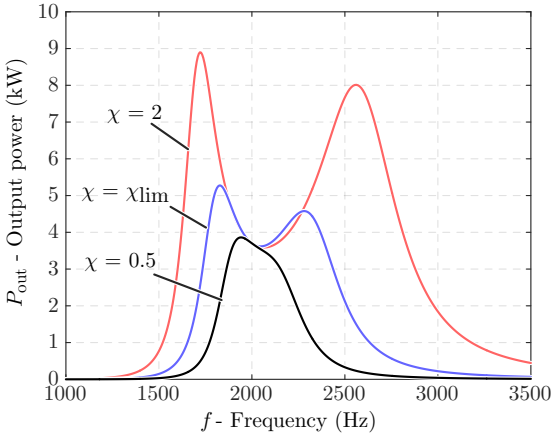

Figure 2.20: Output power vs. switching frequency for different inductance ratios. If χ_{lim} is exceeded two peaks appear.

the values of the inductances will not be exactly the desired value and the capacitors can be only found in discrete values. Even though the real resonance value will not greatly differ from the ideal case, it is interesting to analyze the behavior of the output power for different switching frequencies.

In Figure 2.20 the output power with respect to the switching frequency is depicted for different inductance ratios and a series-series compensation. It has to be mentioned that for the coupling coefficient limit (2.32a) or the power limit (2.32b) produces the same effect. It can be observed that with an inductive link with a pole-splitting, it exhibits two peaks. Even with the exact limit the two peaks appear (in the exact limit two resonance points can be found). These values are much higher than for the designed resonance frequency. However, the peaks are not created exactly at the two extra resonance points. So which is the cause to have two peaks? And how is it possible to have higher value than the ideal resonance? The real part of the input impedance always has a single maximum peak, regardless if there is pole-splitting or not. This peak is always given at the desired resonant point f_0. Thus, the other two resonant points will exhibit a smaller impedance, as it can be seen in Figure 2.17. That makes the current higher and as a consequence the induced voltage is also higher. Leading to a higher transmitted power.

So it can be concluded that, for the real case, if the system is far from the limits of pole-splitting and the frequency is not exactly the

resonance one, the output power will always be smaller. However, if the system is close or above the limit of the bifurcation, depending on the deviation, the power that is being transmitted can be higher. For this reason, from the reliability point of view is better to ensure that no pole-splitting occurs. Nevertheless, as it will be shown in Chapter 4, those extra peaks can also be used to adjust the transmitted power if the expected value at the resonance frequency is too low.

2.4.4 Zero Voltage Switching

As previously said, the system works in zero voltage switching conditions when it is in resonance. However, this is not completely true. The system must work in a slightly inductive zone (phase above zero) in order to discharge the output capacitor (C_{oss}) of the semiconductor during the dead time (t_{D}). In normal operation, inductive zone is achieved working at frequencies just higher than f_0. But, if the the system has pole-splitting, this will take the system to a capacitive zone, further increasing the switching losses.

Figure 2.21 depicts a switching transition from S_2 to S_1. The transition is as follows. Before t_1 the semiconductor S_2 is conducting and the counterpart output capacitance $C_{\text{oss},1}$ is charged to $V_{1,\text{DC}}$. When the current is close to zero (must be working in inductive zone), the semiconductor is turned off at t_1. Then, between t_1 and t_2 all the switches are open and the current flows freely between the output capacitances. This current discharges C_{oss_1} and transfers the energy to $C_{\text{oss},2}$. If the inductive energy is high enough, the voltage of $C_{\text{oss},2}$ will reach $V_{1,\text{DC}}$ before t_2, depicted in blue in Figure 2.21. However, if the current is too low, when S_1 is turned on in t_2, the voltage in C_{oss_1} will be lower and it will suddenly rise, creating a high current spike through S_1. Finally, after t_2, the current will circulate though S_1, while $C_{\text{oss},1}$ is charged to $V_{1,\text{DC}}$.

In order to calculate required switching current to achieve ZVS, two variables must be calculated. On the one hand, the energy that is needed to discharge $C_{\text{oss},1}$ and charge $C_{\text{oss},2}$. And on the other hand, the available inductive energy in load. In non-resonant tightly coupled systems, the magnetizing inductance is adapted to get enough inductive energy for the commutation [Kasper et al., 2016] and the switching current calculation is straightforward. However, in resonant systems, apart from the output capacitances, the resonant capacitor also absorbs

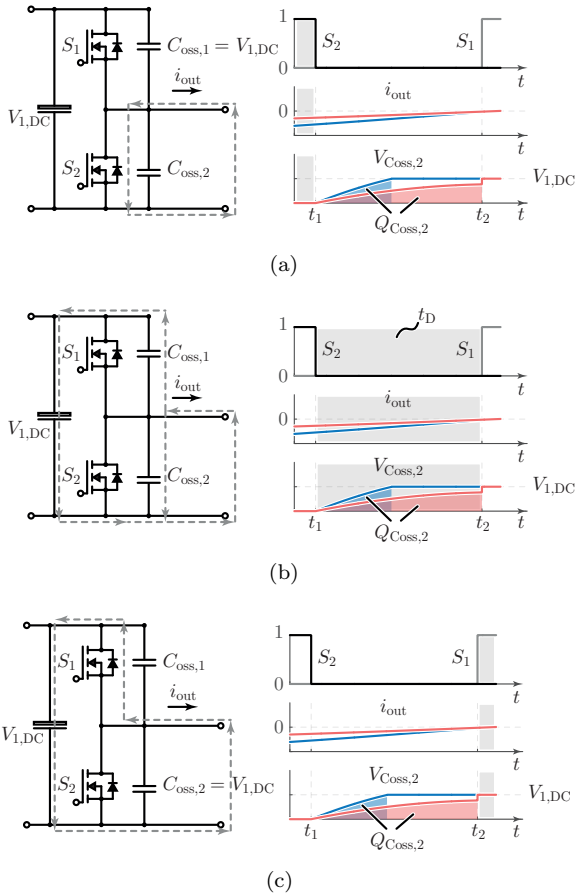

Figure 2.21: Switching transition from S_2 to S_1 of a bridge leg. (a) S_1 conduction interval. (b) Blanking time, depending on the output current (i_{out}) the energy between the output capacitors is shifted or not. If the current is too low, part of the energy is still in $C_{oss,1}$, thus ZVS is not achieved.(c) S_2 conduction interval.

this inductive energy. That is why parameters should be also taken into account in the calculation.

In Figure 2.22 the circuit during the commutation is depicted. During the dead time, the Fourier transforms can no longer be applied, since

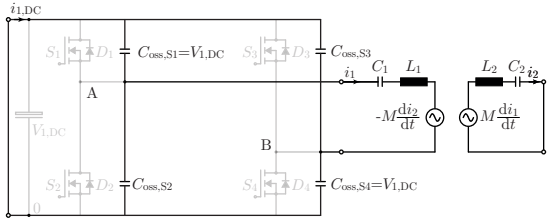

Figure 2.22: Circuit during the dead time t_D. All the voltage sources are short-circuited.

it is not a periodic waveform. Thus, the following differential equations must be analyzed

$$\overbrace{V_{Coss} + V_{C1}}^{V_{Ceq}} + L_1 \frac{di_1}{dt} + M \frac{di_2}{dt} = 0 \tag{2.47a}$$

$$M \frac{di_2}{dt} = V_{C2} + L_2 \frac{di_2}{dt} \tag{2.47b}$$

$$i_1 = C_{eq} \frac{dV_{Ceq}}{dt} \tag{2.47c}$$

$$i_2 = C_2 \frac{dV_{C2}}{dt} \tag{2.47d}$$

Solving the differential equation, the voltage of the output capacitances are obtained. If at $t = t_d$ V_{Coss} is higher than $V_{1,DC}$, means that ZVS is achieved. Otherwise, there is hard switching. This value exclusively depends on the initial conditions of $i_{1,0}, i_{2,0}$ and $V_{Ceq,0}, V_{C2,0}$, that will be imposed by the coupling and the load. For the series-series compensation V_{eq} is

$$\begin{aligned} V_{\mathrm{eq}} =& \cos\left(\frac{t_{\mathrm{d}}}{\sqrt{B}}\right) V_{\mathrm{Ceq},0} + \\ & C_2 M \frac{\cosh\left(\frac{t_{\mathrm{d}}}{\sqrt{A}}\right) - \cos\left(\frac{t_{\mathrm{d}}}{\sqrt{B}}\right)}{A+B} V_{\mathrm{C2},0} + \\ & M \frac{-A\sinh\left(\frac{t_{\mathrm{d}}}{\sqrt{A}}\right) + \sqrt{AB}\sin\left(\frac{t_{\mathrm{d}}}{\sqrt{B}}\right)}{\sqrt{A}\,(A+B)} i_{2,0} + \\ & \frac{\sqrt{B}\sin\left(\frac{t_{\mathrm{d}}}{\sqrt{B}}\right)}{C_{\mathrm{eq}}} i_{1,0} \end{aligned} \tag{2.48}$$

where

$$\begin{aligned} A &= (M - L_2)\, C_2 \\ B &= L_1 C_{\mathrm{eq}} \end{aligned} \tag{2.49}$$

and finally

$$V_{\mathrm{Coss}} = (V_{\mathrm{eq}} - V_{\mathrm{Ceq},0})\, \frac{C_{\mathrm{eq}}}{2C_{\mathrm{oss}}}. \tag{2.50}$$

Considering that the dead time is small compared to the waveform period, it can be said that it has no influence in the steady state waveforms. So, the initial conditions can be obtained from the Fourier equivalent equations previously presented. Since in IPT systems the coupling is very low, during ZVS the secondary side has practically no effect and the equivalent circuit can be simplified into a LC system. Thus equation (2.48) can be simplified into

$$V_{\mathrm{eq}} = \cos\left(\frac{t_{\mathrm{d}}}{\sqrt{B}}\right) V_{\mathrm{Ceq},0} + \frac{\sqrt{B}\sin\left(\frac{t_{\mathrm{d}}}{\sqrt{B}}\right)}{C_{\mathrm{eq}}} i_{1,0} \tag{2.51}$$

In (2.51) the two limits for achieving ZVS are represented. On the one hand, having enough inductive current ($V_{\mathrm{Ceq},0}$ and $i_{1,0}$ both depend on the coupling and the load). And on the other hand, enough dead time. If t_{d} is too small the energy will not be transmitted between the

capacitances before the semiconductor is turned on. The remaining or missing energy E_{rem} will turn into power losses (2.52).

$$P_{\text{sw}} = E_{\text{rem}} f_{\text{sw}} = \frac{1}{2} C_{\text{oss}} \left(V_{1,\text{DC}} - V_{\text{Coss}} \right)^2 f_{\text{sw}} \tag{2.52}$$

2.4.5 Experimental validation

In order to validate these concepts the prototype designed in [Villar et al., 2015] is adapted and forced to a bifurcated zone. The pole-splitting can be achieved by either, increasing the coupling by changing the separation between the coils or by changing the load, i.e. increasing the power. Since for this validation the load is going to be a resistance, its value is determined. The position of the receiver coil is going to be adjusted until a coupling with bifurcation is obtained. The parameters of the prototype are shown in Table 2.1.

Parameter	Variable	Value
Transmitter self inductance	L_1	131.5 μH
Receiver self inductance	L_2	62.27 μH
Transmitter resonance capacitor	C_1	20.95 nF
Receiver resonance capacitor	C_2	43.51 nF
Transmitter wire resistance	R_1	0.36 Ω
Receiver wire resistance	R_2	0.14 Ω
Transmitter resonance frequency	$f_{0,1}$	95.88 kHz
Receiver resonance frequency	$f_{0,2}$	96.69 kHz
Load resistance	R_{DC}	11.1 Ω
Maximum output power	$P_{\text{out,max}}$	3.2 kW
Input voltage	$V_{1,\text{DC}}$	330 V
Coupling coefficient	k	0.355

Table 2.1: Parameters of the prototype presented in [Villar et al., 2015]. The location of the receiver coil is changed to make the system bifurcated.

In order to select the position of the receiver coil, first the coupling limit where bifurcation appears must be calculated. Since the load is a resistance, and its voltage can not be regulated, the coupling limit shown in (2.32a) has to be adapted to

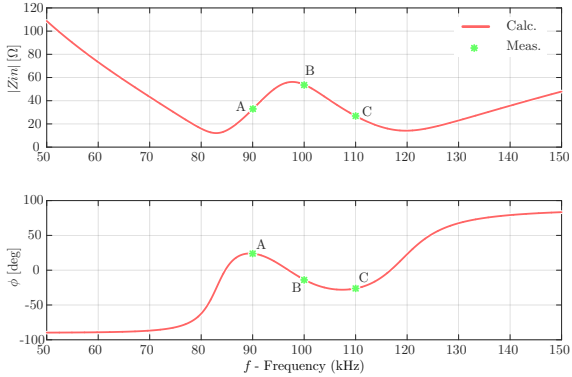

Figure 2.23: Input impedance for the IPT system presented in [Villar et al., 2015], with a load of 11.1Ω and a separation of 25mm. The waveforms of point A, B and C are depicted in Figure 2.24(a), Figure 2.24(b) and Figure 2.24(c) respectively.

$$k_{\text{lim}} = \frac{8}{\pi^2}\frac{R_{2,\text{DC}}}{\omega_0 L_2} = 0.23. \tag{2.53}$$

With both coils fully aligned and a separation of 25mm, a coupling coefficient value of 0.355 is measured. So, since $k > k_{\text{lim}}$, the system has pole-splitting, as it can be appreciated in the input impedance depicted in Figure 2.23.

In the ideal case, the system is designed to work at 100kHz. But, due to the manufacturing differences and the discrete values of the capacitors, this resonance point is established around 96kHz. In a system without bifurcation, this is not a problem. As previously said, an inductive zone is necessary to discharge the output capacitances, thus working at 100kHz will be ideal. However, as it can be seen in Figure 2.23, if the switching frequency is set to this value (point B), the system has a capacitive behavior.

The points A, B and C are depicted in Figure 2.24(a), Figure 2.24(b) and Figure 2.24(c) respectively. It can be seen that for the points B and C, a spike appears in the transmitter AC voltage and current during the switching transients. This is due to the discharging energy of the output capacitances that is going through the semiconductors.

In addition it can be observed that the peak value of the secondary

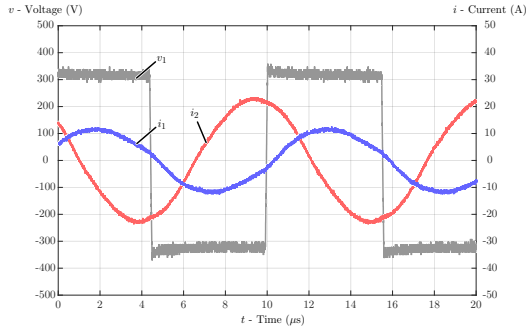

(a)

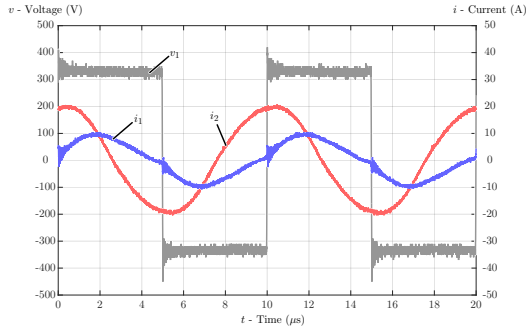

(b)

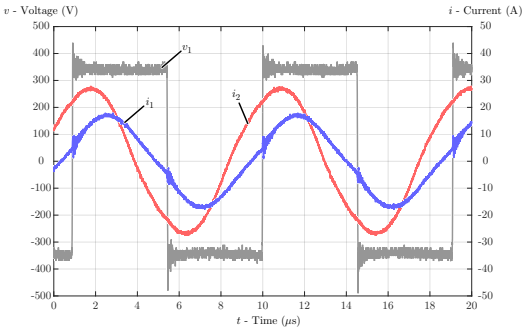

(c)

Figure 2.24: Transmitter AC voltage and AC current and receiver AC current, for the points A, B and C of Figure 2.23. (a) Point A, $f_{\text{sw}} = 90$ kHz. (b) Point B, $f_{\text{sw}} = 100$ kHz. (c) Point C, $f_{\text{sw}} = 110$ kHz.

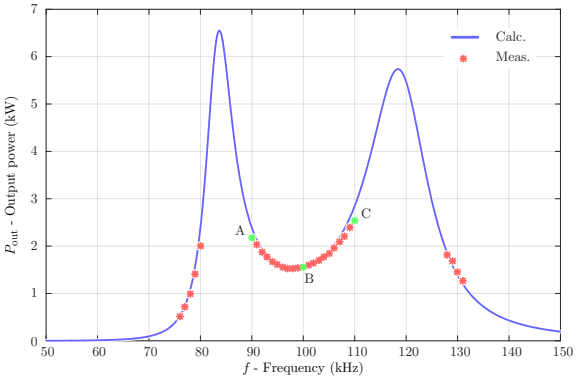

Figure 2.25: Output power P_{out} vs. switching frequency f_{sw}. It can be observed that two peaks appear due to the pole-splitting, much higher than the designed maximum power.

current for the C point is much higher than for the two other points. This means, that the transmitted power is higher at a point further than the ideal resonance point, which is higher than the designed maximum power $P_{\text{out,max}}$, as explained in section 2.4.3. Figure 2.25, depicts this fact. It can be seen that in the two other zeros (at approx. 82kHz and 119kHz) due to the pole-splitting, the transmitted power is way larger than the maximum power.

Finally, in Figure 2.26, the efficiency of the system (measuring from the AC grid to the load resistance) is represented. As it can be observed, the highest efficiency is achieved in the inductive zone close the the design resonance frequency.

2.5 System efficiency

It has been made clear that bifurcation is a problem regarding the efficiency of the system. But it is only one part among all the losses of the inductive link. Up to this point, during the calculations, the resistance inherent to the coils has been considered zero. But that is not true. There will be heating looses due to the circulating current. In addition, if ferrite cores are used to improve the coupling, this element will also have losses. That is only considering the coils set. In addition

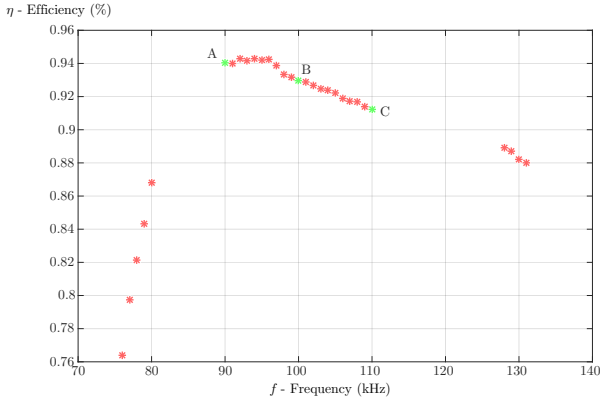

Figure 2.26: Efficiency η vs. frequency f. The highet efficiency is achieved in the inductive zone, close to designed resonance frequency, below 96kHz for this prototype.

the inverter will also be inefficient. Apart from the switching losses, conduction losses also will exist. In the following these aspects are going to be analyzed.

2.5.1 IPT link losses

As previously said, the losses in the IPT can be divided in two groups, wire losses and core losses. In [Villar, 2010] an exhaustive loss analysis is carried out for a medium frequency transformer. Most of the equations presented are applicable to IPT systems.

Wire losses

In medium-frequency applications, so as to carry the current, a certain effective conductor area is necessary. However this area can be too large for the frequency due to eddy current effects. The use of stranded insulated and twisted wires reduces these effects. This type of wires are known as Litz wires. According to [Villar, 2010] the losses in such wires can be divided into two groups, skin-effect losses and proximity losses. The first ones, represent the variation of the current distribution in the wire due to the field generated by the wire or the strand itself. The second one, represent also the variation of the current distribution

but due to the field generated by the neighboring strands (internal proximity effect) and the neighboring turns (external proximity effect). In the case of a transformer the external field path is well defined by the core. But, in IPT there is not such core so this equation is not applicable. Nevertheless, since the coil analyzed in this thesis has a meander shape and the coils are far from each other, this last effect is negligible.

Skin-effect

When a conductor carries AC current, due to the created magnetic field, an opposing current inside the conductor itself is generated. Therefore, the current density is reduced in the middle part and increased in the surface. The total current will be equal, however the current density will not be uniform anymore. The non-uniform distribution of the current density will be much more pronounced at higher frequencies. This penetration property is known as skin depth δ. It is defined as the radial distance from the outer surface of the conductor to an internal surface where the current density is 37% smaller. Being described by

$$\delta = \sqrt{\frac{1}{\pi\omega\mu\sigma}} \tag{2.54}$$

where μ is the permeability of the material and σ the conductivity. As detailed in [Villar, 2010] the skin effect losses can be accurately determined from the one-dimensional solution first developed by [Lammeraner and Štafl, 1966] and then improved by [Ferreira, 1992]. The term resistance factor F_{R} is introduced in the calculation, given by

$$\begin{aligned} F_{\mathrm{R}} = & \frac{\gamma}{4\sqrt{2}} \left(\frac{\mathrm{ber}_0(\gamma)\mathrm{bei}_1(\gamma) - \mathrm{ber}_0(\gamma)\mathrm{ber}_1(\gamma)}{\mathrm{ber}_1(\gamma)^2 + \mathrm{bei}_1(\gamma)^2} \right. \\ & \left. - \frac{\mathrm{bei}_0(\gamma)\mathrm{ber}_1(\gamma) - \mathrm{bei}_0(\gamma)\mathrm{bei}_1(\gamma)}{\mathrm{ber}_1(\gamma)^2 + \mathrm{bei}_1(\gamma)^2} \right) \end{aligned} \tag{2.55}$$

where bei and ber are Kelvin functions, i.e real and imaginary parts, respectively, of Bessel functions of first kind and γ is defined as

$$\gamma = \frac{d_{\mathrm{s}}}{\delta\sqrt{2}} \tag{2.56}$$

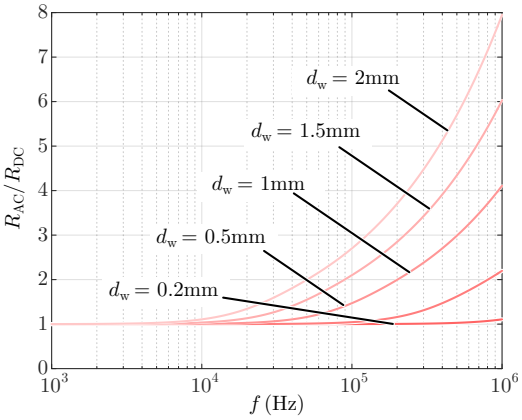

Figure 2.27: Skin effect, AC resistance vs DC resistance for different strand diameters. The calculations are done using copper wires with a conductivity σ of 5.688e7.

where d_s is the diameter of the strand. So, the DC resistance per meter is given by

$$R_{DC} = \frac{1}{n_s \pi \sigma r_s^2} \tag{2.57}$$

where r_s and n_s are the radius and the number of strands respectively. Then, the AC losses per meter considering skin effect for a bunch of strands will be

$$P_{skin} = \underbrace{R_{DC} F_R(\gamma)}_{R_{AC,eq}} \hat{I}^2 \tag{2.58}$$

Figure 2.27, represents the resistance factor for different strand diameters. It can be seen that F_R increases faster for larger strand diameters. Thus, depending on the frequency a smaller strand diameter is necessary. For example, at 100kHz, d_w should be smaller than 0.2mm.

Internal proximity effect

Basically the same procedure is followed for the internal proximity effect. A resistance factor G_R is calculated that relates the AC and DC resistances. Internal proximity effects are determined considering the field that is generated by the strands of the bundle at each position.

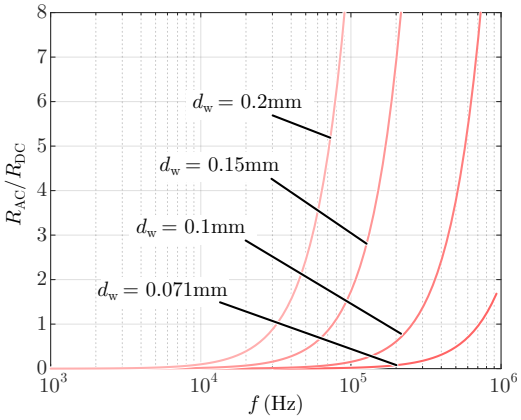

Figure 2.28: Proximity effect, AC resistance vs DC resistance for a Litz wire of 840 strands and an output diameter of 2.25mm.

This external field is applied to each of the strands. In [Villar, 2010] it is shown that the factor derived by [Ferreira, 1992] has a good accuracy for low penetration ratios. This resistance factor is given by

$$G_R = -\frac{\pi^2 d_s^2 \gamma}{2\sqrt{2}} \left(\frac{\mathrm{ber}_2(\gamma)\mathrm{ber}_1(\gamma) + \mathrm{ber}_2(\gamma)\mathrm{bei}_1(\gamma)}{\mathrm{ber}_0(\gamma)^2 + \mathrm{bei}_0(\gamma)^2} + \frac{\mathrm{bei}_2(\gamma)\mathrm{bei}_1(\gamma) - \mathrm{bei}_2(\gamma)\mathrm{ber}_1(\gamma)}{\mathrm{ber}_0(\gamma)^2 + \mathrm{bei}_0(\gamma)^2} \right) \tag{2.59}$$

and taking into account the packing factor $p_f = n_s \left(r_s/r_b\right)^2$ the internal proximity losses per meter are given by

$$P_{int} = p_f R_{DC} G_R \frac{\hat{I}^2}{8\pi^2 r_b^2} \tag{2.60}$$

where r_b denotes the wire bundle radius and r_s is the strand radius.

Figure 2.28, shows the resistance factor G_R for different strand diameters. It can be noticed that this parameter is much larger than F_R. It is mainly due to the large number of strands used for this particular case. The parameter G_R is larger with more strands. However, this is not completely fair, since for the same current density, with a larger strand diameter less strands will be needed. Nevertheless, it can be

noticed that there is an optimum number of strands that minimizes the losses. For the shown two cases, having $d_w = 0.071$mm will lead to an equivalent AC resistance close to the DC one, i.e $R_{AC} \approx R_{DC}$.

External proximity effect

Due to the neighboring turns and the field generated by them, the current distribution of the conductor changes, creating additional losses. According to [Villar, 2010], these losses are given by

$$P_{ext} = p_f R_{DC} G_R \hat{H}_{ext}^2 \tag{2.61}$$

The same term G_R applies for the internal and external proximity effects. In the end, the effect is the same, only the cause is different. However, the external magnetic field depends on the geometry and location of the turns.

It can be observed that the losses exclusively depend on the selected wire. If the strands are small enough, skin effects are negligible and thanks to the twisting of the litz wire, the proximity effects are also minimized. In this thesis, in order to select the litz wire the aforementioned calculations are going to be carried out. The wire that minimizes AC losses is going to be selected. Thereafter, during the optimization process, calculating the length of the coil and considering the DC resistance, the losses in the coil are going to be computed.

Core losses

As previously said, in IPT systems the coupling is considerably lower than in transformers. As shown in (2.4) the inductance depends on the permeability of the media where the field is created. In transformers the relative permeability is very high >1000, whereas the air has a relative permeability of 1. In order to improve as much as possible the coupling, ferrite cores are placed in the back part of the coils [Covic and Boys, 2013,Bosshard and Kolar, 2016b]. This way, the stray field is reoriented and part of it is linked by the opposing coil.

Apart from that, using ferrites has another advantage. As the magnetic field tend to go through the cores and not through the air, a shielding effect is produced. Therefore, the electronics can be safely placed in the back part of the coil

However, it does not come for free. The magnetic field circulating through the material creates losses. In 1892, Steinmetz [Steinmetz,

1892] introduced an expression based on the analysis of various loss curves

$$P_s = \eta B_m^b \tag{2.62}$$

where η and b are determined by the material, and B_m is the peak induction value in a bidirectional magnetization case. According to [Villar, 2010], nowadays a more general expression is used

$$P_s = K f^a B_m^b. \tag{2.63}$$

where K and a are determined by the material characteristic, and f is the frequency. For example, the parameters of the ferrite material 3C90 are $K = 3.8199$, $a = 1.272$ and $b = 1.354$. This expression is only valid for sinusoidal waveform. IPT perfectly fulfills this circumstance, thus more complex developments like the ones presented in [Villar, 2010] will not give any significant accuracy improvement.

Apart from the losses, the weight is also another persuading factor. Cores are a very heavy and expensive component. For that reason, typically, the entire coil is not covered by ferrites, and small pieces are used.

Shielding losses

In order to still reduce the magnetic field in the backside of the receiver coil, a typical solution is to add shielding that will absorb the field. This way eddy currents are generated in the shielding and not in the electronic components. Different options can be found in the literature such as aluminum foils or copper foils [Tejeda et al., 2017].

As described in [Bosshard, 2015], the losses due to the eddy currents can be estimated with

$$P_{sh} \approx I_{eddy}^2 R_{eddy} \propto \sqrt{\frac{f_0}{\sigma_{sh}}} \tag{2.64}$$

where σ_{sh} is the conductivity of the shielding material.

Resonant capacitor losses

In an ideal case, lossless capacitors are considered. However, this is far from being true. In order to model those losses, apart from the capacitance, a series resistance is modeled. This resistance is known as Equivalent Series Resistance (ESR) and the manufacturers give the

value of it with the loss tangent (tanδ). This parameter relates the stored energy with losses. So, in order to calculate the value of the ESR, the following equation is applied

$$\text{ESR} = \tan\delta \frac{1}{2\pi f C}. \tag{2.65}$$

Thus, the losses in the capacitors will be

$$P_C = ESR \cdot i_C^2. \tag{2.66}$$

2.5.2 Semiconductor losses

Even though in subsection 2.4.4 already a first approach has been presented regarding the converter losses, in the following part a more thorough calculation is going to be carried out. As for the inductive link, the losses in the converter can be divided into two groups: losses in the transistors and in the diodes. Since a high frequency and power is expected, SiC MOSFETs are going to be used during this thesis. Mainly, due to their improved blocking voltage compared to Si MOSFETs, and their better switching characteristics compared to Si IGBTs. Likewise, SiC diodes are going to be used, as the reverse recovery is much better than their Si counterparts. Inside each device, the losses are divided in two groups: conduction losses and switching losses.

In order to compare the performance of SiC vs. Si in the following two devices of equal voltage (1200V) and similar current characteristics are analyzed. The first one is a 1200V-138A SiC MOSFET from CREE. The second one, is a 1200V-100A IGBT from INFINEON.

Conduction losses

As detailed in [Garcia Bediaga, 2014], IGBTs and diodes, being bipolar components have a exponential forward characteristic. In contrast, MOSFETs, as they are unipolar structures, exhibit an almost linear conductive behavior. This data is given by the manufacturers for different gate voltages and junction temperatures. Figure 2.29, represents such information for the semiconductors listed in Table 2.2. So, the conduction losses for the MOSFETs are given by

$$P_{\text{MOSFET,cond}} = V_{\text{DS,RMS}} \cdot i_{\text{D,RMS}} = R_{\text{DS}} \cdot i_{\text{D,RMS}}^2. \tag{2.67}$$

Name	CAS120M12BM2	FF100R12RT4
Type	SiC MOSFET	S Si IGBT
V_{blk}	1200V	1200V
i_{D}†	138A	100A
V_{DS}*	2.7V	2.1V
V_{F}*	1.9V	1.65V
E_{ON} ⋆	3.1mJ	14mJ
E_{OFF}⋆	0.8mJ	11.9mJ
E_{REC}⋆	-	7mJ
Q_{G}‡	375nC	800nC
$R_{\text{Tth,j-c}}$	0.135°C/W	0.27°C/W
$R_{\text{Dth,j-c}}$	0.115°C/W	0.48°C/W
Price ◇	290€/u	48.18€/u

† for ambient temperature $T_{\text{amb}} = 90°\text{C}$.
* for $i_{\text{D}} = 120\text{A}$ current, $V_{\text{GS}} = 20\text{V}$ gate voltage and $T_{\text{amb}} = 150°\text{C}$.
⋆ for $i_{\text{D}} = 120\text{A}$ and $V_{\text{DS}} = 800\text{V}$.
‡ for $V_{\text{GS}} = 20\text{V}$.
◇ obtained from Mouser, on 10/10/2017. http://www.mouser.es/

Table 2.2: 1200V-120A semiconductors. SiC MOSFET shows a much better switching characteristics than Si IGBT, but the price is six times higher.

Thus, the equivalent conduction resitance R_{DS} for CAS120M12BM2s is $V_{\text{DS}}/i_{\text{D}} = 25\text{m}\Omega$.

Regarding the freewheeling diodes and the receiver side diode rectifier. Being bipolar semiconductors, the losses are

$$P_{\text{Diode,cond}} = V_0 \cdot i_{\text{D,AVG}} + R_{\text{D}} \cdot i_{\text{D,RMS}} \tag{2.68}$$

In Figure 2.30, the diode conduction characteristic of the semiconductors on Table 2.2 are represented. It can be seen that the best performance is achieved using the IGBT. Nevertheless, in IPT systems the time that the diode is conducting is minimum. Thus, its RMS current will be very low compared. So, the main benefit of the freewheeling diode of the IGBT module will, in practice, not be used.

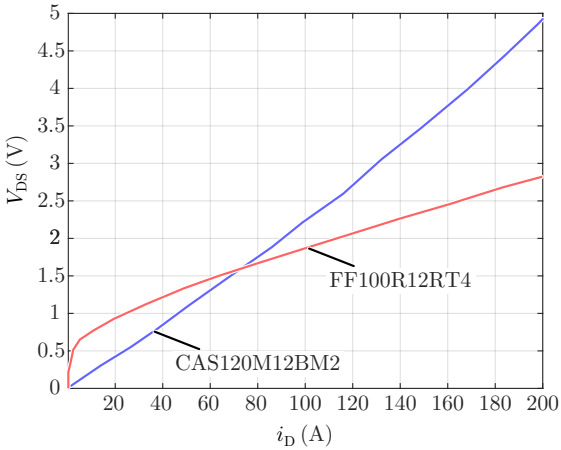

Figure 2.29: Conduction losses of the semiconductors on Table 2.2. This V_{DS}-i_D graph is obtained for $V_{GS} = 20$V and $T_j = 150°$C.

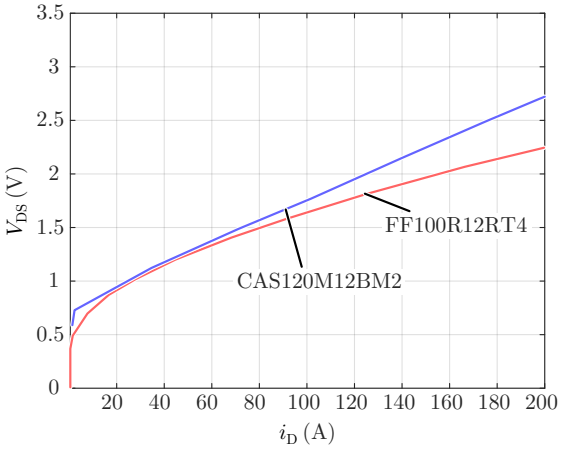

Figure 2.30: Freewheeling diodes conduction characteristic, for $T_j = 150°$C.

Switching losses

Switching losses are also estimated from the graphs provided by the semiconductor manufacturers. Figure 2.31(a) and Figure 2.31(b), rep-

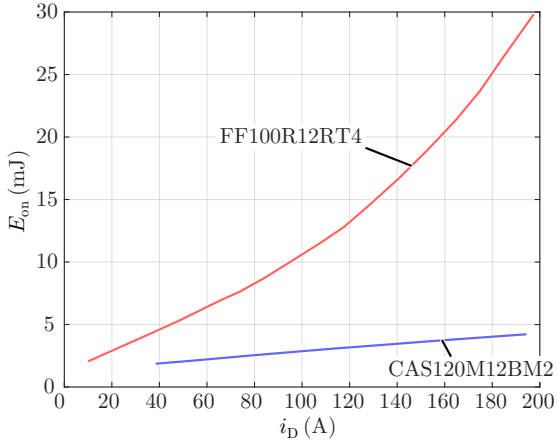

(a)

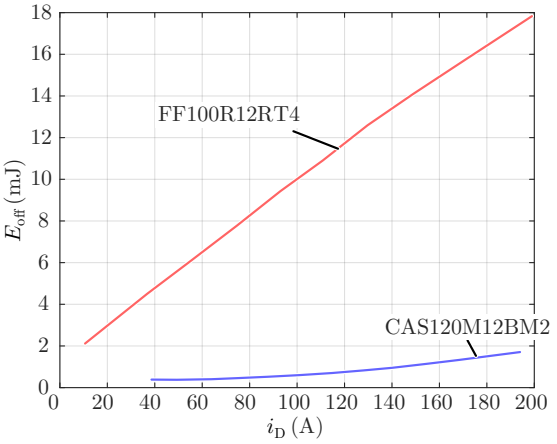

(b)

Figure 2.31: Energy dissipated during switching. It depends on the current circulating and the temperature.(a) turn ON energy dissipation. (b) turn OFF energy dissipation

resent the turn-on and turn-off losses respectively. Here, the main advantage of having unipolar semiconductor becomes latent. The losses during the turn-on of the IGBT are almost five times bigger than for the MOSFET. In addition, during the turn-off the difference is even higher, being 10 times higher for the IGBT.

However, as previously explained, in IPT applications the system works close to resonance, thus the switching is done with very little current. As it can be observed in the graphs, the data for low currents is not given. According to [Garcia Bediaga, 2014], power-electronic designers use different processes to calculate the switching losses from the available information. Four of these methods are:

1. Using the data of the graph, and considering a linear behavior between the zero-current losses and the first point graph.

2. Using the data of the graph, and considering the low current losses equal to the smallest available point.

3. Using interpolated functions, obtaining the parameters from a curve-fitting.

4. Analytical calculation from idealized waveforms.

In [Garcia Bediaga, 2014], these four methods are compared with experimental data. The conclusion is that method 1 is the closest to the real behavior. For these reason in this thesis, method 1 is going to be used. Therefore, the losses will be determined by

$$P_{\mathrm{sw,ON}} = E_{\mathrm{sw,ON}}(i_{\mathrm{D,ON}})f_{\mathrm{sw}} \tag{2.69a}$$

$$P_{\mathrm{sw,OFF}} = E_{\mathrm{sw,OFF}}(i_{\mathrm{D,OFF}})f_{\mathrm{sw}} \tag{2.69b}$$

$$P_{\mathrm{sw}} = P_{\mathrm{sw,ON}} + P_{\mathrm{sw,OFF}} \tag{2.69c}$$

Finally, as SiC diodes do not have recovery charges they do not have switching losses. Thus, no further analysis will be carried out in this matter.

2.6 Conclusions

In this chapter, the basics of inductive power transfer systems have been explained. First, starting from a classical transformer, due to

its similarities, a smooth transition has been carried out towards IPT, being the nexus the isolated conductive chargers. The waveforms and equations of the single active bridge SAB that supplies the system have been shown. Concluding that, due to the large air gap, inductance compensation topologies are required.

Then, the Series-Series and Series-Parallel compensations have been analyzed, making emphasis in the bifurcation problem and the efficiency reduction that causes. Following, the conditions to achieve zero voltage switching with resonant circuit has been analyzed. Finally, the losses of the various components, such as the wires (skin and proximity losses), cores and inverter (conduction and switching) have been obtained.

All the analysis carried out in this chapter will be used during the optimization process of Chapter 4.

Chapter 3

Three-phase IPT systems

Once the basics of single phase IPT systems have been presented, this chapter analyzes the Three Phase Dynamic IPT using meander coils. The work of this chapter is an extended version of the article published in [Iruretagoyena et al., 2017c].

The roots of meander type coils can be found in sensing applications [Wakiwaka et al., 1996a, Wakiwaka et al., 1996b]. Here, using a single coil solution, due to the sinusoidal output voltage, the position of the receiver was accurately estimated. Afterwards, [Sato et al., 1996, Sato et al., 1998, Sato et al., 1999] realized that the same effect could be used for transferring power. In this initial solution, each part was turned on and off depending on the position of the receiver. Then, [Gao, 2007] realized that creating a traveling magnetic field will improve the system, as the system will constantly turned on, without needing communication. Finally, [Meins and Struve, 2013, Meins and Vollenwyder, 2013, Vollenwyder et al., 2014], created the final solution, consisting of a three phase intertwined coil. However, despite this previous work, there is a lack of analysis and no design criterion regarding meander coils can be found in the literature.

In this chapter, first, the working principles of meander coils are going to be presented. Focusing, on the magnetic field generation. Then, the effect of different parameters, such as, coil window and distance are going to be analyzed. Afterwards, the single phase equivalent circuit

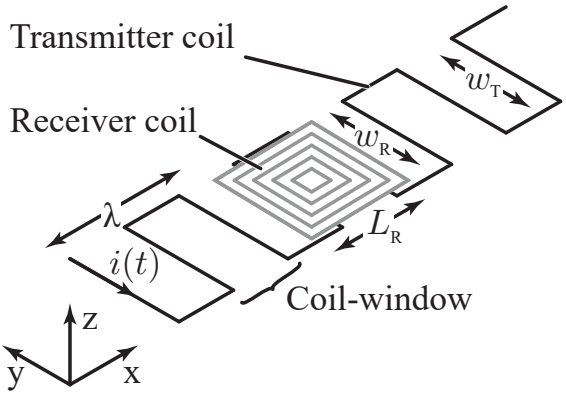

Figure 3.1: Single phase meander coil. λ is the coil window distance. w_T and w_R are the with of the transmitter and receiver coil respectively. L_R is the length of the receiver.

will be obtained, that will enable the use of the equations presented in Chapter 2. Following, the equations of three phase SAB will be obtained. Finally, the series-series and series-parallel compensations will be analyzed for the three phase case.

3.1 Meander coil fundamentals

In Figure 3.1 a drawing of a single phase meander transmitter coil with a square receiver is illustrated. As it will be shown later, this shape maximizes the coupling when the space is constrained.

In order to understand the working principles of meander coils, for the calculation of the magnetic field, a cut-plane in the x-z plane is going to be considered. Thus, the current will be circulating either entering or getting out of this plane, i.e. in the y axis. Consequently, the magnetic field can be calculated by solving Ampère's law, that is given by the curl [1]of

[1]Definition of curl is $\nabla \mathrm{x}\hat{B} = \begin{bmatrix} \hat{\mathrm{x}} & \hat{\mathrm{y}} & \hat{\mathrm{z}} \\ \frac{\partial}{\partial \mathrm{x}} & \frac{\partial}{\partial \mathrm{y}} & \frac{\partial}{\partial \mathrm{z}} \\ \vec{B}_{\mathrm{x}} & \vec{B}_{\mathrm{y}} & \vec{B}_{z} \end{bmatrix}$

$$\nabla \mathrm{x} \left(\frac{\mu_\mathrm{r} \mu_0 \hat{I}}{2\pi \sqrt{(x - x_0)^2 + (z - z_0)^2}} \hat{y} \right). \tag{3.1}$$

The magnetic field will have two components. The field in x direction B_x and the field in z direction B_z, which are

$$B_\mathrm{x} = \pm \frac{\mu_\mathrm{R} \mu_0 \hat{I}}{2\pi} \frac{\mathrm{z} - \mathrm{z}_0}{\sqrt[3/2]{(\mathrm{x} - \mathrm{x}_0)^2 + (\mathrm{z} - \mathrm{z}_0)^2}} \tag{3.2a}$$

$$B_\mathrm{z} = \pm \frac{\mu_\mathrm{R} \mu_0 \hat{I}}{2\pi} \frac{\mathrm{x} - \mathrm{x}_0}{\sqrt[3/2]{(\mathrm{x} - \mathrm{x}_0)^2 + (\mathrm{z} - \mathrm{z}_0)^2}} \tag{3.2b}$$

where x_0 and y_0 are the position of each wire, and x and y are the point where the field is calculated. Depending on the direction of the current the sign will be positive or negative.

These components are calculated for each of the wires and then summed up. Since only the perpendicular field respect to the coil turn area induces voltage, for this particular case, as the receiver is placed in the x-y plane, only the B_z component will be used.

(3.2) explains why the square coil is the optimal solution. As the mutual inductance depends on the linked field, the bigger the receiver area the higher the coupling (as long as the field is in the same direction). In a vehicle the space is limited. So the shape that maximizes the are is inevitably square. This same conclusion is derived and verified by FEM simulation in [Gonzalez-Hernando et al., 2017].

Figure 3.2 depicts the magnetic field B_z for different coil windows. Some interesting conclusions can be obtained. First of all, as expected, the closer the wires the field gets higher. But once the distance is increased, for any given λ, the peak field value is achieved exactly in the middle between two wires, i.e at $\lambda/4$ or $3\lambda/4$. Furthermore, exactly above any wire, the field B_z is zero. At this point the field vector is fully oriented in the x axis. Finally, it can be also observed that the field with the highest λ reaches further in z. However, the lines are more separated between each other. For example if z = 60mm and λ = 200mm at x = 50mm, the second line is reached, but with λ = 400mm and at x 100mm not. Besides, with z = 90mm and x at those same positions, the highest value is achieved with the highest coil-window. This entails that for each z separation an optimum λ exists, similarly to the coil sizes for static systems as presented in [Gonzalez-Hernando et al., 2017].

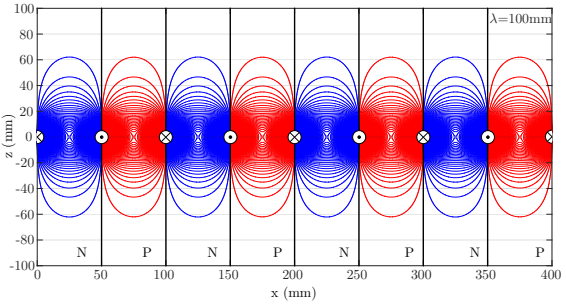

(a)

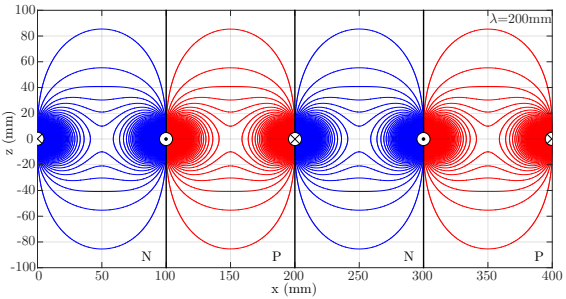

(b)

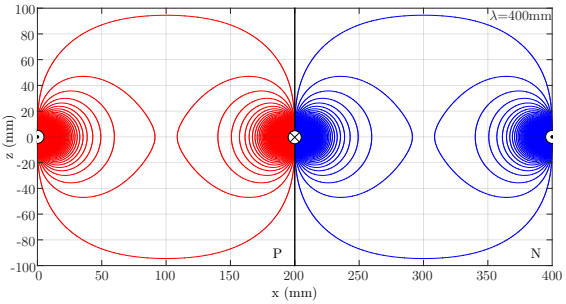

(c)

Figure 3.2: Magnitude of the magnetic field in the z direction B_z for different coil-windows. (a) $\lambda = 100$mm (b) $\lambda = 200$mm and (c) $\lambda = 400$mm. The red color or P zone represents the field in the positive direction of z. The blue color or N zone represents the field in the negative direction of z.

Nevertheless, the amplitude of the magnetic field is only one of the characteristics of meander coils. As it will be shown in the following subsection, the shape along x (moving direction) of this field is also important.

During this thesis only a square receiver is analyzed. Different solutions are also possible. For example, also a meander coil can be placed at the receiver side. However, the coupling values that are achieved are much lower (approximately 10 times lower). Therefore, the coils would have to be closer in order to be able to transmit energy without increasing too much the current.

3.1.1 Mutual inductance calculation

As just said, for the induced voltage only the z component accounts. In order to calculate the value of the mutual inductance, all the field that goes though the area A of the coil has to be integrated, i.e.

$$M = \int_A \frac{\hat{B}_\mathrm{z}}{\hat{I}} \partial A \tag{3.3}$$

Depending on the coil-window λ, the size of the receiver (L_R and w_R) and its position in x, this value will vary. For the upcoming figures the value of B_z has been obtained using FEM software FLUX® and the sum of all B_z has been carried out with MATLAB®. This way all the dimensions of the coils are taken into account.

In Figure 3.3 the coil-window is varied for a z = 25mm separation. It can be observed that if $L_\mathrm{R} < 2\lambda$, the mutual inductance has no longer a sinusoidal shape. This is due to the fact that the wires are too separated from each other and the field in the middle is weakened, as it can be deduced from Figure 3.2. Besides, if $L_\mathrm{R} > 2\lambda$, the coil encloses field that is going in the opposite direction. For this reason, even though the shape is still sinusoidal, the amplitude is reduced. The optimal coil size is when $\lambda = 2L_\mathrm{R}$ (same direction of B_z is enclosed). This way the sinusoidal shape is kept and all the magnetic field is fully exploited. Then, the mutual inductance can be represented by

$$M(\mathrm{z}, \lambda, \mathrm{x}) = \hat{M}(\mathrm{z}, \lambda)\cos\left(\frac{2\pi}{\lambda}\mathrm{x}\right) \tag{3.4}$$

where $\hat{M}(\mathrm{z}, \lambda)$ is the maximum value that must be calculated by FEM and x is the position of the receiver.

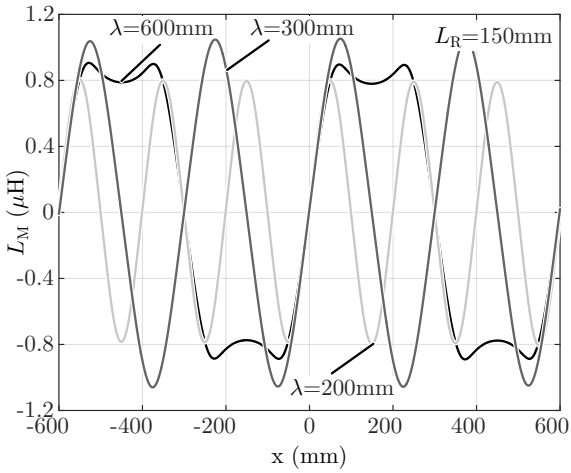

Figure 3.3: Mutual inductance for different coil-windows λ. The mutual inductance is no longer sinusoidal if $\lambda > 2L_R$. The maximum is achieved when $\lambda = 2L_R$.

Resuming, the best solution is to have the highest possible coil-window λ (the field reaches further) and the receiver coil length L_R equal to $\lambda/2$ (enclosing most of the field). The limit will be given by the space available beneath the moving vehicle. Thus the coil-window must be adapted to the given space.

However, the fact that the mutual inductance is zero is still there. This means that even though there is a current in the transmitter coil there will not be transferred power. In order to solve this issue, extra phases should be added to the transmitter side.

3.1.2 Meander coil construction

In order to further increase the mutual inductance, extra turns can be added to each winding. Note that in either self or mutual inductance the increment is quadratic to the number of turns.

Figure 3.4 illustrates the construction of a meander type coil. First of all the 'go-winding' is constructed, with the selected width and coil period, see Figure 3.4(a). Once the desired distance is covered, the 'return-winding' is constructed, see Figure 3.4(b), filling the spaces

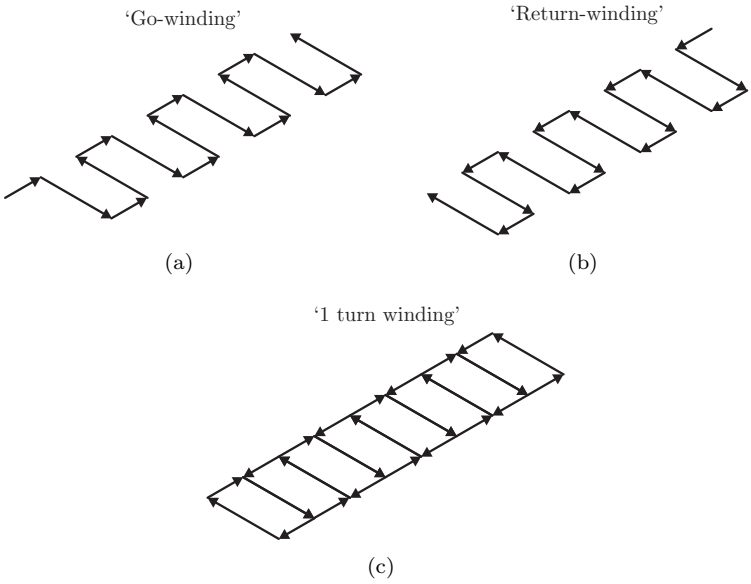

Figure 3.4: Induced voltage depending on time and position of the coil for different number of phases. (a) single phase (b) two phases (c) three phases (d) four phases.

leaved. In this thesis this 'go-back' winding is considered as a single turn winding, see Figure 3.4(c). As the start and end point of this winding configuration is at the same place, for the construction of multiple turns this procedure can be repeated.

3.1.3 Multi-phase meander coil

In any multi-phase system one of the most important characteristics is a balanced system. Otherwise, some parts of the system will suffer more and will reduce the lifetime of the device. So, in order to add new phases to the meander coil, the location of each phase can not be arbitrary. Depending on the number of phases, taking as reference the first phase, the distance between each of them has to be

$$\varphi_{\mathrm{n}} = \frac{(\mathrm{n}-1)\,\lambda}{\mathrm{N}}, \tag{3.5}$$

where N stands for the total number of phases and n is each of the phases. However, it is clear that if all the coils are supplied by the same current, the total mutual inductance will be zero for any position. Thus, to still transfer power and have a balanced system, the desired current phase shift is

$$\phi_{\mathrm{n}} = \frac{(\mathrm{n}-1)\,\mathrm{T}}{\mathrm{N}} \text{ or } \frac{(\mathrm{n}-1)}{f\mathrm{N}}. \tag{3.6}$$

Finally, the voltages that will be induced at a receiver will be the sum of the voltage generated by each transmitter. So adding (3.5) and (3.6) to the calculation, it leads to

$$v = \sum_{\mathrm{n}=1}^{N} \hat{M}\cos\left(\frac{2\pi}{\lambda}\mathrm{x} + \frac{(\mathrm{n}-1)2\pi}{\mathrm{N}}\right)\hat{i}\cdot\cos\left(\frac{2\pi}{\mathrm{T}}\mathrm{t} + \frac{(\mathrm{n}-1)2\pi}{\mathrm{N}}\right). \tag{3.7}$$

Figure 3.5 represents the induced voltage (p.u.) for different number of phases[2]. The most interesting aspect is that if $\mathrm{N} \geqq 3$ the induced voltage becomes a traveling wave. It will have two periods, a geometric given by λ and a time period T. It must be kept in mind that the speed of the receiver is much smaller than the operating frequency. So the variation in x is negligible from the electric point of view. Thus during the design phase of the power electronics x will be considered constant. Consequently, it can be concluded that for any given position, the power transmission will be also constant. Furthermore, the magnitude of this constant mutual inductance will be dependent on the number of phases. In Figure 3.5(c) the magnitude is 1.5 times bigger than for $\mathrm{N} = 1$, whereas in Figure 3.5(d) is 2 times bigger. So the relation between the single phase and a system with 3 or more phases will be given by

$$\hat{M}_{\mathrm{N}} = \frac{\mathrm{N}}{2}\hat{M}_1 \text{ for } \mathrm{N} > 2. \tag{3.8}$$

This relation simplifies the analysis and design of a multi-phase IPT system. Its equivalent single phase circuit can be used to calculate all the parameters previously presented in Chapter 2.

[2] In the drawing $\lambda = \mathrm{T}$ for better visualization.

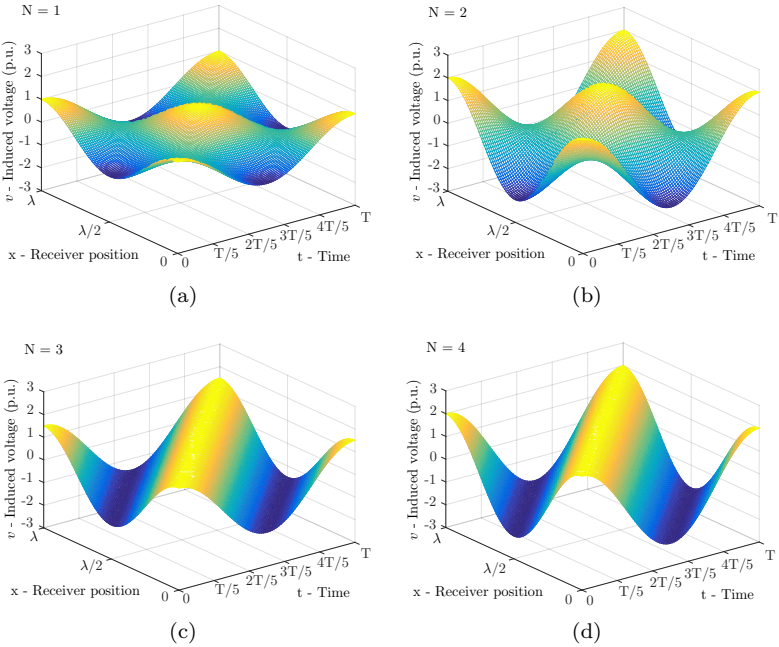

Figure 3.5: Induced voltage depending on time and position of the coil for different number of phases. (a) single phase (b) two phases (c) three phases (d) four phases.

3.2 Three-phase system development

In the previous section it has been demonstrated that with a meander coil with more than two phases constant mutual inductance can be achieved. However, adding more and more phases makes the system complex and most important expensive. As explained in Chapter 1, in industry the cost is the predominant constraint. For this reason, in the following section only the three phase system is going to be analyzed.

3.2.1 Three phase IPT

As for the single phase system presented in Section 2.3, the three phase IPT system can be represented by a voltage equivalent circuit. In this case, instead of having just a single voltage source describing the cou-

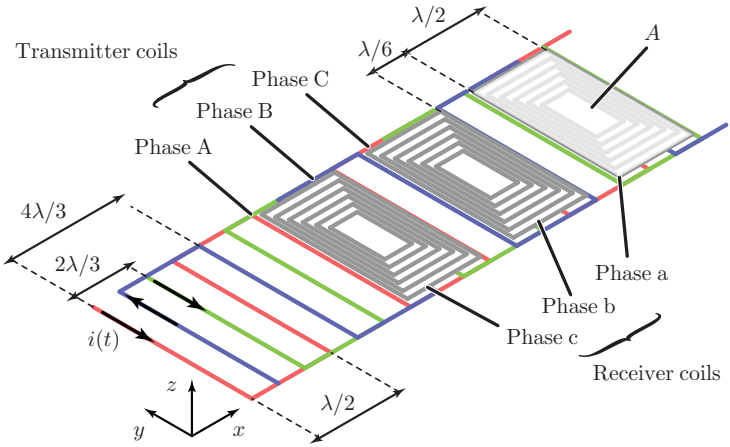

Figure 3.6: Three phase IPT coils with three meander transmitter coils and three square receiver coils.

pling, all the coil combinations must be represented. At this point, it can be noticed that in order to have a balanced system, if there are three transmitters, also three receivers must be added. Otherwise, the voltage reflected at each transmitter phase will be equal and since the voltages are shifted, all three currents can not be in phase at the same time. Thus, following the same reasoning as for the transmitter phases, it can be certainly said that the separation between the receivers should be also of 120° per phase.

Having so many coil combinations, instead of an equation form, the three phase system is better represented with a matrix form. So defining ABC as the transmitter phases and abc as receiver phases, this matrix is given by

$$\begin{bmatrix} \vec{v}_{\mathrm{L,A}} \\ \vec{v}_{\mathrm{L,B}} \\ \vec{v}_{\mathrm{L,C}} \\ \vec{v}_{\mathrm{L,a}} \\ \vec{v}_{\mathrm{L,b}} \\ \vec{v}_{\mathrm{L,c}} \end{bmatrix} = \left[\begin{array}{ccc|ccc} \overbrace{L_{\mathrm{A,A}} & M_{\mathrm{B,A}} & M_{\mathrm{C,A}}}^{\text{Transmitter inductance}} & \overbrace{M_{\mathrm{a,A}} & M_{\mathrm{b,A}} & M_{\mathrm{c,A}}}^{\text{Mutual inductance}} \\ M_{\mathrm{A,B}} & L_{\mathrm{B,B}} & M_{\mathrm{C,B}} & M_{\mathrm{a,B}} & M_{\mathrm{b,B}} & M_{\mathrm{c,B}} \\ M_{\mathrm{A,C}} & M_{\mathrm{B,C}} & L_{\mathrm{C,C}} & M_{\mathrm{a,C}} & M_{\mathrm{b,C}} & M_{\mathrm{c,C}} \\ \hline M_{\mathrm{A,a}} & M_{\mathrm{B,a}} & M_{\mathrm{C,a}} & L_{\mathrm{a,a}} & M_{\mathrm{b,a}} & M_{\mathrm{c,a}} \\ M_{\mathrm{A,b}} & M_{\mathrm{B,b}} & M_{\mathrm{C,b}} & M_{\mathrm{a,b}} & L_{\mathrm{b,b}} & M_{\mathrm{c,b}} \\ \underbrace{M_{\mathrm{A,c}} & M_{\mathrm{B,c}} & M_{\mathrm{C,c}}}_{\text{Mutual inductance}^{\mathrm{T}}} & \underbrace{M_{\mathrm{a,c}} & M_{\mathrm{b,c}} & L_{\mathrm{c,c}}}_{\text{Receiver inductance}} \end{array}\right] \begin{bmatrix} \vec{i}_{\mathrm{L,A}} \\ \vec{i}_{\mathrm{L,B}} \\ \vec{i}_{\mathrm{L,C}} \\ \vec{i}_{\mathrm{L,a}} \\ \vec{i}_{\mathrm{L,b}} \\ \vec{i}_{\mathrm{L,c}} \end{bmatrix} \tag{3.9}$$

where $\vec{v}_{\mathrm{L,x}}$ denotes the voltage seen at the coil terminals, $\vec{i}_{\mathrm{L,x}}$ is the current into the coil and $M_{\mathrm{x,y}}$ is the coupling between coil x and y[3]. Inside the matrix, four different matrices can be defined. In the left-upper part, the transmitter inductance matrix, represents the self inductances of each phase $L_{\mathrm{A,A}}$, $L_{\mathrm{B,B}}$ and $L_{\mathrm{C,C}}$ and the mutual inductances $M_{\mathrm{ABC,ABC}}$ due to the interaction between them. A similar matrix can be found in the bottom-right part, the receiver self inductance. It represent the self inductances $L_{\mathrm{a,a}}$, $L_{\mathrm{b,b}}$ and $L_{\mathrm{c,c}}$ and the mutual inductances $M_{\mathrm{abc,abc}}$ of the receiver part. These mutual inductances produced by the interaction between phases do not generate a useful power transmission. As it will be shown later, these terms can be neglected during the calculations of the power transmission. However, they have to be taken into account during the calculation of the resonant capacitances. This way, these useless inductances will not affect to the inverter operation. Fortunately, since the position among them is always equal, their value will be constant. Finally, in the upper-right part and bottom-left part, the mutual inductance and its transpose can be found, representing all the combinations between transmitter and receiver coils. This inductances are the ones that actually transmit useful power.

In order to have identical load at each phase, not only the self inductances have to be equal $L_{\mathrm{A,A}} = L_{\mathrm{B,B}} = L_{\mathrm{C,C}}$ and $L_{\mathrm{a,a}} = L_{\mathrm{b,b}} = L_{\mathrm{c,c}}$; but also the coupling inductances between them has to be balanced, i.e $M_{\mathrm{A,a}} = M_{\mathrm{B,b}} = M_{\mathrm{C,c}}$, $M_{\mathrm{A,b}} = M_{\mathrm{B,c}} = M_{\mathrm{C,a}}$ and $M_{\mathrm{A,c}} = M_{\mathrm{B,a}} = M_{\mathrm{C,b}}$, where from equation 3.4 and 3.5 it is known that,

$$M_{\mathrm{A,a}} = \hat{M}\cos\left(\frac{2\pi}{\lambda}\mathrm{x}\right), \tag{3.10a}$$

[3]Reminder that $M_{\mathrm{x,y}} = M_{\mathrm{y,x}}$

$$M_{\mathrm{A,b}} = \hat{M}\cos\left(\frac{2\pi}{\lambda}\mathrm{x} + \frac{2\pi}{3}\right), \tag{3.10b}$$

$$M_{\mathrm{A,c}} = \hat{M}\cos\left(\frac{2\pi}{\lambda}\mathrm{x} - \frac{2\pi}{3}\right). \tag{3.10c}$$

3.2.2 Coil connection

Depending on the connection type, the current $\vec{i}_{\mathrm{L,x}}$ and the voltages $\vec{v}_{\mathrm{L,x}}$ seen at the coil terminals will be different. There are two standard connection types in three phase systems, which are the star or wye (Y) and triangle or delta (Δ) that can also be applied in the three phase IPT. From these connections four configurations are obtained Y-Y, Y-Δ, Δ-Y and Δ-Δ, see Figure 3.7. The relation between star and triangle connection is given by

$$L_{\mathrm{A},\Delta} = \frac{L_{\mathrm{A,Y}}L_{\mathrm{B,Y}} + L_{\mathrm{A,Y}}L_{\mathrm{C,Y}} + L_{\mathrm{B,Y}}L_{\mathrm{C,Y}}}{L_{\mathrm{A,Y}}} = 3L_{\mathrm{A,Y}} \tag{3.11a}$$

$$L_{\mathrm{a},\Delta} = \frac{L_{\mathrm{a,Y}}L_{\mathrm{b,Y}} + L_{\mathrm{a,Y}}L_{\mathrm{c,Y}} + L_{\mathrm{b,Y}}L_{\mathrm{c,Y}}}{L_{\mathrm{a,Y}}} = 3L_{\mathrm{a,Y}} \tag{3.11b}$$

So in order to have the same load, from the converter point of view, the inductance of the triangle connection should be 3 times bigger than for the star one. This entails that for the triangle-triangle connection, both coils have to be 3 times larger. And as a consequence, for the same coupling coefficient, the mutual inductance will be also 3 times bigger. For the star-triangle and triangle-star connections, since only one of the coils has to be adapted, the mutual inductance will be $\sqrt{3}$ times bigger.

3.2.3 Three phase SAB

Similarly to the single phase system presented in Chapter 2, for the three phase IPT system a SAB converter is going to be analyzed. Here instead of having just a full-bridge at the transmitted side and a diode bridge at the receiver part, an extra leg is added in each converter, see Figure 3.8. Compared to the single phase, in this case, the control parameters are reduced to the switching frequency f and the duty-cycle D, since the phase between legs ϕ has to be 120° to keep a balanced system.

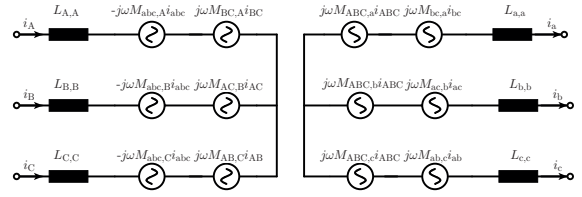

(a)

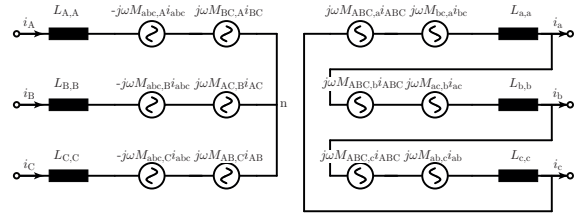

(b)

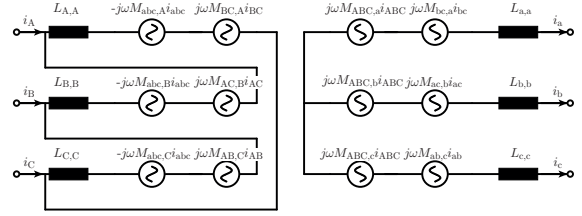

(c)

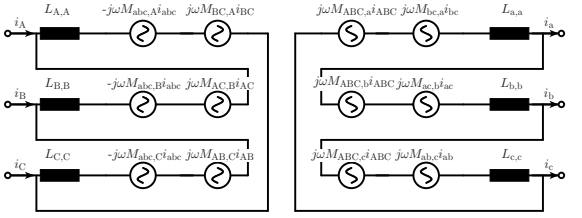

(d)

Figure 3.7: Connections for three phase systems. (a) Y-Y connection. (b) Y-Δ connection. (c) Δ-Y connection. (d) Δ-Δ connection.

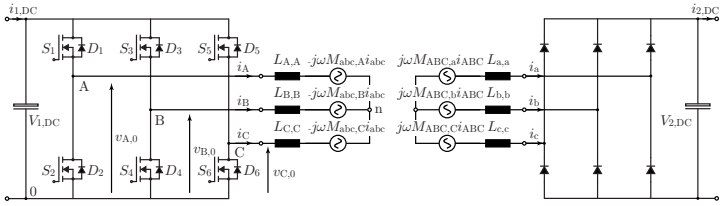

Figure 3.8: Three phase SAB with star-star connection. For simplification only the mutual inductance between transmitter and receiver coils are drawn.

In order to calculate the voltage seen by each of the transmitter coils, first the phase to zero voltage has to bee calculated. Since all the waveforms are periodical, they can be represented by the following Fourier series

$$v_{A,0} = DV_{1,DC} + \sum_{n=1}^{\infty} \frac{2V_{1,DC}}{n\pi} \sin(n\pi D) \underbrace{\cos(n\omega t)}_{A} \tag{3.12a}$$

$$v_{B,0} = DV_{1,DC} + \sum_{n=1}^{\infty} \frac{2V_{1,DC}}{n\pi} \sin(n\pi D) \underbrace{\cos\left(n\omega t + \frac{n2\pi}{3}\right)}_{B} \tag{3.12b}$$

$$v_{C,0} = DV_{1,DC} + \sum_{n=1}^{\infty} \frac{2V_{1,DC}}{n\pi} \sin(n\pi D) \underbrace{\cos\left(n\omega t - \frac{n2\pi}{3}\right)}_{C} \tag{3.12c}$$

where $v_{A,0}, v_{B,0}$ and $v_{C,0}$ are the voltages at each phase, ω is the frequency and n is the harmonic number. Depending on the connection, the voltage seen in their terminals differs, see Figure 3.9.

Δ-connection voltage

With a triangle or delta connection, the coil is directly connected to two phases. Thus, the voltage will be the subtraction between both of them, i.e.

$$v_{L,A} = v_{A,0} - v_{B,0} = \sum_{n=1}^{\infty} \frac{2V_{1,DC}}{n\pi} \sin(n\pi D)\,(A - B) \tag{3.13a}$$

$$v_{\mathrm{L,B}} = v_{\mathrm{B,0}} - v_{\mathrm{C,0}} = \sum_{\mathrm{n}=1}^{\infty} \frac{2V_{\mathrm{1,DC}}}{\mathrm{n}\pi} \sin\left(\mathrm{n}\pi D\right)\left(\mathrm{B} - \mathrm{C}\right) \tag{3.13b}$$

$$v_{\mathrm{L,C}} = v_{\mathrm{B,0}} - v_{\mathrm{A,0}} = \sum_{\mathrm{n}=1}^{\infty} \frac{2V_{\mathrm{1,DC}}}{\mathrm{n}\pi} \sin\left(\mathrm{n}\pi D\right)\left(\mathrm{C} - \mathrm{A}\right) \tag{3.13c}$$

Y-connection voltage

When the primary is connected in star configuration the coil is connected to a phase and a neutral point labeled n. Considering an ideal system the value of the voltage of this neutral point will be given by

$$v_{\mathrm{n,0}} = \frac{v_{\mathrm{A,0}} + v_{\mathrm{C,0}} + v_{\mathrm{C,0}}}{3}. \tag{3.14}$$

So, the voltage seen by each of the transmitter coils will be the subtraction between the phase voltage and the neutral to zero voltage

$$v_{\mathrm{L,A}} = v_{\mathrm{A,0}} - v_{\mathrm{n,0}} = \sum_{\mathrm{n}=1}^{\infty} \frac{2V_{\mathrm{1,DC}}}{3\mathrm{n}\pi} \sin\left(\mathrm{n}\pi D\right)\left(2\mathrm{A} - \mathrm{B} - \mathrm{C}\right) \tag{3.15a}$$

$$v_{\mathrm{L,B}} = v_{\mathrm{B,0}} - v_{\mathrm{n,0}} = \sum_{\mathrm{n}=1}^{\infty} \frac{2V_{\mathrm{1,DC}}}{3\mathrm{n}\pi} \sin\left(\mathrm{n}\pi D\right)\left(-\mathrm{A} + 2\mathrm{B} - \mathrm{C}\right) \tag{3.15b}$$

$$v_{\mathrm{L,C}} = v_{\mathrm{C,0}} - v_{\mathrm{n,0}} = \sum_{\mathrm{n}=1}^{\infty} \frac{2V_{\mathrm{1,DC}}}{3\mathrm{n}\pi} \sin\left(\mathrm{n}\pi D\right)\left(-\mathrm{A} - \mathrm{B} + 2\mathrm{C}\right) \tag{3.15c}$$

Once again, many outputs can be obtained varying D, see Figure 3.9. However, in practice, the duty cycle is fixed to 50%, Figure 3.9(c). This way all the conduction and switching losses are uniformly distributed among the semiconductors. In addition, switching losses improved since ZVS is achieved. Then, the power transmission is controlled varying either of the DC voltages.

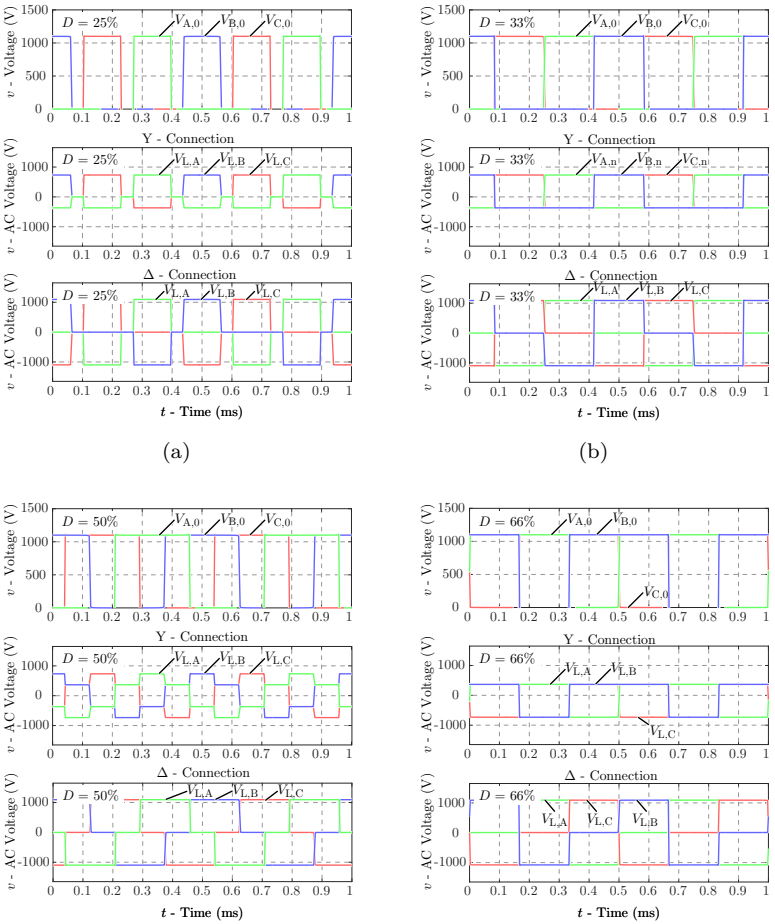

Figure 3.9: Different output voltages, varying D for star and triangle configurations. (a) $D = 25\%$, (b) $D = 33\%$, (c) $D = 50\%$, which is the square wave modulation for the three phase system and (d) $D = 66\%$. During this work only the (c) case is going to be analyzed. Being the only one that balances the current through the semiconductors.

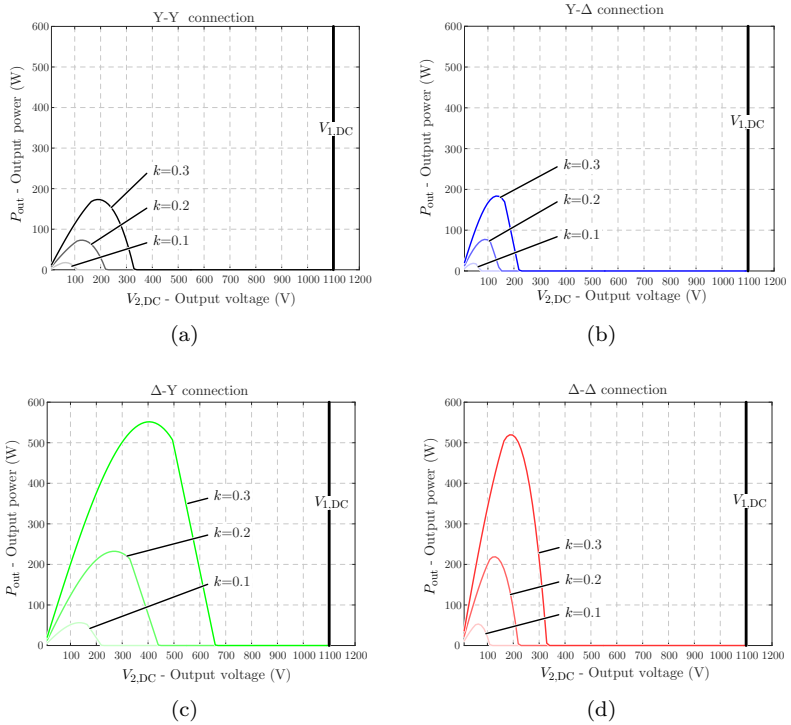

Figure 3.10: Output power for various coupling coefficient. The IPT system is analyzed with the same parameters as the ICC of section 2.3. $V_{1,DC} = 1100V$ and varying $V_{2,DC}$ for the four connection combinations: (a) Y-Y connection, (b) Y-Δ connection, (c) Δ-Y connection and (D) $\Delta-\Delta$ connection.

3.2.4 Three phase SAB output power

Figure 3.10 represents the output power for coupling coefficients 0.1, 0.2 and 0.3 for the aforementioned four connection combinations. These results are obtained for the same coil parameters used in section 2.3. It can be observed that for a Y transmitter the output power is much smaller compared to the Δ connection. The reason is that the voltage at the coil terminals is higher for the delta connection, as it can be appreciated in Figure 3.9. Since the same inductance is connected, the current circulating through the coil is also higher. Then, as the mutual

inductance is also equal, the voltage induced at the receiver side is higher for the delta connection. Finally, depending on the connection of the receiver the phase current will be different. If the secondary is connected in wye connection, the phase current will be equal to the coil current. Besides, if the receiver is connected in delta, the phase current will be $\sqrt{3}$ times smaller. For this reason, the highest output power is achieved using Δ-Y connection. Nevertheless, for the present work the coil is going to be adjusted for a certain power. Thus, even though a higher power would be transmitted with Δ-Δ connection, the smallest coil is obtained with Y-Y connection. So, from now on only this connection is going to be analyzed.

3.3 Three-phase compensation topologies

As previously analyzed for the single phase system, in order to improve the efficiency and the power transfer capability, self inductances must be compensated. This allows the simplification of the system to its fundamental frequency. The phase voltages will be

$$\begin{aligned} v_{\mathrm{L,A}} &= \frac{2V_{1,\mathrm{DC}}}{\pi}\cos(\omega t) \\ v_{\mathrm{L,B}} &= \frac{2V_{1,\mathrm{DC}}}{\pi}\cos\left(\omega t + \frac{2\pi}{3}\right) \\ v_{\mathrm{L,C}} &= \frac{2V_{1,\mathrm{DC}}}{\pi}\cos\left(\omega t - \frac{2\pi}{3}\right) \end{aligned} \tag{3.16}$$

3.3.1 Three-phase series-series compensation

Figure 3.11, depicts a three phase IPT system with series-series compensation. Following the same procedure as in section 2.4, first the secondary side AC voltage is calculated with

$$\hat{v}_{\mathrm{a}} = \frac{2}{\pi}V_{2,\mathrm{DC}}. \tag{3.17}$$

Since a three phase diode bridge is used, the relation between AC and DC current is found by solving

$$i_{2,\mathrm{DC}} = 6f\int_{\frac{1}{4f}-\frac{1}{12f}}^{\frac{1}{4f}+\frac{1}{12f}} \hat{i}_2 \sin(\omega t) = \frac{3}{\pi}\hat{i}_2. \tag{3.18}$$

Figure 3.11: Three phase SAB system with Series-Series compensation with Y-Y connection. The inverter is replaced by equivalent voltage sources. The load is replaced by an equivalent resistance.

Then, the equivalent AC resistance R_{AC} per phase is

$$R_{\mathrm{AC}} = \frac{\hat{v}_2}{\hat{i}_2} = \frac{\frac{2}{\pi}V_{2,\mathrm{DC}}}{\frac{\pi}{3}i_{2,\mathrm{DC}}} = \frac{6}{\pi^2}R_{2,\mathrm{DC}} = \frac{6}{\pi^2}\frac{V_{2,\mathrm{DC}}^2}{P_{\mathrm{out}}}. \tag{3.19}$$

This equivalent phase resistance is calculated considering that they are in Y-connection. So, assuming that there is no coupling among the transmitter phases nor among receiver phases, the three phase system can be analyzed using its single phase equivalence

$$\begin{aligned} \vec{v}_{\mathrm{A,n}} &= \overbrace{\left(\frac{1}{j\omega C_{\mathrm{A}}} + j\omega L_{\mathrm{AA}}\right)}^{Z_{\mathrm{A}}}\vec{i}_{\mathrm{A}} - j\omega\frac{3}{2}\hat{M}\vec{i}_{\mathrm{a}} \\ R_{\mathrm{AC}}\vec{i}_{\mathrm{a}} &= j\omega\frac{3}{2}\hat{M}\vec{i}_{\mathrm{A}} - \underbrace{\left(j\omega L_{\mathrm{aa}} + \frac{1}{j\omega C_{\mathrm{a}}}\right)}_{Z_{\mathrm{a}}}\vec{i}_{\mathrm{a}} \end{aligned} \tag{3.20}$$

Thus, similarly to the single phase system, in the ideal case the resonant capacitance value will be given by

$$\begin{aligned} C_{\mathrm{A}} &= \frac{1}{\omega_0^2 L_{\mathrm{A}}} \\ C_{\mathrm{a}} &= \frac{1}{\omega_0^2 L_{\mathrm{a}}} \end{aligned} \tag{3.21}$$

Nevertheless, the calculation of the resonance capacitance with 3.21 can not be used in the real system. Even though it does not affect the

power transmission equation and the calculation of the peak mutual inductance, as said in section 3.1, the coupling among transmitter and receiver coil must be also considered. In [Safaee et al., 2015], the procedure of calculating the resonant capacitance with coupled inductances is detailed. Considering all mutual couplings equal, this capacitance values is given by,

$$\begin{aligned} C_{\mathrm{A}} &= \frac{1}{\omega_0^2\left(L_{\mathrm{A,A}} - M_{\mathrm{A,B}} - M_{\mathrm{A,C}} + M_{\mathrm{B,C}}\right)} = \frac{1}{\omega_0^2 L_{\mathrm{A,A}}\left(1 - k_{\mathrm{T}}\right)}, \\ C_{\mathrm{B}} &= \frac{1}{\omega_0^2\left(L_{\mathrm{B,B}} - M_{\mathrm{B,A}} - M_{\mathrm{B,C}} + M_{\mathrm{A,C}}\right)} = \frac{1}{\omega_0^2 L_{\mathrm{B,B}}\left(1 - k_{\mathrm{T}}\right)}, \\ C_{\mathrm{C}} &= \frac{1}{\omega_0^2\left(L_{\mathrm{C,C}} - M_{\mathrm{C,A}} - M_{\mathrm{C,B}} + M_{\mathrm{A,B}}\right)} = \frac{1}{\omega_0^2 L_{\mathrm{C,C}}\left(1 - k_{\mathrm{T}}\right)}, \end{aligned} \tag{3.22}$$

and for the receiver part

$$\begin{aligned} C_{\mathrm{a}} &= \frac{1}{\omega_0^2\left(L_{\mathrm{a,a}} - M_{\mathrm{a,b}} - M_{\mathrm{a,c}} + M_{\mathrm{b,c}}\right)} = \frac{1}{\omega_0^2 L_{\mathrm{a,a}}\left(1 - k_{\mathrm{R}}\right)}, \\ C_{\mathrm{b}} &= \frac{1}{\omega_0^2\left(L_{\mathrm{b,b}} - M_{\mathrm{b,a}} - M_{\mathrm{b,c}} + M_{\mathrm{a,c}}\right)} = \frac{1}{\omega_0^2 L_{\mathrm{b,b}}\left(1 - k_{\mathrm{R}}\right)}, \\ C_{\mathrm{c}} &= \frac{1}{\omega_0^2\left(L_{\mathrm{c,c}} - M_{\mathrm{c,a}} - M_{\mathrm{c,b}} + M_{\mathrm{a,b}}\right)} = \frac{1}{\omega_0^2 L_{\mathrm{c,c}}\left(1 - k_{\mathrm{R}}\right)}. \end{aligned} \tag{3.23}$$

where k_{T} and k_{R} denote the coupling coefficient among transmitter and receiver phases respectively.

Using these capacitor values, the impedance seen by the inverter will be completely resistive, i.e. impedance angle zero. So for the power transmission calculation, using (3.21) or (3.23) is indifferent. Thus, solving 3.20, the output power is given by

$$P_{\mathrm{out}} = \frac{4}{\pi^2}\frac{V_{1,\mathrm{DC}} V_{2,\mathrm{DC}}}{\omega_0 \hat{M}} \tag{3.24}$$

It can be observed that the output power is proportional to either of the DC voltages. So, maintaining one of them constant the power can be controlled by the counterpart side. This allows, using meander type coils, since a constant coupling is produced, to control the power without any communication between the transmitter and the receiver parts once the peak value is known.

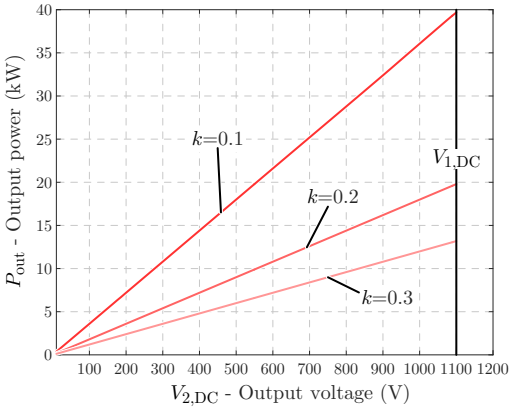

Figure 3.12: Output power with series-series compensation. Setting constant one of the DC voltages, the power transmission becomes proportional to the counterpart voltage.

From the design point of view, rearranging equation 3.24, the desired peak mutual inductance value can be calculated with

$$\hat{M} = \frac{4}{\pi^2} \frac{V_{1,\mathrm{DC}} V_{2,\mathrm{DC}}}{\omega_0 P_{\mathrm{out}}}. \tag{3.25}$$

Thus during the optimization process, the value of $\hat{M}$ is sufficient to obtain the behavior of the whole system. It must be kept in mind that the value of equation 3.25 is for a star-star configuration. If a triangle-triangle connection is used, this value has to be 3 times bigger. And if a star-triangle or a triangle-star connection is used, the peak mutual inductance has to be $\sqrt{3}$ times bigger. The output power represented in Figure 3.12 is equal for any given connection.

Lastly, considering all the phases equal and tunned with (3.23), the input impedance of the three phase IPT system is

$$Z_{\mathrm{A}} = \frac{\vec{v}_{\mathrm{A}}}{\vec{i}_{\mathrm{A}}} = \frac{\left(\omega^2 \frac{3}{2} M\right)^2 + j\omega L_{\mathrm{T}} \left(\omega^2 - \omega_0^2\right) R_{\mathrm{AC}} - L_{\mathrm{T}} L_{\mathrm{R}} \left(\omega^2 - \omega_0^2\right)^2}{\omega \left(j \left(\omega^2 - \omega_0^2\right) L_{\mathrm{R}} + \omega R_{\mathrm{AC}}\right)} \tag{3.26}$$

were

$$\begin{aligned} L_{\mathrm{T}} &= (1 - k_{\mathrm{T}})\, L_{\mathrm{AA}} \\ L_{\mathrm{R}} &= (1 - k_{\mathrm{R}})\, L_{\mathrm{aa}} \end{aligned} \tag{3.27}$$

Here the imaginary part is given by

$$\Im\left(Z_{\mathrm{A}}\right) = \frac{\left(\omega^2 - \omega_0^2\right)\left(\left(\omega^2 - \omega_0^2\right)^2 L_{\mathrm{T}} L_{\mathrm{R}}^2 + L_{\mathrm{T}} R_{\mathrm{AC}}^2 \omega^2 - \left(\omega^2 \frac{3}{2} M\right)^2 L_{\mathrm{R}}\right)}{\omega\left(\left(\omega^2 - \omega_0^2\right)^2 L_{\mathrm{R}}^2 + \omega^2 R_{\mathrm{AC}}^2\right)} = 0. \tag{3.28}$$

As for the single phase system, more than one zeros can be obtained, thus also in the three phase system the pole-splitting occurs. The limits of the coupling and output power for the three phase IPT system are

$$k_{\mathrm{lim}} = \frac{4}{\pi^2} \frac{V_{2,\mathrm{DC}}^2}{\omega_0 \left(1 - k_{\mathrm{R}}\right) L_2 P_{\mathrm{out}}} \tag{3.29a}$$

$$P_{\mathrm{out,lim}} = \frac{4}{\pi^2} \frac{V_{2,\mathrm{DC}}^2}{k \omega_0 \left(1 - k_{\mathrm{R}}\right) L_2} \tag{3.29b}$$

Finally, the limit for the inductance ratio χ is

$$\chi_{\mathrm{lim}} = \frac{1 - k_{\mathrm{T}}}{1 - k_{\mathrm{R}}} \left(\frac{V_{2,\mathrm{DC}}}{V_{1,\mathrm{DC}}}\right)^2 \tag{3.30}$$

3.3.2 Three-phase Series-Parallel compensation

For the Series-Parallel connection, see Figure 3.13, the secondary side must be controlled by a current driven source. The secondary side AC current will be given by

$$\hat{i}_2 = \frac{2}{\pi} i_{2,\mathrm{DC}}. \tag{3.31}$$

While the secondary AC voltage is defined as

$$V_{2,\mathrm{DC}} = \frac{3}{\pi} \hat{v}_2. \tag{3.32}$$

Figure 3.13: Three phase SAB system with Series-Parallel compensation with Y-Y connection. The inverter is replaced by equivalent voltage sources. The load is replaced by an equivalent resistance.

So the equivalent AC resistance will be

$$R_{\mathrm{AC}} = \frac{\pi^2}{6}\frac{P_{\mathrm{out}}}{i_{2,\mathrm{DC}}^2}. \tag{3.33}$$

Similarly to the Series-Series compensation, the single phase equivalence can be used. Thus the inductive link can be described by

$$\begin{aligned}
\vec{v_{\mathrm{A}}} &= \underbrace{\left(\frac{1}{j\omega C_{\mathrm{A}}} + j\omega L_{\mathrm{AA}}\right)}_{\mathrm{z_A}} \vec{i_{\mathrm{A}}} - j\omega\frac{3}{2}\hat{M}\vec{i_{\mathrm{a,L}}} \\
j\omega\frac{3}{2}\hat{M}\vec{i_{\mathrm{A}}} &= \underbrace{j\omega L_{\mathrm{aa}}\vec{i_{\mathrm{a,L}}} + \frac{1}{j\omega C_{\mathrm{a}}}\vec{i_{\mathrm{a,C}}}}_{Z_{\mathrm{a}}} \\
\frac{1}{j\omega C_{\mathrm{a}}}\vec{i_{\mathrm{a,C}}} &= R_{\mathrm{AC}}\vec{i_{\mathrm{a}}} \\
\vec{i_{\mathrm{a,L}}} &= \vec{i_{\mathrm{a,C}}} + \vec{i_{\mathrm{a}}}.
\end{aligned} \tag{3.34}$$

Thus, the calculation of the capacitors in ideal conditions is given by

$$C_{\mathrm{a}} = \frac{1}{\omega_0^2 L_{\mathrm{aa}}} \tag{3.35a}$$

$$C_{\mathrm{A}} = \frac{1}{\omega_0^2 L_{\mathrm{AA}}\left(1-k^2\right)}. \tag{3.35b}$$

This leads to an output power, when the system is in resonance, of

$$P_{\text{out}} = \frac{4}{\pi^2} \frac{V_{1,\text{DC}} L_2 i_{2,\text{DC}}}{\hat{M}} \tag{3.36}$$

Similarly to the series-series compensation, in a real case the value of the capacitors must be adjusted with

$$\begin{aligned} C_{\text{a}} &= \frac{1}{\omega_0^2 \left(L_{\text{a,a}} - M_{\text{a,b}} - M_{\text{a,c}} + M_{\text{b,c}}\right)}, \\ C_{\text{b}} &= \frac{1}{\omega_0^2 \left(L_{\text{b,b}} - M_{\text{b,a}} - M_{\text{b,c}} + M_{\text{a,c}}\right)}, \\ C_{\text{c}} &= \frac{1}{\omega_0^2 \left(L_{\text{c,c}} - M_{\text{c,a}} - M_{\text{c,b}} + M_{\text{a,b}}\right)}, \end{aligned} \tag{3.37}$$

and for the transmitter side

$$\begin{aligned} C_{\text{A}} &= \frac{1}{\omega_0^2 \left(L_{\text{A,A}} - M_{\text{A,B}} - M_{\text{A,C}} + M_{\text{B,C}}\right)\left(1 - k_3^2\right)}, \\ C_{\text{B}} &= \frac{1}{\omega_0^2 \left(L_{\text{B,B}} - M_{\text{B,A}} - M_{\text{B,C}} + M_{\text{A,C}}\right)\left(1 - k_3^2\right)}, \\ C_{\text{C}} &= \frac{1}{\omega_0^2 \left(L_{\text{C,C}} - M_{\text{C,A}} - M_{\text{C,B}} + M_{\text{A,B}}\right)\left(1 - k_3^2\right)}. \end{aligned} \tag{3.38}$$

$$Z_{\text{A}} = L_{\text{T}} \frac{(\omega - \omega_0)^2 (k_3^2 - 1) \left(R_{\text{AC}}(\omega - \omega_0) - j L_{\text{R}} \omega \omega_0^2\right) + R_{\text{AC}} (k_3 \omega \omega_0)^2}{\omega \left(L_{\text{R}} \omega \omega_0^2 + j R_{\text{AC}} \left(\omega^2 - \omega_0^2\right)\right)} \tag{3.39}$$

where

$$\begin{aligned} L_{\text{T}} &= \left(1 - k_{\text{T}}\right) L_{\text{AA}} \\ L_{\text{R}} &= \left(1 - k_{\text{R}}\right) L_{\text{aa}} \\ k_3 &= \frac{3}{2} k \end{aligned} \tag{3.40}$$

$$\Im\left(Z_{\text{A}}\right) = \frac{L_{\text{T}} \left(\omega_0^2 - \omega^2\right) \left(A + \left(\omega \omega_0^2 L_{\text{T}}\right)^2 \left(k_3^2 - 1\right)\right)}{\omega \left(\left(L_{\text{R}} \omega \omega_0^2\right)^2 + R_{\text{AC}} \left(\omega^2 - \omega_0^2\right)^2\right)} \tag{3.41}$$

and1

$$A = R_{\text{AC}}^2 \left(\left(\omega^2 - \omega_0^2\right)^2 \left(k_3^2 - 1\right) + k_3^2 \omega^2 \omega_0^2\right). \tag{3.42}$$

$$k_{\text{lim}} = \frac{L_{\text{R}} i_{2,\text{DC}}^2 \omega_0}{\sqrt{\left(L_{\text{R}} i_{2,\text{DC}}^2 \omega_0\right)^2 + \left(\frac{\pi^2}{4} P_{\text{out}}\right)^2}} \tag{3.43a}$$

$$P_{\text{out,lim}} = \frac{4}{\pi^2} \frac{\omega_0 L_{\text{R}} i_{2,\text{DC}}^2 \sqrt{1 - k_3^2}}{k_3} \tag{3.43b}$$

3.4 Initial sizing procedure

Before heading to the optimization of the three-phase inductive link, in this part the design procedure is going to be introduced for a particular case study. The work of this thesis is focused on the power supply of a railway system with a boarded storage system, similar to the one presented in [Herrera et al., 2015, Herrera et al., 2016]. In this application, the train is endowed with a battery pack, connected with a DC/DC converter to the internal DC bus. This DC/DC is capable of controlling the voltage level of the train. For this reason, the most simple IPT configuration is the Series-Series compensation, since the secondary is a voltage driven source. In addition, as detailed in section 3.2, in order to have the smallest coil, the star-star connection is preferred.

During this design procedure, all the system is going to be considered ideal. Ergo, the capacitors will be perfectly tunned and there will not be any losses in the windings. With this assumption, the output power will be equal to the input power, so the DC currents will be

$$i_{1,\text{DC}} = \frac{P_{\text{out}}}{V_{1,\text{DC}}} \tag{3.44}$$

for the transmitter side, and

$$i_{2,\text{DC}} = \frac{P_{\text{out}}}{V_{2,\text{DC}}} \tag{3.45}$$

for the receiver side. Thus for a three phase system, the AC currents per phase are

$$\hat{i}_{\text{A}} = \frac{\pi}{3} i_{1,\text{DC}} \tag{3.46}$$

$$\hat{i}_{\text{a}} = \frac{\pi}{3} i_{2,\text{DC}} \tag{3.47}$$

for each of the transmitter phases and receiver phases respectively.

In a Y-Y connection, the voltage that is produced between a phase and the neutral point is

$$\hat{v}_{\mathrm{A,n}} = \frac{2V_{1,\mathrm{DC}}}{\pi} \tag{3.48}$$

for the transmitter, and

$$\hat{v}_{\mathrm{a,n}} = \frac{2V_{2,\mathrm{DC}}}{\pi} \tag{3.49}$$

for the receiver.

So the peak mutual inductance that is necessary in order to transmit a certain power is

$$\hat{M} = \frac{2\hat{v}_{\mathrm{A,n}}}{3\omega\hat{i}_{\mathrm{a}}}. \tag{3.50}$$

Finally, to calculate the value of the self inductances, the coupling coefficient between the transmitter and the receiver coils must be known. The simplest way of obtaining this value is using a finite element method software. It is clear that the value of the coupling will vary with the position of the receiver. But as previously said in section 3.1, the maximum is achieved when the receiver coil is fully aligned with a coil window and its size is equal to half of the coil window λ. So simulating just this point will give the value of k that is needed.

At this point it has to be mentioned that, as explained in [Iruretagoyena et al., 2017b], the coupling coefficient does not depend on the number of turns of the coils. It depends exclusively on the area of both coils. For this reason, the easiest way of computing the coupling is to simulate both, transmitter and receiver coils, with just one turn that will cover the whole area.

As explained in [Iruretagoyena et al., 2017a], the optimal inductance ratio is achieved when

$$\chi = \chi_{\mathrm{lim}} = \left(\frac{V_{2,\mathrm{DC}}}{V_{1,\mathrm{DC}}}\right)^2 \tag{3.51}$$

So the value of the self inductances has to be

$$L_{\mathrm{A}} = \frac{\hat{M}}{k\sqrt{\chi}}, \tag{3.52}$$

$$L_{\mathrm{a}} = \chi L_{\mathrm{A}} \tag{3.53}$$

for the transmitter and receiver respectively.

In order to know the number of turns of each coil, the values for a single turn have to be obtained from the previous simulation. Then the turns are calculated with

$$N_{\mathrm{req}} = \sqrt{\frac{L_{\mathrm{req}}}{L_1}} \tag{3.54}$$

where N_{req} denotes the required number of turns, L_{req} is the desired inductance value and L_1 is the value of the inductance with a single turn.

However, it has to be mentioned that it is possible that the turns could not be fitted in the available space in either of the coils. In that case, both of the coils have to be adjusted to still have the desired mutual inductance and not exceed χ_{lim} .

3.5 Experimental validation

With the aim of validating the theory of this chapter, a 50W three-phase IPT is built. The objective of this prototype is to find gaps in the design procedure since they heavily rely on FEM calculations, and their accuracy must be ensured. In addition, effects like non ideal components in the inductive link and their importance is going be pointed out. Specially in the constant power transmission feature, it is the main reason why meander coils are used.

The specifications of the prototype are summarized in Table 3.1. Due to availability reasons, the Litz wire of 140x0.1mm is used with an overall external diameter of 1.65mm. For similar reasons, the MOSFETs C2M0080120D from Cree are used. Even though they are 1200V devices, the three-phase inverter is intended to be a generic solution for future projects with different voltage ratings. The input voltage is selected to be 24V, a standard voltage for grid connected commercial AC/DC rectifiers. This value is going to be fixed, so there will not be any power control. In order to make the system as simple as possible, the same voltage is chosen for the secondary side. Being so, both coils can have the same inductance and also the resonant capacitors for all phases can be equal. In this prototype, the load is going to be

Specifications		
Parameter	Variable	Value
Electric specifications		
Input voltage	$V_{1,\mathrm{DC}}$	24 V
Output voltage	$V_{2,\mathrm{DC}}$	24 V
Switching frequency	f_{sw}	100kHz
Output power	P_{out}	50 W
Geometric specifications		
Transmitter length	L_{T}	1300 mm
Transmitter width	W_{T}	150 mm
Receiver outer length	$L_{\mathrm{R,out}}$	112 mm
Receiver inner length	$L_{\mathrm{R,in}}$	5.5 mm
Receiver outer width	$W_{\mathrm{R,out}}$	150 mm
Receiver inner width	$W_{\mathrm{R,in}}$	45 mm
Separation	z	50 mm

Table 3.1: Specifications of the small scale prototype.

substituted by an equivalent resistance that will absorb those 50W at 24V.

For the modulation, the square wave signals are created with a TLC551CP timer. This timer runs at 1.2 MHz. Then with a Divide-By-Twelve decade counter SN74LS92N, the 100kHz and 120° delay are created. The dead time between upper and lower semiconductors are introduced with a comparator and a RC circuit. Each of the semiconductors is controlled by an independent driver, so the gate signals are individually transmitted.

Since in the future this prototype is going to be used as a demonstrator, LED lights are added to the moving part to make it more visual. Finally, the geometric specifications of the coils are taken from the distances of a real railway system. Being the scale 1:4 smaller than the real case.

Figure 3.14 depicts the CAD designed of the 50W demonstrator. Here the geometric parameters of Table 3.1 are indicated.

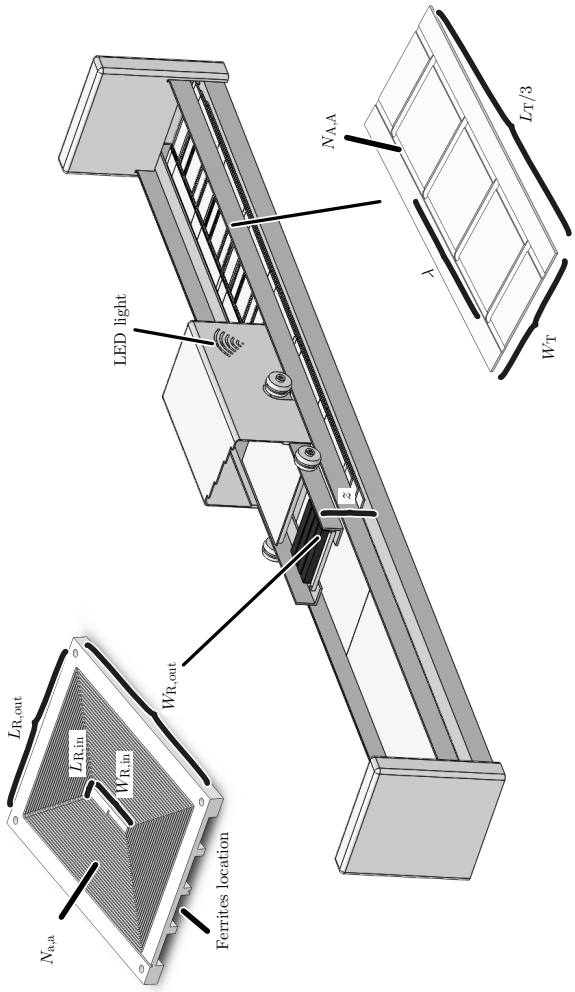

Figure 3.14: Solidworks drawing of the 50W prototype. In the left-upper part one of the receiver coils is zoomed. In the right-bottom part one piece of the transmitter coil is zoomed. Each of the phases is comprised of three of this pieces.

3.5.1 Case study

First of all, given the specifications, the mutual inductance that is needed to transmit those 50W is calculated. Following the steps shown in section 3.4, the calculations of Table 3.2 are carried out. From the peak current values, it can be calculated that the current density through the coils is $\sim 2\text{A/mm}^2$, so no forced cooling is required.

Initial calculations

Parameter	Variable	Equation	Value
Input DC current	$i_{1,\text{DC}}$	$\frac{P_{\text{out}}}{V_{\text{out}}}$	2.08 A
Output DC current	$i_{2,\text{DC}}$	$\frac{P_{\text{out}}}{V_{\text{in}}}$	2.08 A
Input AC peak current	$\hat{i}_{\text{A}}$	$\frac{\pi}{3} i_{1,\text{DC}}$	2.18 A
Output AC peak current	$\hat{i}_{\text{a}}$	$\frac{\pi}{3} i_{2,\text{DC}}$	2.18 A
Input AC peak voltage	$\hat{v}_{\text{A,n}}$	$\frac{2}{\pi} V_{1,\text{DC}}$	15.27 A
Output AC peak voltage	$\hat{v}_{\text{a,n}}$	$\frac{2}{\pi} V_{2,\text{DC}}$	15.27 A
Mutual inductance	$\hat{M}$	$\frac{2\hat{v}_{\text{A,n}}}{3\omega\hat{i}_{\text{a}}}$	7.43 μH
Inductance ratio	χ	$\left(\frac{V_{\text{out}}}{V_{\text{in}}}\right)^2$	1

Table 3.2: Mutual inductance calculation for the 50W small-scaled prototype.

Once the desired value is known, the inductances of the coils plus the mutual inductance are simulated with FLUX® for a single turn, see Table 3.3. With this coupling coefficient, the pretended self inductances of the transmitter and receiver coils are calculated and the number of turns adjusted, i.e $N_{\text{A,A}}$ and $N_{\text{a,a}}$ are calculated. Taking into account that the outer diameter of the wire is 1.65mm, the total width and

length of the receiver coil have to be at least 108.9mm. For the given specifications there is not enough space. In addition, extra space is necessary to make the coil formers.

FEM simulation results for a single turn

Parameter	Variable	Value
Coupling coefficient	k	0.05
Transmitter inductance	$L_{\mathrm{A,A}\rightarrow\mathrm{N=1}}$	5.2041 μH
Receiver inductance	$L_{\mathrm{a,a}\rightarrow\mathrm{N=1}}$	0.1104 μH
Transmitter inductance	$L_{\mathrm{A,A}}$	141.0738 μH
Receiver inductance	$L_{\mathrm{a,a}}$	141.0738 μH
Transmitter turns	$N_{\mathrm{A,A}}$	$5.2 \approx 5$
Receiver turns	$N_{\mathrm{a,a}}$	$35.74 \approx 36$

Table 3.3: FLUX simulation results for a single turn case and the calculation of the turns.

For this reason, the maximum number of turns that can be fitted properly in the receiver coils is set to 27 turns. Thus the values of the inductances have to be once again calculated, see Table 3.4.

As it can be observed in Table 3.4, the resulting number of turns of the transmitter coil is 7.26. However this can not be built in the real system, and, the number must be rounded down. Thus, the transmitter coil will have 7 turns. With a mutual inductance 0.96% smaller than the desired one, 7.16μH vs. 7.43μH. This will mean that the system will actually deliver more power. Nevertheless, it has to be kept in mind that the desired mutual inductance is calculated for the ideal case. Thus in a real situation a lower mutual inductance has to be built to meet the power requirements.

With these new values new FEM simulations have been carried out. As expected, the values of the self inductance are almost equal to the predicted number, see Table 3.5. The slight difference comes from the real position of the turns. In this simulation, each of the transmitter turns have been considered cylindrical and a space between them, so the coil is not covering exactly the same surface. Nevertheless, the accuracy

Number of turns calculation

Parameter	Variable	Value
Receiver turns	$N_{\mathrm{a,a}}$	27
Receiver inductance	$L_{\mathrm{a,a}}$	80.5 μH
Transmitter turns	$N_{\mathrm{A,A}}$	$7.26 \approx 7$
Transmitter inductance	$L_{\mathrm{A,A}}$	274.31 μH $\approx$ 255 μH
Mutual inductance	$\hat{M}$	7.16μH
Output power	P_{out}	51.86 W

Table 3.4: Recalculation of the inductances with the constraint of 27 turns at the receiver coils.

is good enough.

Mutual and self inductance FEM simulation

Parameter	Variable	Value	Diff. calc.
Transmitter self inductance	L_{AA}	251.4 μH	-1.41%
	L_{BB}	251.2 μH	-1.49%
	L_{CC}	254.2 μH	-0.31%
Receiver self inductance	L_{aa}	80.53 μH	0.03%
	L_{bb}	78.87 μH	-2.02%
	L_{cc}	80.03 μH	-0.58%
Transmitter mutual inductance	M_{AB}	-50.32 μH	-
	M_{BC}	-50.79 μH	-
	M_{CA}	-43.66 μH	-
Receiver mutual inductance	M_{ab}	-0.30 μH	-
	M_{bc}	-0.35 μH	-
	M_{ca}	-0.03 μH	-

Table 3.5: Self and mutual inductances for $N_{\mathrm{A,A}} = 7$ and $N_{\mathrm{a,a}} = 27$.

In addition, this same simulation is used to calculate the mutual inductances among the transmitter coils and among receiver coils. It can be observed that this coupling is high for the transmitter coil and can not be neglected. It is equivalent to have a coupling coefficient of

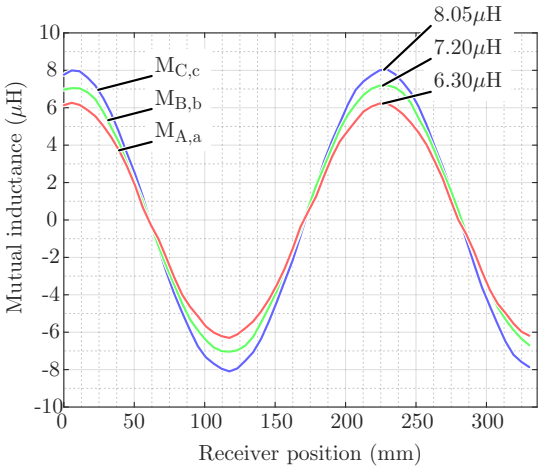

Figure 3.15: Simulated mutual inductance for a geometric period $\lambda = 224$mm.

0.2. On the contrary, for the receiver coil, the coupling is negligible, the coupling coefficient is lower than 0.004.

Figure 3.15 represents the mutual inductances $M_{\mathrm{A,a}}$, $M_{\mathrm{B,b}}$ and $M_{\mathrm{C,c}}$, were ABC are the transmitter coils and abc are the receiver coils. It can be observed that the peak value of B phase is almost equal to the desired one. For this simulation, the trasnmitter phases A and C have been displaced from the original point (see Figure 3.16). A is 4mm further from the receiver, $\mathrm{z_{A,a}}$, and C is 4mm closer, $\mathrm{z_{C,a}}$. As a consequence, the peak mutual inductance of phase A is slightly lower and phase B is higher. This entails that the current through the phase A is going to be the highest and for phase C the lowest.

Going back to the design process, the last thing that needs to be done is calculate the capacitance values. First taking into account the coupling among phases the equivalent inductance is calculated with

$$\begin{aligned} L_{\mathrm{T,A}} &= L_{\mathrm{A,A}} - M_{\mathrm{A,B}} - M_{\mathrm{A,C}} + M_{\mathrm{B,C}} = 297.76\mu\mathrm{H} \\ L_{\mathrm{T,B}} &= L_{\mathrm{B,B}} - M_{\mathrm{B,A}} - M_{\mathrm{B,C}} + M_{\mathrm{A,C}} = 316.26\mu\mathrm{H} \\ L_{\mathrm{T,C}} &= L_{\mathrm{C,C}} - M_{\mathrm{C,A}} - M_{\mathrm{C,B}} + M_{\mathrm{A,B}} = 293.55\mu\mathrm{H} \end{aligned} \tag{3.55}$$

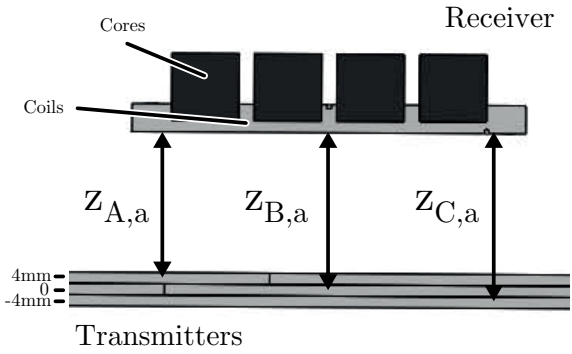

Figure 3.16: Location of the transmitter coils. Taking as origin and reference distance phase B, phase A is displaced 4mm towards the receiver coils whereas phase C is 4mm away.

for the transmitter coil, and with

$$\begin{aligned} L_{\mathrm{T,a}} &= L_{\mathrm{a,a}} - M_{\mathrm{a,b}} - M_{\mathrm{a,c}} + M_{\mathrm{b,c}} = 81.10\mu\mathrm{H} \\ L_{\mathrm{T,b}} &= L_{\mathrm{b,b}} - M_{\mathrm{b,a}} - M_{\mathrm{b,c}} + M_{\mathrm{a,c}} = 78.90\mu\mathrm{H} \\ L_{\mathrm{T,c}} &= L_{\mathrm{c,c}} - M_{\mathrm{c,a}} - M_{\mathrm{c,b}} + M_{\mathrm{a,b}} = 80.07\mu\mathrm{H} \end{aligned} \tag{3.56}$$

for the receiver. As B is in the middle of the other two, the mutual inductance seen by the inverter leg is higher. So the resonance capacitor should be properly adjusted. Calculating with (3.22) and (3.23), the capacitance values of the transmitter side are

$$\begin{aligned} C_{\mathrm{A}} &= \frac{1}{\omega_0^2 \left(L_{\mathrm{A,A}} - M_{\mathrm{A,B}} - M_{\mathrm{A,C}} + M_{\mathrm{B,C}}\right)} = 8.5070\mathrm{nF} \approx 8.5\mathrm{nF} \\ C_{\mathrm{B}} &= \frac{1}{\omega_0^2 \left(L_{\mathrm{B,B}} - M_{\mathrm{B,A}} - M_{\mathrm{B,C}} + M_{\mathrm{A,C}}\right)} = 8.0093\mathrm{nF} \approx 8.0\mathrm{nF} \\ C_{\mathrm{C}} &= \frac{1}{\omega_0^2 \left(L_{\mathrm{C,C}} - M_{\mathrm{C,A}} - M_{\mathrm{C,B}} + M_{\mathrm{A,B}}\right)} = 8.6288\mathrm{nF} \approx 8.5\mathrm{nF}. \end{aligned} \tag{3.57}$$

Whereas for the receiver part are

$$\begin{aligned} C_{\mathrm{a}} &= \frac{1}{\omega_0^2 \left(L_{\mathrm{a,a}} - M_{\mathrm{a,b}} - M_{\mathrm{a,c}} + M_{\mathrm{b,c}}\right)} = 31.232\mathrm{nF} \approx 32.0\mathrm{nF} \\ C_{\mathrm{b}} &= \frac{1}{\omega_0^2 \left(L_{\mathrm{b,b}} - M_{\mathrm{b,a}} - M_{\mathrm{b,c}} + M_{\mathrm{a,c}}\right)} = 32.101\mathrm{nF} \approx 32.0\mathrm{nF} \\ C_{\mathrm{c}} &= \frac{1}{\omega_0^2 \left(L_{\mathrm{c,c}} - M_{\mathrm{c,a}} - M_{\mathrm{c,b}} + M_{\mathrm{a,b}}\right)} = 31.635\mathrm{nF} \approx 32.0\mathrm{nF}. \end{aligned} \tag{3.58}$$

In order to select the capacitors, apart from the capacitance value, the voltage that they must withstand is also important. Considering that the system is ideally tunned, the transmitter capacitor voltages are given by

$$\begin{aligned} \hat{v}_{C_{\mathrm{A}}} &= \frac{1}{\omega_0 C_{\mathrm{A}}} \hat{i}_{\mathrm{A}} = \frac{1}{2\pi 100\mathrm{k}\ 8.5\mathrm{n}} 2.08 = 389.46\mathrm{V} \\ \hat{v}_{C_{\mathrm{B}}} &= \frac{1}{\omega_0 C_{\mathrm{B}}} \hat{i}_{\mathrm{B}} = \frac{1}{2\pi 100\mathrm{k}\ 8.0\mathrm{n}} 2.08 = 413.80\mathrm{V} \\ \hat{v}_{C_{\mathrm{C}}} &= \frac{1}{\omega_0 C_{\mathrm{C}}} \hat{i}_{\mathrm{C}} = \frac{1}{2\pi 100\mathrm{k}\ 8.5\mathrm{n}} 2.08 = 389.46\mathrm{V} \end{aligned} \tag{3.59}$$

While the receiver capacitors are,

$$\begin{aligned} \hat{v}_{C_{\mathrm{a}}} &= \frac{1}{\omega_0 C_{\mathrm{a}}} \hat{i}_{\mathrm{a}} = \frac{1}{2\pi 100\mathrm{k}\ 32.0\mathrm{n}} 2.18 = 108.42\mathrm{V} \\ \hat{v}_{C_{\mathrm{b}}} &= \frac{1}{\omega_0 C_{\mathrm{b}}} \hat{i}_{\mathrm{b}} = \frac{1}{2\pi 100\mathrm{k}\ 32.0\mathrm{n}} 2.18 = 108.42\mathrm{V} \\ \hat{v}_{C_{\mathrm{c}}} &= \frac{1}{\omega_0 C_{\mathrm{c}}} \hat{i}_{\mathrm{c}} = \frac{1}{2\pi 100\mathrm{k}\ 32.0\mathrm{n}} 2.18 = 108.42\mathrm{V} \end{aligned} \tag{3.60}$$

Special care has to be taken when selecting the capacitors. The voltage ratings decrease when increasing the frequency (see Figure 3.17). For this prototype, due to availability, capacitors of 1nF and a voltage of 700V@100kHz are used.

3.5.2 Measurements

Once the coil is mounted, see Figure 3.18, first the inductances and resistances are measured with the Agilent 4285A RLC meter. Table 3.6 summarizes the measurements for the parameters that do not change

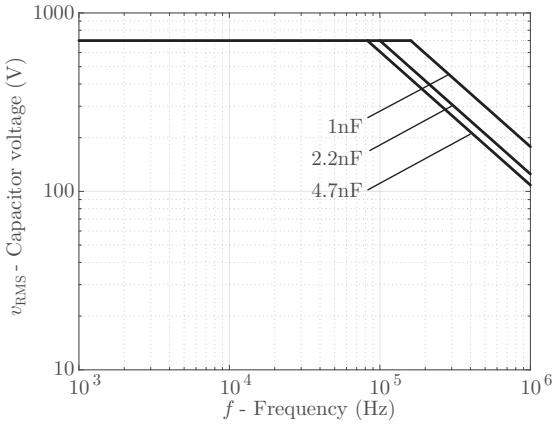

Figure 3.17: Derating of the capacitor voltage depending on the capacitance value and the waveform frequency.

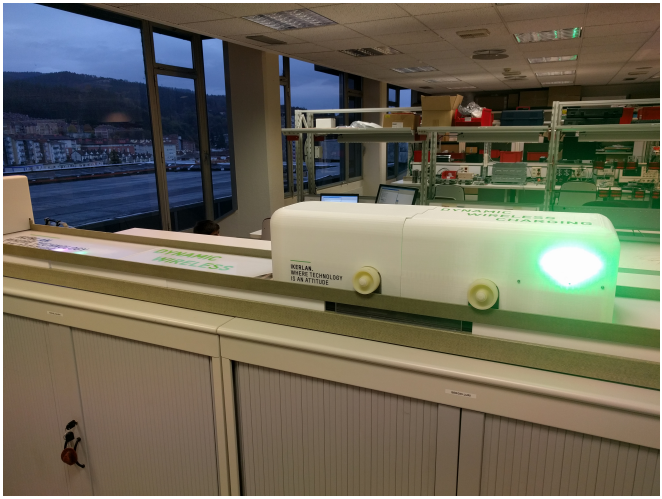

Figure 3.18: 50W small-scale three-phase IPT charger.

with the position of the receiver coil. Besides, Figure 3.19 depicts the mutual inductance for various receiver positions.

Due to the low available space, in order to build the meander coil,

Measurements

Parameter	Variable	Value	Diff. sim.
Transmitter self inductance	L_{AA}	255.69 μH	+1.70%
	L_{BB}	257.15 μH	+2.36%
	L_{CC}	251.54 μH	-1.04%
Receiver self inductance	L_{aa}	86.13 μH	+6.95%
	L_{bb}	85.81 μH	+8.79%
	L_{cc}	86.44 μH	+8.00%
Transmitter mutual inductance	M_{AB}	-50.58 μH	-0.51%
	M_{BC}	-50.58 μH	-0.41%
	M_{CA}	-42.03 μH	-3.73%
Receiver mutual inductance	M_{ab}	0.0 μH	-
	M_{bc}	0.0 μH	-
	M_{ca}	0.0 μH	-
Transmitter wire resistance	R_{AA}	2.65 Ω	-
	R_{BB}	2.59 Ω	-
	R_{CC}	2.61 Ω	-
Receiver wire resistance	R_{aa}	0.39 Ω	-
	R_{bb}	0.41 Ω	-
	R_{cc}	0.37 Ω	-
Load resistance	R_{DC}	11.5 Ω	-

Table 3.6: Inductance and resistance values for the 50W prototype.

each of the turns is mounted separately and afterwards all are connected in series. This soldering, increases the winding resistance as it can be seen in Table 3.6, where the resistance of the transmitter coil is much higher compared to the receiver coil (the receiver coil is not soldered). The measured quality factor for the transmitter coils Q_1 is ~ 60. For the receiver coils, the measured quality factor Q_2 is ~ 140, comparatively higher.

Besides, for the inductance measurements, it can be observed that the accuracy is acceptable. The biggest error is around 9%, given at the self inductances of the receiver coils. Since this coil is simulated as a single coil with N turns, the spacing in between the wires is not considered. Another reason can also be the ending terminals that increase the value. Taking all into account, it can be said that FEM simulations offer enough accuracy.

As previously said, Figure 3.19 depicts the mutual inductance for

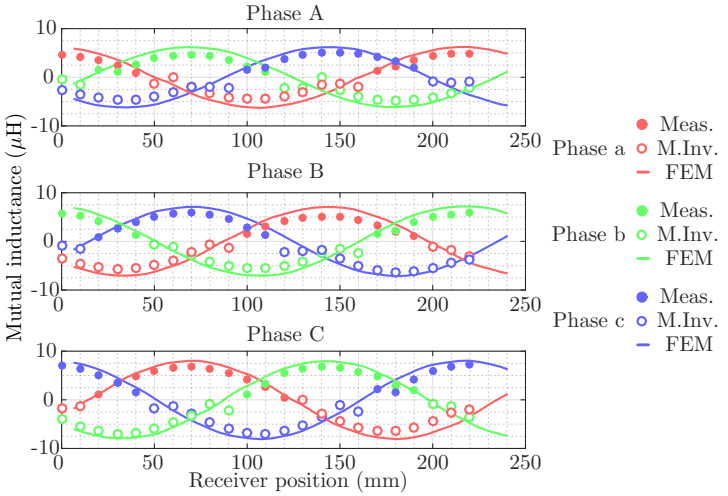

Figure 3.19: Mutual inductance FEM simulations and measurements for the 50W small-scale prototype. The empty circles are measured as positive values as in [Iruretagoyena et al., 2017c]. However, from Figure 3.2 it is known that those values are negative. So, for better visualization, this values have been reflected to the negative part.

the three transmitter coils and the three receivers, labeled ABC and abc respectively. As previously seen in the FEM simulation, the mutual inductance for phase A is the lowest and for phase C the highest. This effect is also illustrated in Figure 3.20(a) where the peak values of the currents are depicted. It can be observed that generally the current through phase A is higher. The ripple that appears is due to the alignment of the coils. In the simulation, all the turns of a phase can be placed in the same position, respecting λ in all of them. However in reality this is not possible, so some of the turns will have higher coil windows and others smaller. Nevertheless, this amplitudes correspond with the initially calculated 2.18A. Figure 3.20(b) represents the current of the three phases for two different receiver positions. It can be noticed that even the phases are not equal, the angle between them is close to 120°.

In Figure 3.21 the voltage through a coil and the voltage of its leg is illustrated. It can be concluded that the turn-off is done while there is positive current so this phase is working in the inductive zone. However,

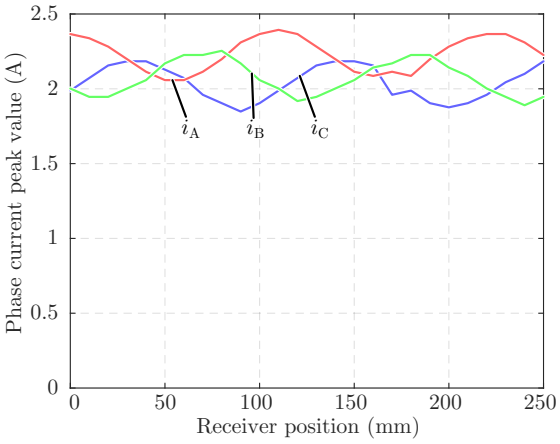

(a)

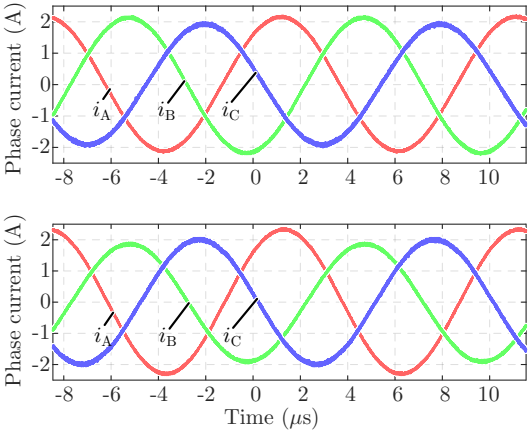

(b)

Figure 3.20: (a) Peak current variation through a geometric period. (b) Three-phase current distribution for two different receiver positions.

a single spike can be appreciated in the voltage square wave. This indicates that one of the other phases is working also in the inductive zone but the third one is in a capacitive one.

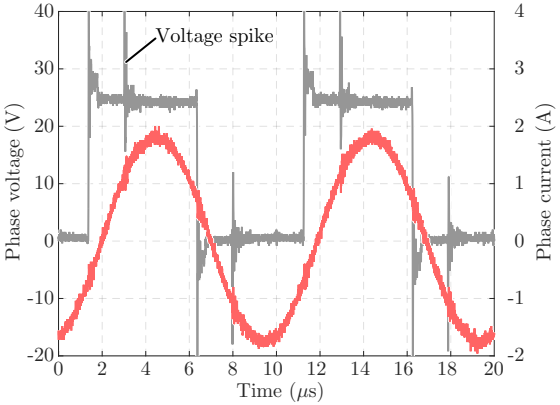

Figure 3.21: Phase voltage and current. Even though this phase is in an inductive zone, from the voltage waveform it can be concluded that one of the other phases is in a capacitive zone.

Finally, the output power is shown in Figure 3.22. This power is obtained measuring the output voltage at the receiver DC part. It can

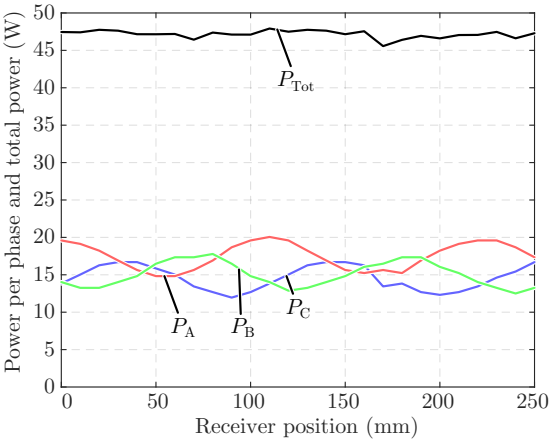

Figure 3.22: Output power through a geometric period. Even though the phase power fluctuate, the total output power keeps constant.

be seen that even though the currents are not constant, the output

power is almost equal for any point. Furthermore, this value is close to the designed 50W value. Even though the mutual inductances are lower, and this will mean that the power should be bigger, due to the losses in the system the achieved outcome is lower. This fact is clearly reflected in the efficiency of the system in Figure 3.23.

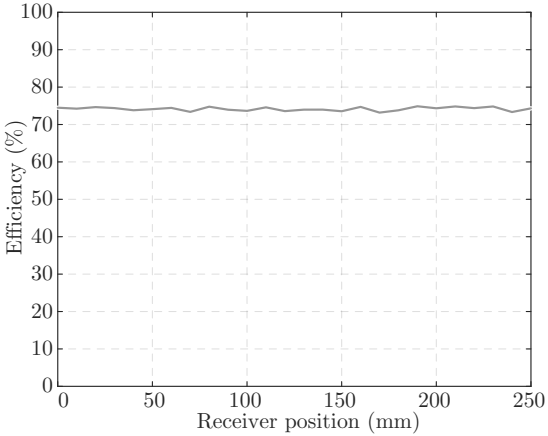

Figure 3.23: Efficiency for a geometric period. The efficiency is kept constant through all the charging lane at approximately 70%.

The achieved efficiency is around 70%, mainly due to the losses in the transmitter coils and also because on of the phases is switching in a capacitive zone. Nevertheless, this efficiency is similar to other prototypes that can be found in the literature [Choi et al., 2013, Choi et al., 2015, Huh et al., 2010, Huh et al., 2011].

3.6 Conclusions

In this chapter the three-phase IPT system has been analyzed. First, the sinusoidal magnetic field generation using meander coils has been explained. Afterwards, the mutual inductance calculation has been detailed. It has been made clear that the main advantage of this sinusoidal shape is that knowing the geometrical period and the maximum mutual inductance, the behavior for any position can be estimated. However, it has been demonstrated that in order to achieve constant power trans-

mission, multi-phase coil is necessary. Furthermore, it has been shown that the minimum number of phases is three. Then, the connection between the phases has been analyzed. The main conclusion is that for a given power, the optimal solution is a star-star connection, since a lower mutual inductance is needed. Afterwards, the three-phase SAB has been analyzed. Due to the low power capability, also compensation topologies are needed. In the next part, the compensation topologies have been analyzed and the limits for bifurcation for series-series and series-parallel have been obtained. Finally a small scale 50W prototype has been designed and validated. Even the differences among the phases the transferred output power is constant for any given receiver position.

Chapter 4

Design, optimization and experimental validation of a 9kW three-phase IPT system

The calculations introduced in the previous chapter will form the basis for the optimization of the 9kW three-phase IPT system developed in this chapter. Compared to the previous 50W prototype where all dimensions where previously defined and only the number of turns of the transmitter and the receiver coils where calculated, in this new design different aspects like coil size, coil window and number of ferrite cores are going to be analyzed.

Considering the size limits, all the feasible solutions are shown in plots comparing: efficiency vs. size ($\eta - \mathrm{s_z}$) and efficiency vs. weight ($\eta - \mathrm{w_g}$). As shown in [Bosshard et al., 2015] for the single phase case, a trade-off exists between those elements and a Pareto-Front is created at the limit. In this chapter this analysis is extended for the three-phase IPT system. In addition, efficiency vs. cost ($\eta -$ €) and receiver voltage vs. weight ($V_\mathrm{R} - \mathrm{w_g}$) are also going to be analyzed.

This chapter is structured as follows: first in section 4.1 the optimization techniques are introduced. Afterwards, in section 4.2, the three-phase optimization routine is going to be explained and applied

to a 9kW design. The Pareto-Fronts are obtained and the effect of each of the parameters is discussed. In section 4.3, the chosen solution is analyzed and more detailed simulations are carried out. Finally in section 4.4, the prototype that has been built is presented, inductance measurements are executed and afterwards the experimental validation is carried out.

4.1 Optimization Methodology

In recent years, thanks to the development of computers with large memory and fast speed, huge amount of simulations can be carried out in a very short time lapse. In addition, the high accuracy in electric and electromagnetic softwares enable designers to calculate many solutions without needing to build prototypes for each case. This trend is clearly noticeable in the literature, where recently many publications can be found concerning optimization of power electronic systems with large amount of simulations [Bosshard et al., 2015, Subotic et al., 2016, Burkart and Kolar, 2017, Flankl et al., 2017, Mogorovic and Dujic, 2017].

4.1.1 Decision criteria

In most of the cases, the optimization is carried out comparing different performance indicators, typically efficiency, cost, volume and reliability are analyzed. In addition, some limiting factors are added, such as maximum temperature, maximum voltage, etc. Then, multi-objective optimization algorithms are applied to find the optimum solution [Raggl et al., 2009, Nussbaumer et al., 2009]. According to [Garcia Bediaga, 2014], those optimization algorithms can be classified into three main groups:

- **A priori:** decisions before calculation (eg. weighting factors, k_1, k_2, k_3).
- **Progressive:** decision during calculation (eg. interactive).
- **A posteriori:** decision after calculation (eg. Pareto-Front analysis).

Using *a priori* or *progressive* methods, any multi-objective formulation with many performance indicators (P_1, P_2, P_3) can be converted to a single-objective problem. Then, the optimization will find a unique optimal solution, which will depend on the values assigned to the weighting factors k_1, k_2, k_3. That is to say, the solution will be optimal when the cost function

$$F = k_{\mathrm{P}1}P_1 + k_{\mathrm{P}2}P_2 + k_{\mathrm{P}3}P_3 + \dots \tag{4.1}$$

is minimized or maximized.

One of the easiest methods to depict and explain this type of optimizations is the spider chart, see Figure 4.1. In this illustrative example, three different solutions (case A, case B and case C) are shown with eight performance indicators (P1 to P8). Depending on the initial decisions, any of these three solutions can be optimal. For example, if the highest weighting factors are given to P_2, P_4 and P_7, Case C is the most likely to be the optimal. Besides, if P_1 and P_8 are considered the most important, Case A will be optimal. According to [Kolar et al., 2010], setting those weighting factors is not always an easy task and largely depends on the application and the experience of the designer.

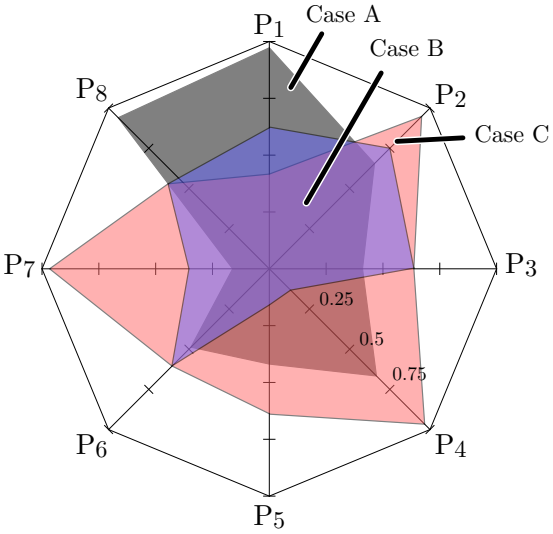

Figure 4.1: Spider chart with 7 performance indicators.

Besides, using *a posteriori* method, i.e. Pareto-Front optimization, see Figure 4.2, all the feasible solutions are presented and the optimal selection is done afterwards, knowing all the information. The Pareto-Front is the line or surface where in order to improve one performance indicator another one is worsened. So, in this type of optimizations, two or more countering performances are compared. One of the most typical countering indicators are efficiency and size. If a very efficient system is desired, the system has to be bigger. Similarly, if a very compact system is designed, the efficiency is penalized. With variations of components, modulations or topologies, optimal solutions can be compared [San-Sebastian et al., 2013].

The main drawback of this strategy is that when many performances are evaluated at the same time, plotting them is not intuitive. So, typically a pair of indicators is drawn in each plot.

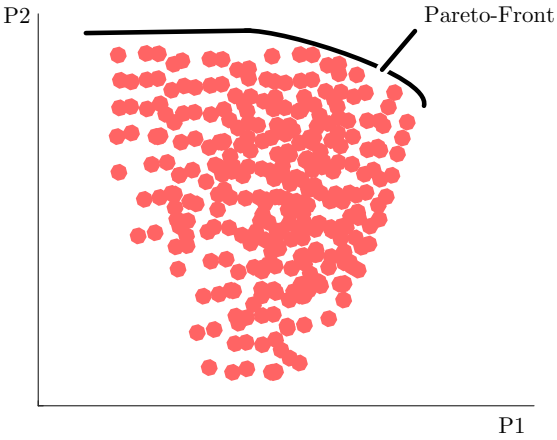

Figure 4.2: Pareto-front with two performance indicators, P1 and P2.

In late works, these multi-objective optimizations have been mostly used for the design of low voltage PFC and resonant converters, evaluating efficiency and power density barriers [Kolar et al., 2007, Badstuebner et al., 2011]. Recently the scope has been extended towards medium voltage (MV) converters [San-Sebastian et al., 2013, Ortiz, 2014, Huber, 2016]. This way, the feasible solutions are evaluated and ultra-compact or ultra-efficient converters are designed.

Those same objectives can be found in transformers [Dujic and

Mogorovic, 2017] and in single-phase IPT systems [Bosshard, 2015]. In transportation applications space and weight are two of the most important and demanding factors. The coils should be as small as possible, in order to fit beneath the chassis and the weight should also be as small as possible, to lower the power consumption. Apart from these, also the cost is an important indicator. Manufacturers alway seek for the cheapest solution. In addition, meander type coils offer another important criteria, being the phases sticked one to the other, the voltage of the transmitter inductance should also be minimized. This way, the insulation can be reduced and also the voltage ratings of the capacitors can be kept low.

4.1.2 Flow-chart

Thus, the objective of the upcoming optimization is to obtain the Pareto-Fronts for the following indicators: efficiency(η), weight ($\mathrm{w_g}$), coil size ($\mathrm{s_z}$), cost (€) and coil voltages (V_{L1} and V_{L2}). For that purpose the design flow chart depicted in Figure 4.3 is going to be followed.

First of all, the electric and geometric specifications have to be obtained. For this particular optimization the electric specifications considered are: the input nominal DC voltage ($V_{1,\mathrm{DC}}$), the output nominal DC voltage ($V_{2,\mathrm{DC}}$), the switching frequency (f_{sw}) and the nominal power that is demanded (P_{out}). Besides, the geometric specifications are: the length of the charging lane (L_{T}), the width of the charging lane (W_{T}), the distance to the receiver coil (z) and the maximum size of the receiver coil ($W_{\mathrm{R,out\ max}}$).

Following the same design procedure of section 3.4, in the second step of the flow chart, the AC currents $\hat{i}_{\mathrm{A}}$ and $\hat{i}_{\mathrm{a}}$ plus the mutual inductance $\hat{M}$ that is required are calculated. In addition also the bifurcation limit can be used to know the values of the self inductances. As it was observed in the small scale prototype, section 3.5, it is not always possible to achieve the optimal inductance ratio. In addition, the number of turns of the meander coils have to be an integer number. Otherwise, the mutual inductance will not be equal in all the charging lane. So, it is advisable to obtain also the Pareto for different transmitter turns.

Once the currents and the frequency are known, using Figure 2.27 and Figure 2.28, the litz wire that minimizes the high frequency AC effects is selected. Selecting the litz wire, the outer diameter is therefore known.

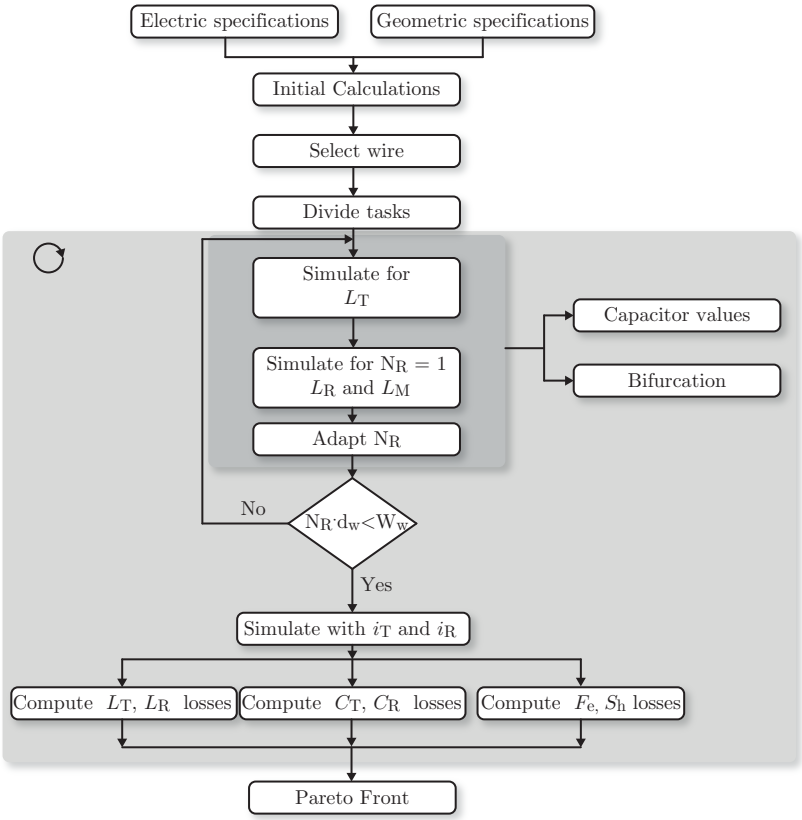

Figure 4.3: Optimization methodology flow-chart.

The fourth step of the flow-chart is carried out by FEM simulations, where in each iteration one of the parameters is varied. In the first simulation, supplying only the meander coil and measuring the circulating magnetic flux through it, the value of the self inductance of the transmitter is obtained. Afterwards, in the second simulation, the current of the transmitter is set to zero and the receiver coil is supplied. Then, measuring the flux through it, the self inductance of the receiver is calculated. In this same simulation, the magnetic flux circulating through the transmitter coil is measured. So, dividing this value with the receiver current, the mutual inductance is obtained for a single turn

receiver. Note that this simulation has to be done with the receiver coil fully aligned with the transmitter coil window. Therefore, knowing the desired mutual inductance and that the value of L_1 is not going to be changed, the number of turns of the receiver is calculated with (3.54). Is after this step when the feasibility of the solution is checked. If the diameter times the number of turns is higher than the available space, the solution is discarded and the optimization continues with a new iteration. Notice that in all these simulations, only one of the transmitter and one of the receiver coils is sufficient. As the rest of the coils are assumed to be equal.

If the solution is feasible, out of the FEM simulation, the capacitor values and its ESR are calculated. Furthermore, the bifurcation limit is also checked.

Afterwards, in the third FEM simulation all three transmitter coils are simulated. In this step, all coils are supplied with the initially calculated AC currents. Then the losses in the aluminum and in the ferrite cores are calculated. The reason of using all the coils in this simulation is that the losses are not proportional to the magnetic field, see equation 2.63[1]. Apart from that, since the length of the coils are also known, the DC resistance can be calculated and then the power losses. Once the FEM simulations are finished, with the current values and the ESR, the losses in the capacitors are estimated.

Afterwards, adding up all the losses (aluminum, ferrites, coils and capacitors), the efficiency of the system is calculated. During this simulations, since the coupling between receivers is negligible, only one coil is used for the calculations and then the losses are multiplied by three.

Finally, after all the iterations and calculations have finished, all the data is collected and the Pareto-Fronts are drawn.

4.2 System optimization

4.2.1 Specifications

Increasing power is not a straightforward step. In kilowatt order applications, the availability of the components specially capacitors is considerably lower. In addition, the cost of each of them is much higher compared to the low power samples. For an IPT system, the value

[1]Equation 2.63 is already integrated in the FEM simulator loss calculation.

of the capacitors is extremely important, since they establish the resonance frequency. For these reasons and as the main objective of this prototype is to validate the optimization methodology and the three-phase IPT concept, in this work the output power is specified to be 9kW. With these power level, the challenges that offers high power, such as high capacitor voltages are well represented. Hence, an array of capacitors can be built to meet the current, and more important, the voltage requirements. Table 4.1 summarizes the electric and geometric specifications for the three-phase IPT system that is wanted to optimize.

Specifications

Parameter	Variable	Value
Electric specifications		
Max. input voltage	$V_{1,\mathrm{DC,max}}$	520 V
Max. output voltage	$V_{2,\mathrm{DC,max}}$	600 V
Switching frequency	f_{sw}	100kHz
Output power	P_{out}	9 kW
Geometric specifications		
Transmitter length	L_{T}	2800 mm
Transmitter width	W_{T}	400 mm
Transmitter coil period	λ	800 mm
Max. receiver outer length	$L_{\mathrm{R,out,max}}$	450 mm
Max. receiver outer width	$W_{\mathrm{R,out,max}}$	450 mm
Separation	z	100 mm

Table 4.1: Specifications of the 9kW prototype.

As it has been demonstrated in the previous small-scale prototype, even though the overall coupling is constant, considering each phase individually, the coupling slightly varies. For this reason, the best option is to use a Series-Series compensation, as it is the only compensation topology that is independent of the coupling and the transmitted power. Furthermore, as for the low-scale prototype, a voltage source inverter is used, so a series compensation is mandatory in the transmitter side.

For this prototype standard ferrite cores are going to be used. Once more the I shape cores are chosen. The dimensions of each of the ferrites are 155x25x25. The transmitter coil will not have any ferrite cores. In a real application, it would be extremely expensive to add ferrite cores

through all the charging line, as it will be shown later the cores are one of the most expensive parts of the coil. So, in order to still improve the coupling, ferrites will be added only in the back part of the receiver coils.

In addition, an aluminum plate is going to be placed behind each receiver. This way, the electronic of the receiver part will be protected from the magnetic field. As a consequence, eddy currents are generated in the aluminum, but the field is reduceds. As previously said, this aluminum losses are also considered in the optimization routine.

In the final assembly, the secondary part will also be substituted by an equivalent resistor. As shown in the 50W prototype, it offers a simple solution for validating the power transmission.

4.2.2 Initial sizing

Starting with the optimization routine, the first step is to calculate the AC currents and voltages, and the mutual inductance that is needed. These calculations, Table 4.2, are equal to the ones previously presented in section 3.4.

In this 9kW prototype, since the coil size (and as a consequence the inductance value) and the currents are much higher, the voltage that will be generated in the coils and also in the capacitors is going to be large. As previously mentioned, it is specially problematic in the meander coil; since the turns are place one next to the other, the insulation must be correctly chosen. Otherwise, an electric arc can be produced, damaging the wire and the system.

Parameter	Variable	Equation	Value
Input DC current	$i_{1,\mathrm{DC}}$	$\frac{P_{\mathrm{out}}}{V_{\mathrm{in}}}$	17.3 A
Output DC current	$i_{2,\mathrm{DC}}$	$\frac{P_{\mathrm{out}}}{V_{\mathrm{out}}}$	15 A
Input AC peak current	$\hat{i}_{\mathrm{A}}$	$\frac{\pi}{3} i_{1,\mathrm{DC}}$	18.12 A
Output AC peak current	$\hat{i}_{\mathrm{a}}$	$\frac{\pi}{3} i_{2,\mathrm{DC}}$	15.70 A
Input AC peak voltage	$\hat{v}_{\mathrm{A,n}}$	$\frac{2}{\pi} V_{1,\mathrm{DC}}$	331.04 V
Output AC peak voltage	$\hat{v}_{\mathrm{a,n}}$	$\frac{2}{\pi} V_{2,\mathrm{DC}}$	381.97 V
Mutual inductance	$\hat{M}$	$\frac{2\hat{v}_{\mathrm{A,n}}}{3\omega\hat{i}_{\mathrm{a}}}$	22.36 μH

Table 4.2: Mutual inductance calculation for the 9kW prototype.

4.2.3 Litz wire

Once the currents and its frequency are known, the litz wire is selected. Since only natural convection is going to be used, the compromise of having less than 6 A/mm^2 has been taken. This leads to a minimum total wire area of 2.1mm^2. Besides, considering the skin effect (Figure 2.27) and internal proximity effect (Figure 2.28), the strand diameter has to be smaller than 0.1mm. Searching in a litz wire catalog, the wires of Table 4.3 that meet the requirements are analyzed [2].

Figure 4.4 illustrates the current distribution whereas Figure 4.5 depicts the AC resistance for the aforementioned litz wires. It can be observed that for the strand diameters 0.1mm and 0.2mm, the AC resistance at 100kHz increases noticeably. So the best option is to use a 0.071mm strand. Comparing the remaining wires, with 735 strands the resistance is lower as the area is higher. However also the diameter of this wire is bigger. Even though both solutions are valid, in this work the litz 0.071x630 is chosen. This way more turns could be fitted in

[2] 0.2mm strand is used for comparison.

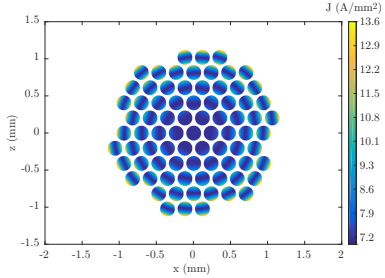

(a)

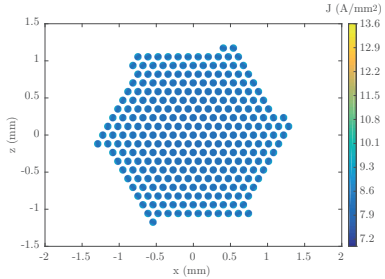

(b)

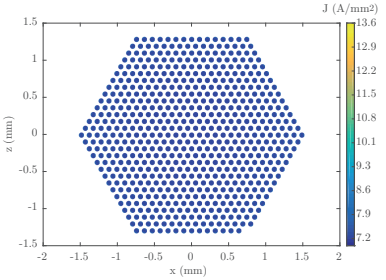

(c)

Figure 4.4: Distribution of the current through the litz wire strands at 100 kHz. The current flows in y direction with an amplitude of 18.12A. (a) Wire composed by 0.2mmx80 strands. The maximum current density is $J_{\max} = 13.6\text{A/mm}^2$ and the minimum is $J_{\min} = 7.2\text{A/mm}^2$. (b) Wire composed by 0.1mmx280 strands. The maximum current density is $J_{\max} = 9.89\text{A/mm}^2$ and the minimum is $J_{\min} = 8.23\text{A/mm}^2$. (c) Wire composed by 0.071mmx630 strands. The maximum current density is $J_{\max} = 7.9\text{A/mm}^2$ and the minimum is $J_{\min} = 7.26\text{A/mm}^2$.

Strand diameter (mm)	Strand number	Outer diameter (mm)	Area (mm^2)
0.071	630	2.6	2.49
0.071	735	2.82	2.91
0.1	280	2.34	2.19
0.1	350	2.62	2.74
0.2	80	2.47	2.51

Table 4.3: Litz wires with different strand diameter and number of strands, that have a total area higher than and close to $2mm^2$.

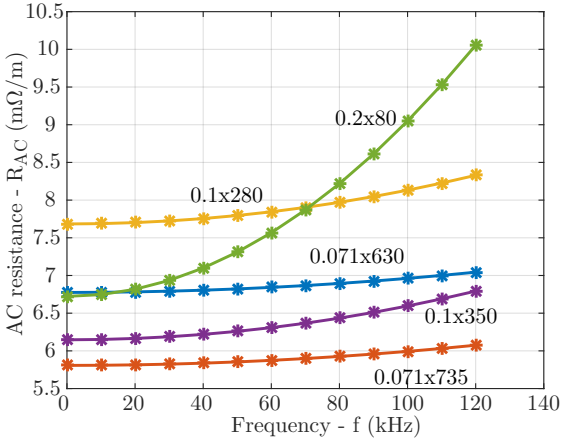

Figure 4.5: AC resistance vs. frequency for the litz wires on Table 4.3.

the receiver part and more solutions are valid. Nevertheless, it must be mentioned that the efficiency will be better with 0.071x735 Litz wire, but as a trade-off the cost will also be higher.

As it can be observed in Figure 4.5, the chosen solution has a very small variation. For this reason, it is fair to say that considering just the DC resistance will be a good approximation.

4.2.4 Tasks preparation

Once the litz wire is selected, all the parametric sweep is prepared. Table 4.4. summarizes the parametric sweep carried out for the 9kW

design and Figure 4.6 is a drawing of one of the receiver coils that is going to be optimized. Each of the parameters that is going to be varied is indicated in indicated in Table 4.4.

Parameter	Symbol	Min.	Max.	Nº of sim.
Percentage of wire space	W_{w}	0.3	0.6	7
Outer width	$W_{\mathrm{R,out}}$	370	420	6
Outer length	$L_{\mathrm{R,out}}$	325	450	6
Ferrite in parallel	$N_{\mathrm{Fe,P}}$	3	5	3
Ferrite in series	$N_{\mathrm{Fe,S}}$	2	3	2
Total number of simulations				1512

Table 4.4: Limits of the parameters that are varied during the optimization sweep.

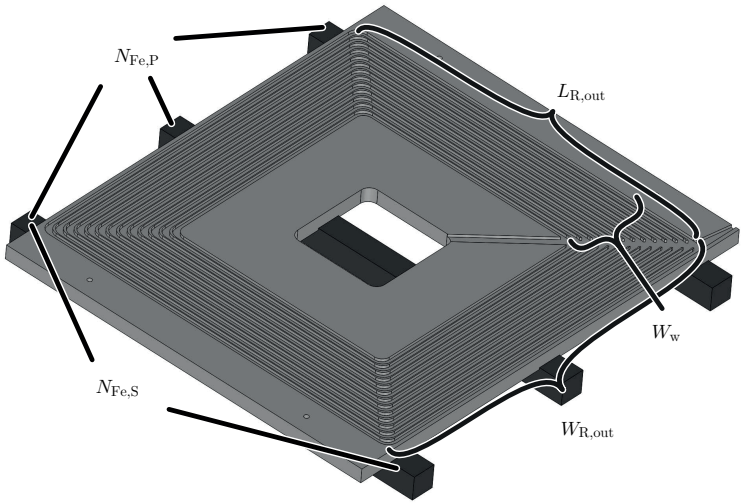

Figure 4.6: Drawing of a receiver coil showing the parameters that are going to be varied during the optimization process.

$L_{\mathrm{R,out}}$ corresponds to the outer length of the receiver (see Figure 4.6). Whereas $W_{\mathrm{R,out}}$ is the outer width. It has to be mentioned, that the moving direction is towards, $L_{\mathrm{R,out}}$. Besides, W_{w}, is the percentage

of wire space. Depending on which is smaller, the length or the width, the value of the wire space will be adjusted according to it. $N_{\mathrm{Fe,P}}$ is the number of ferrite cores placed in parallel. While $N_{\mathrm{Fe,S}}$ is the number of ferrites in series.

It has to be pointed out that many other simulations have been carried out with various transmitter number of turns and different receiver coil sizes. With less transmitter turns (1 or 2 turns) there was not any feasible solution, and the same happened with smaller coils. Besides, with higher turns at the transmitter, there where feasible solutions with higher efficiencies that the ones shown in this document. However, the voltage in the coils got greatly increased, note that the inductance value increases to the square of the number of turns. In addition, the cost will also be higher, as more wire is needed. For that reason, and due to the insulation complications that arise, the minimum feasible transmitter turn was chosen, for the present design three turns. For seek of clarity, only the aforementioned limits are going to be shown in this document and the Pareto-Fronts minimizing V_{L1} are not going to be drawn since they do not give any extra information.

4.2.5 Sweep and Pareto-Fronts

The output of the FEM simulations are: the losses in the ferrites (P_{Fe}), the losses in the aluminum (P_{Al}), the losses in the transmitter (P_{T}) and receiver (P_{R}) coils, the values of the inductances (L_1) and (L_2) and the coupling coefficient (k).

First, for the litz wire losses computation, a DC resistance of 7.9 mΩ/m is used. Even though this value is higher than the one calculated in Figure 4.5, the litz supplier considers it the worst case scenario, taking into account the manufacturing tolerances. Even though it is a conservative approach, it must be point out that extra resistances, like connectors and capacitor soldering are not considered. So taking the worst value, even though in reality the wire resistance is likely to be better, those extra losses will increment the total value.

Besides, the tanδ of the capacitors is set to 2m, according to EPCOS datasheet for capacitors <27nF at 100kHz. The losses in the ferrite cores and aluminum are computed using the materials already predefined in the FEM simulator.

Second, in order to calculate the total weight of the system, a weight of 0.4624kg per single I core plus 0.0278kg per meter for the litz wire is

considered. The transmitter wire weight is not considered, as this part is placed in the ground is not critical. In addition, for the present analysis all the solutions have the same transmitter size, so if considered all the results will have a higher weight but keeping the same difference. The rest of the components, such as the aluminum weight and the plastic fiber coil formers are not computed, since they are also considered equal for all the solutions.

Third, for the computation of the area, only the receiver coil is used. Where a size limit exists. The total area is calculated multiplying the width $W_{\mathrm{R,out}}$ and the length $L_{\mathrm{R,out}}$ of the coil with the number of receivers, for the present optimization, three.

Finally, for the cost computation, each of the ferrite cores cost is estimated to be 7.52€ and the cost of the litz wire is 33.76€/kg. This data, is obtained comparing various ferrite and litz suppliers catalogs.

In the following, the Pareto-Front graphs are analyzed. Figure 4.7, represents the efficiency as a function of the coil area, depending on the coupling coefficient. In Figure 4.10, the receiver voltage is analyzed as a function of this same area. Figure 4.11, depicts again the efficiency but as function of the weight. Finally, in Figure 4.12, the cost of the system is used. Note that for all analyzed solutions, the same output power and the same switching frequency is used.

Efficiency vs. size ($\eta - \mathrm{s_z}$) Pareto-Front

As previously said, the coupling coefficient depends on the area of the coils being faced. This is clearly described in Figure 4.7, where it can be observed that higher coupling coefficient values are obtained with bigger coils.

This entails that with smaller coils, as the same transmitter coil is used for all cases, the secondary needs to have more turns so as to reach the mutual inductance value. With more turns, the losses at the receiver part increase and the efficiency is reduced. So, a Pareto-Front is created between the efficiency and the size of the coils.

It is also noticeable that with the same coil area, many couplings can be obtained and the efficiency can vary drastically. This is due to the ferrite cores that are used for shaping the magnetic field. Figure 4.8 and Figure 4.9, show the same Pareto-Front, but the coloring represents the number of ferrite cores. In Figure 4.8, the solutions with 2 ferrites is highlighted. Whereas in Figure 4.9, 3 ferrites are used.

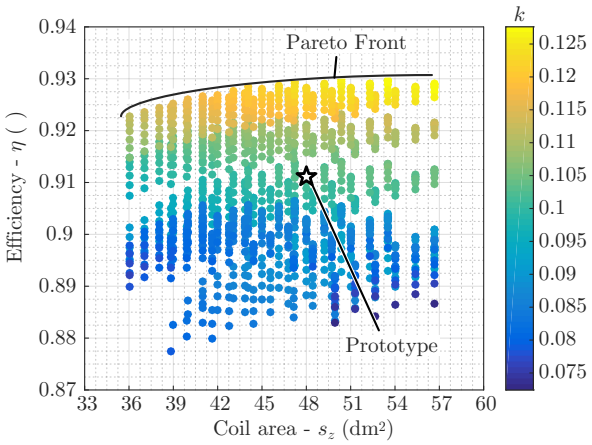

Figure 4.7: Efficiency vs. area Pareto-Front, with the coloring representing the coupling coefficient. The highest efficiency is obtained with the highest coil area.

It can be clearly observed that the most efficient solutions are the ones with the highest number of ferrite cores. Two major effects are produced adding more cores. On the one hand, with more cores there is a better use of the field, i.e. more field reaches the receiver coil. This entails that the coupling is enhanced. On the other hand, apart from the wire loss reduction, the field going through the cores is better distributed, so the losses in the ferrites are also lowered. As a consequence, the efficiency is clearly improved.

Receiver voltage vs. weight ($V_{\mathrm{R}} - \mathrm{w_g}$) Pareto-Front

Another major advantage of increasing the coupling, and as a consequence decreasing the number of turns in the receiver coil, is the reduction of the generated voltage at the coil terminals. Note that in resonance, the voltage generated at the coil and the capacitors is equal. Figure 4.10 represents the secondary coil voltage as a function of the coil area. It can be observed that for the biggest areas with more ferrites, the voltage is greatly reduced.

So, only considering the $\eta - \mathrm{s_z}$ and $V_{\mathrm{R}} - \mathrm{w_g}$ Pareto-Fronts, adding as much ferrite cores as possible is the optimal solution.

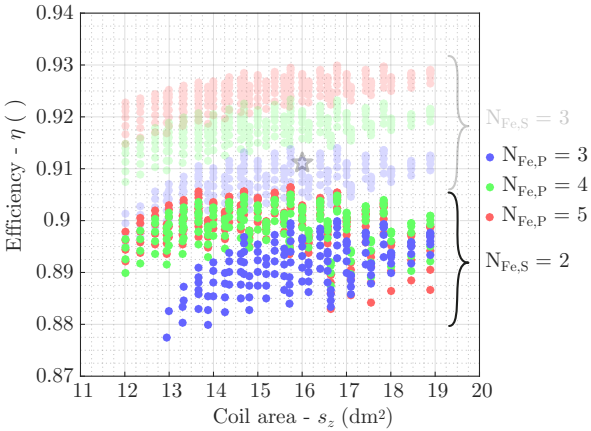

Figure 4.8: Efficiency vs. area Pareto-Front, the coloring represents the number of ferrite cores in parallel, with 2 cores in series is highlighted.

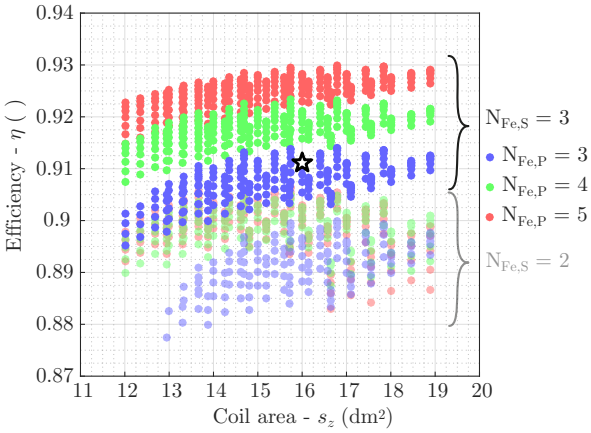

Figure 4.9: Efficiency vs. area Pareto-Front, the coloring represents the number of ferrite cores in parallel, with 3 cores in series is highlighted.

Efficiency vs. weight ($\eta - \mathrm{w_g}$) Pareto-Front

However adding ferrites has also some major drawbacks. Among them, the most remarkable is the weight increase. The most significant weight

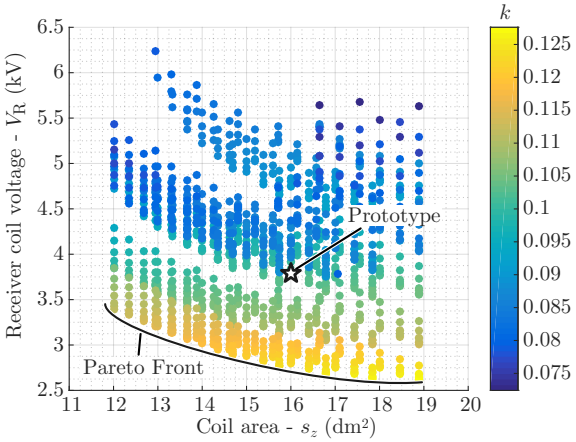

Figure 4.10: Receiver coil voltage vs coil area Pareto-Front. With larger coils, higher coupling is obtained and the voltage of the coil is reduced.

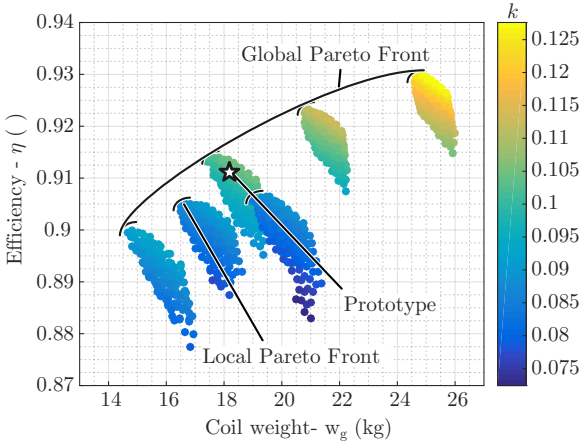

Figure 4.11: Efficiency vs. coil weight. The ferrite cores have a major impact on the total weight of the coils.

contribution to the whole system comes form the ferrite cores. Adding too many cores make the system much heavier, as it can be seen in Figure 4.11. This is the reason why I cores are used and not a solid

ferrite plate. The impact is so clear, that depending on the number of ferrite cores, different solution groups[3] are created. Inside each group a local Pareto Front can be found. For example, if the number of ferrite cores would be predefined, one of this local Pareto-Fronts will be the optimal solution. But analyzing all the solutions, it can be seen that also a global Pareto-Front is created.

Efficiency vs. cost ($\eta-$ €) Pareto-Front

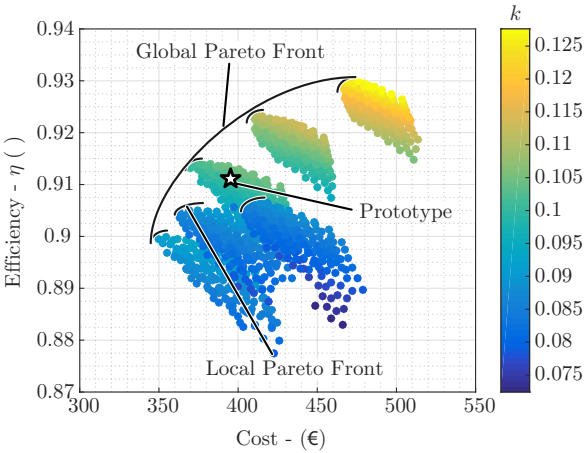

Figure 4.12: Efficiency vs. cost. The cost is computed considering the wire and the ferrite cores. The cost plot is similar to the weight plot. Proportionally, the ferrites are the most expensive part of the system.

Apart from the weight drawback, adding more ferrite cores makes the system more expensive. Figure 4.12, represents the system efficiency vs. the cost. It is very similar to the previous one. In the end, the cost is closely associated to the amount of the material that is being used.

Mind that this is not the cost of the whole system, only the litz wire and the ferrite cores are computed. Comparing the solution with 5 and 3 ferrites, it can be seen that the efficiency is around 2% higher for the 5 core solution, but the cost is around 25% bigger.

[3]The groups are created because the number of cores is discrete. If continuous ferrite sizes where used, there will not be any group division.

Efficiency vs. weighted function equation $(\eta - F)$ Pareto-Front

Summing up, there are two indicators; area and coil voltage, where the highest efficiency is achieved with more ferrite cores. Whereas, the other two; weight and cost, are penalized. In this work there is not any special criteria. So in order to get the optimal solutions a weighting factor $(k_{s_z}, k_{w_g}, k_{€}, k_{V_R})$ is added to those performance indicators $(P_{s_z}, P_{w_g}, P_{€}, P_{V_R})$. In order to have a fair evaluation, each of the performance indicators is divided by its maximum. This way the values are between 0 and 1.

$$F = \frac{k_{s_z} P_{s_z}}{\max\left(P_{s_z}\right)} + \frac{k_{w_g} P_{w_g}}{\max\left(P_{w_g}\right)} + \frac{k_{€} P_{€}}{\max\left(P_{€}\right)} + \frac{k_{V_R} P_{V_R}}{\max\left(P_{V_R}\right)} \tag{4.2}$$

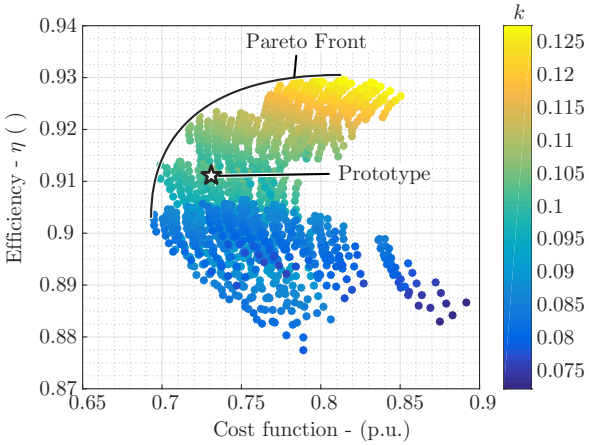

Figure 4.13: Efficiency vs. cost function. The weighting factors are equal for the analyzed four performance indicators. The coloring represents the coupling coefficient.

Figure 4.13, represent the efficiency vs. the aforementioned cost function (4.2). It can be observed that the low coupling solutions are penalized by the large voltage of the coil, whereas the high coupling solutions are penalized by the heavy weight and the high cost. As all performance indicators are equally weighted, 'middle' results arise as optimal solutions.

Finally, the remaining parameter is analyzed, the winding space.

Figure 4.14 also depicts the efficiency over the cost function, but the coloring shows the winding space.

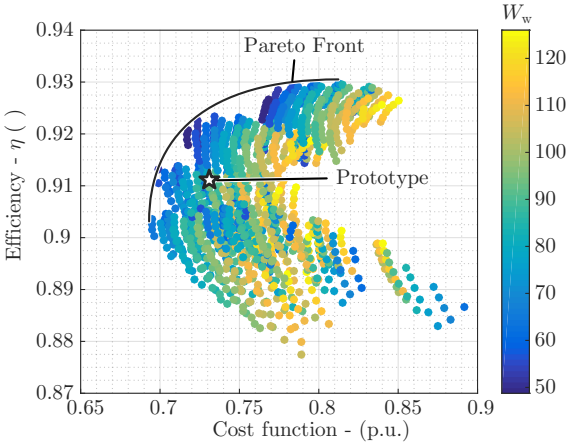

Figure 4.14: Efficiency vs. cost function. The colors represent the wire space in the receiver coils. This value should always be as small as possible.

It can be observed in Figure 4.14 that the available space is not a parameter that creates a trade-off. It serves as a discarding factor, but the optimum solution is always to have the smallest possible space. The intuitive explanation for this phenomenon has already been explained. As previously said, the coupling is higher for larger coil areas. Using smaller winding spaces, note that the space is from the outer part to the inwards, the average turn area is higher. As a consequence the coupling increases and less turns are needed, so efficiency cost and weight is improved. In addition, this winding space does not affect to the total size computation, thus the optimization function is always improved.

4.3 Three-phase Charger

Given the performance indicator trade-offs, a design with the parameters listed in Table 4.5 has been selected. In the previous figures, this design has been indicated by the star point. The constructive limitations (in the plastic fiber coil formers) resulted in the selection of a solution slightly below the Pareto-Front limit.

Parameter	Variable	Value
Transmitter coil		
Length	L_{T}	2800 mm
Width	W_{T}	400 mm
Coil period	λ	800 mm
Number of turns	N_{T}	3
Self inductance	L_{T}	120 μH
Resistance per coil	R_{T}	0.26 Ω
Receiver coil		
Length	L_{R}	400 mm
Width	W_{R}	400 mm
Winding width	W_{w}	80mm
Number of turns	N_{R}	24
Self inductance	L_{R}	346 μH
Resistance per coil	R_{R}	0.54 Ω
Coupling		
Separation	z	100 mm
Peak mutual inductance	$\hat{M}$	22.36 μH
Coupling coefficient	k	0.1
Electric parameters		
Input voltage	$V_{1,\mathrm{DC}}$	520 V
Input peak current	$\hat{i}_{1,\mathrm{AC}}$	18.12 A
Output voltage	$V_{2,\mathrm{DC}}$	600 V
Output peak current	$\hat{i}_{2,\mathrm{AC}}$	15.70 A
Switching frequency	f_{sw}	100kHz
Output power	P_{out}	9 kW
Performance indicators		
Area	s_{z}	16 dm^2
Weight	W_{g}	18.16 kg
Transmitter coil voltage	V_{L1}	1.42 kV
Receiver coil voltage	V_{L2}	3.79 kV
Cost	€	394.95€

Table 4.5: Specifications of the 9kW prototype.

Figure 4.15 represents the power loss distribution for the selected point. It can be observed that the losses are comparatively higher at the receiver coil compared to the transmitter one, 67.44% and 32.56% respectively.

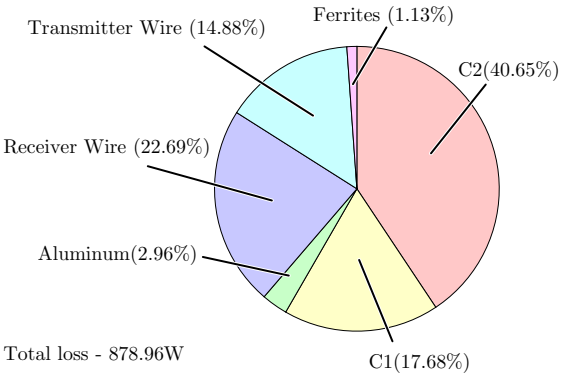

Figure 4.15: Loss distribution in the selected solution. The major losses are produced at the receiver part, specially in the resonance capacitors.

The reason for such disparity lies on the difference between transmitter and receiver inductances. Basically all the 'effort' is carried out at the receiver side. That is to say, since the transmitter has so few turns and the coupling is so low, the receiver needs to have a large amount of turns in order to induce enough voltage. This is directly translated to the loss distribution, mainly in the wire and in the capacitor. In addition, the ferrites and the aluminum are also computed as receiver losses. Among receiver losses, the main contribution comes from the losses at the resonance capacitors. The ESR is comparatively higher to the resistance of the litz wire. In the final assembly, the value of the ESR will depend on the capacitor array (num. in series and num. in parallel). The value of the optimization is obtained with $\tan\delta$ for a single capacitor.

Figure 4.16 depicts the CAD design of the 9kW prototype that has been built and is going to be validated in the following sections.

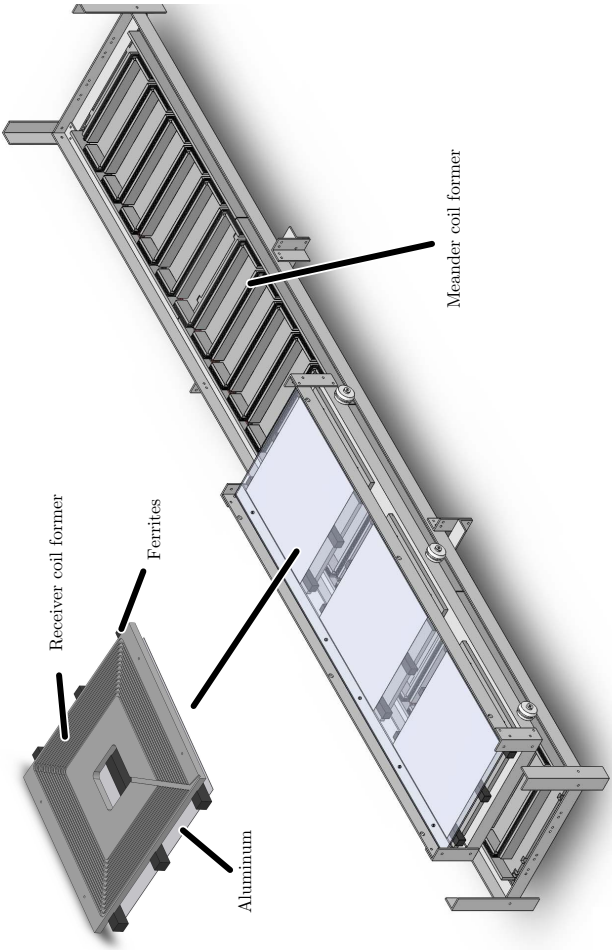

Figure 4.16: 9kW Solidworks design drawing. 3mm separators are added between transmitter turns to prevent from electric arcs.

Once the parameters are optimized, the full system is simulated, i.e the three receivers are analyzed. In this simulation, the three transmitters are located at their final position. This way, the mutual inductance among them can be calculated.

On the one hand, Table 4.6 summarizes the main parameters obtained from FEM simulations. It can be observed that the value of the self inductances is slightly lower than the ones obtained in the optimization process, around 13%. Like in the 50W prototype, this is due to the separation between each turn. Moreover, as a high voltage is expected, the separation between turns has been increased, using 3mm plastic walls. Nevertheless, as it will be shown later, the mutual inductance is not greatly affected.

In addition, the importance of considering the mutual inductance between transmitters is also noticeable. For this prototype the coupling k_{T} is around 0.13. Whereas for the receiver coils, i.e k_{R}, is 0.02 at most.

Simulation

Parameter	Variable	Value
Transmitter self inductance	L_{AA}	104.82 μH
	L_{BB}	104.77 μH
	L_{CC}	104.11 μH
Receiver self inductance	L_{aa}	343.16 μH
	L_{bb}	341.95 μH
	L_{cc}	346.84 μH
Transmitter mutual inductance	M_{AB}	-14.0 μH
	M_{BC}	-18.04 μH
	M_{CA}	-14.7 μH
Receiver mutual inductance	M_{ab}	-8.1 μH
	M_{bc}	-8.06 μH
	M_{ca}	-0.6 μH

Table 4.6: Self and mutual inductances for the 9kW three-phase IPT system.

On the other hand, in Figure 4.17 the mutual inductances $M_{\mathrm{A,a}}$, $M_{\mathrm{B,b}}$ and $M_{\mathrm{C,c}}$ are depicted, for a full geometric period λ. As for the scaled prototype a slight difference appears due to the further distance of the phases A and B. Nevertheless, it can be observed that the obtained values are close to the desired mutual inductance. Phase C has

a +0.6% than the ideal mutual inductance values. Whereas, phase A and phase B are -8.3% and -2.06% respectively.

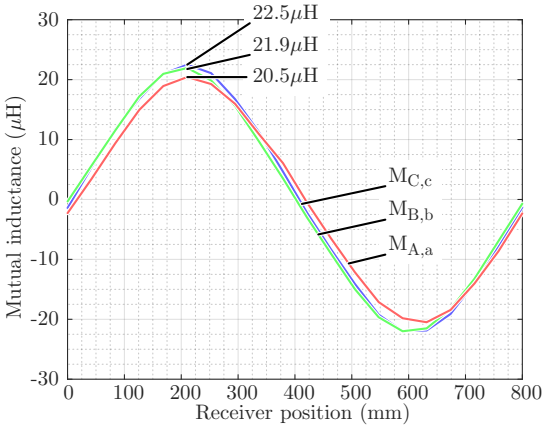

Figure 4.17: Mutual inductances for various receiver positions obtained by FEM simulation.

4.4 Experimental validation

Once the selected solution has been simulated for different positions, the prototype is built to validate the results. Figure 4.18 is a schematic of the assembled test-bench in the laboratory of IK4-IKERLAN.

The power supply is a variable DC source from the laboratory with a maximum voltage of 520V and a rated power of 15kW. Connected to this voltage source, the full-SiC DC/DC converter developed in [Rujas et al., 2014, Rujas et al., 2017] is adapted. Even if the rated power of this converter is 100kW, much higher than the required one, since the objective of this work is to optimize the IPT and not the converter, it is an acceptable option. This converter is comprised of four bridges with 1200V, 100A SiC MOSFETs. For the present work, three of these bridges are used. One of the main challenges of using this converter is the high output capacitance of each device, $C_{\text{oss}} = 2.6185\text{nF}$. The system has to work in a very inductive zone to discharge these capacitances. The control of this inverter is carried out by a sbRio from National Instruments, whose software is also developed. This way the

frequency of the inverter can be changed and adjusted, so the system can be forced to operate in the inductive zone with ZVS. In order to decouple the disturbances, the communication between the control board and the drivers is done via optic fiber.

The output of the inverter is connected to the resonance capacitors. Then one of the ends of each coil is connected to these capacitors, whereas the remaining ends are connected among them, creating the neutral point.

At the secondary part the same coil connections are done. Here the rectification of the AC voltage is going to be carried out with a diode bridge, formed with SiC diodes, plus a small electrolytic capacitor is added to stabilize the DC voltage. Finally, the load will be substituted by an equivalent resistance. As the power is high, for this prototype, the resistors are too big to mount them in the moving part. So they are connected outside and will not move.

In order to measure the transmitted power and the efficiency of the system, a Yokogawa WT500 Precision Power Analyzer is used. With the internal shunt resistors, the input and the output DC currents, i.e. $i_{1,\mathrm{DC}}$ and $i_{2,\mathrm{DC}}$ are measured.

By measuring also the input and output voltages, i.e. $V_{1,\mathrm{DC}}$ and $V_{1,\mathrm{DC}}$, the power at each side is computed and the efficiency is calculated. Note that with this calculations also the transmitter side inverter and the receiver rectifier account for the losses. Even though their efficiency is high, according to [Rujas et al., 2017] over 98%, the measured efficiency is going to be slightly smaller than the one estimated during the optimization routine.

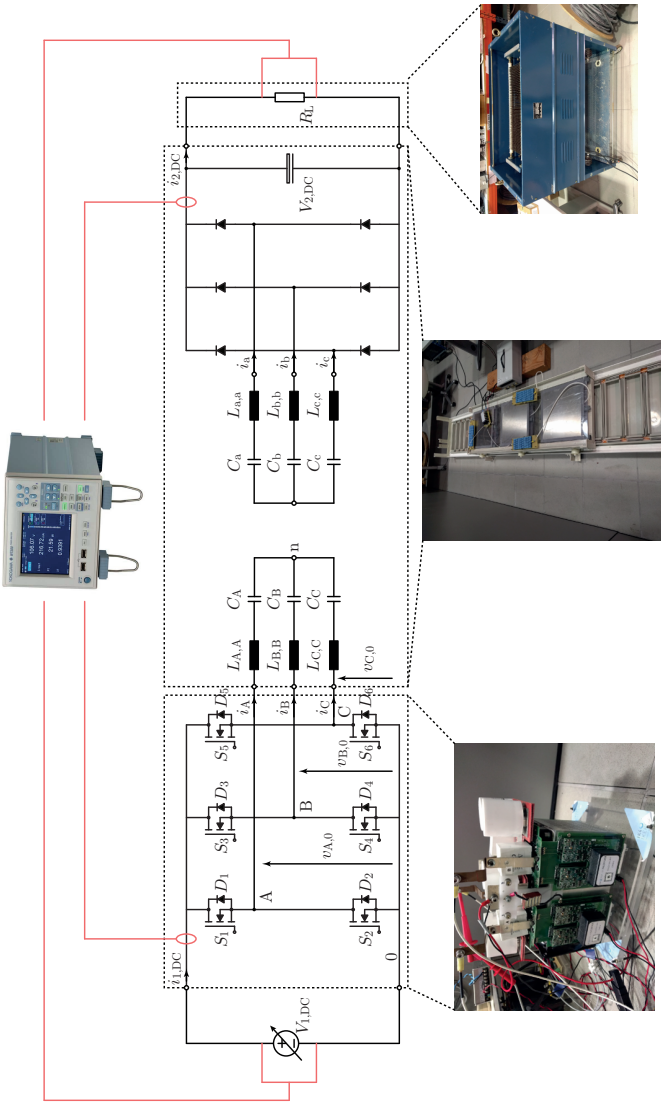

Figure 4.18: Schematic and photos of the 9kW three-phase prototype assembled at the laboratory of IK4-IKERLAN.

4.4.1 Inductance measurements

Before starting with the experiments, first the real inductances are measured. Table 4.7, shows the measured values with the RLC meter and compares them with the simulated values.

Measurements

Parameter	Variable	Value	Diff. sim.
	L_{AA}	95.30 μH	-9.08%
Transmitter self inductance	L_{BB}	93.50 μH	-10.76%
	L_{CC}	95.05 μH	-8.7%
	L_{aa}	355 μH	+3.3%
Receiver self inductance	L_{bb}	353.3 μH	+3.21%
	L_{cc}	354.5 μH	+2.1%
	M_{AB}	-16.83 μH	+20.0%
Transmitter mutual inductance	M_{BC}	-18.1 μH	+0.3%
	M_{CA}	-16.45 μH	+11.9%
	M_{ab}	-5.5 μH	-32.1%
Receiver mutual inductance	M_{bc}	-5.4 μH	-34.24%
	M_{ca}	0.0 μH	-
	R_{AA}	0.29 Ω	+11.54%
Transmitter wire resistance	R_{BB}	0.31 Ω	+19.23%
	R_{CC}	0.3 Ω	+15.38%
	R_{aa}	0.64 Ω	+18.52%
Receiver wire resistance	R_{bb}	0.63 Ω	+16.6%
	R_{cc}	0.61 Ω	+12.9%
Load resistance	$R_{2,DC}$	39 Ω	-2.56%

Table 4.7: 9kW prototype measured inductances and resistances.

From Table 4.7, it can be observed that the simulation accuracy is very high. The biggest differences appear in the mutual inductance among receiver coils, but note that the value is actually very small, around 1.5μH. This differences can come from the manufacturing tolerances or from the measurement itself. The maximum difference appears in the self inductances of the meander coils, approximately 9μH. As a conclusion it can be said that the accuracy is sufficient to validate the simulations.

It has to be pointed out that the load value in order to transmit 9kW at 600V has to be 40Ω. However when measuring the resistance box a value of 39Ω was obtained. For this reason, the real output power is going to be 9.23kW.

Figure 4.19, depicts all the mutual inductance combinations obtained from the FEM simulations (lines) and from the RLC measurements (dots). It can be observed that both methods correspond with each other.

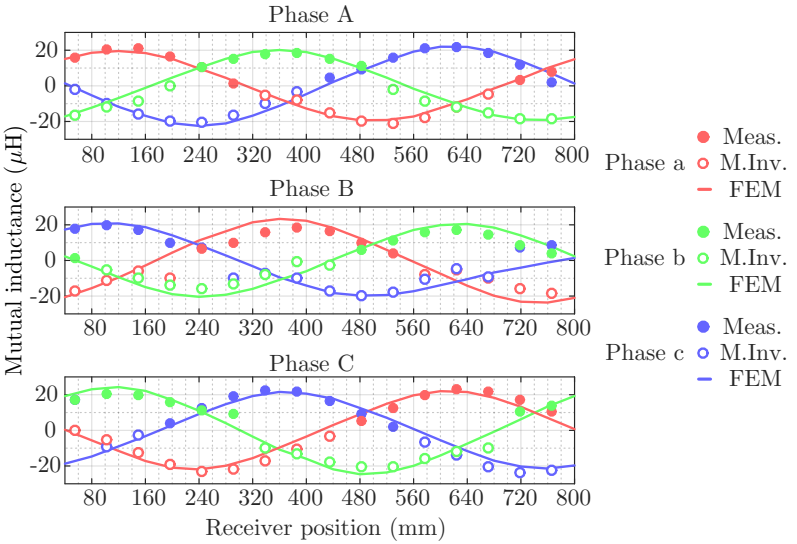

Figure 4.19: Mutual inductance FEM simulations and measurements for the 9kW prototype. The empty circles are measured as positive values as in [Iruretagoyena et al., 2017c]. However, from Figure 3.2 it is known that those values are negative. So, for better visualization, this values have been reflected to the negative part.

However, it has to be mentioned that the measurements are slightly below the FEM simulations. Specially phases A and B. Averaging with the receiver three phases, the mutual inductance is approximately 1.5μH lower than the FEM value shown in Figure 4.17 which corresponds to a mutual inductance 6.5% smaller than the ideal case (phase C is 0.1μH lower than FEM).

Even though according to the carried out DC insulation test the

litz could stand up to 4.5kV, in the initial tests in the prototype an electric-arc was produced. For that reason, an extra insulation paper was added between the phases. This makes phase C to be closer to the receiver coil and have a higher mutual inductance than the rest.

This entails that the current through phase C is likely to be lower than the other two phases. Also the power may have small variations for different receiver positions.

4.4.2 Capacitor calculation

Once all the inductances are known, the total self inductance per phase can be calculated. First of all, for the transmitter coil, the inductances are:

$$\begin{aligned} L_{\mathrm{T,A}} &= L_{\mathrm{A,A}} - M_{\mathrm{A,B}} - M_{\mathrm{A,C}} + M_{\mathrm{B,C}} = 110.48\mu\mathrm{H}, \\ L_{\mathrm{T,B}} &= L_{\mathrm{B,B}} - M_{\mathrm{B,A}} - M_{\mathrm{B,C}} + M_{\mathrm{A,C}} = 111.98\mu\mathrm{H}, \\ L_{\mathrm{T,C}} &= L_{\mathrm{C,C}} - M_{\mathrm{C,A}} - M_{\mathrm{C,B}} + M_{\mathrm{A,B}} = 112.77\mu\mathrm{H}. \end{aligned} \tag{4.3}$$

Whereas for the receiver coil are given by:

$$\begin{aligned} L_{\mathrm{T,a}} &= L_{\mathrm{a,a}} - M_{\mathrm{a,b}} - M_{\mathrm{a,c}} + M_{\mathrm{b,c}} = 355.1\mu\mathrm{H}, \\ L_{\mathrm{T,b}} &= L_{\mathrm{b,b}} - M_{\mathrm{b,a}} - M_{\mathrm{b,c}} + M_{\mathrm{a,c}} = 364.3\mu\mathrm{H}, \\ L_{\mathrm{T,c}} &= L_{\mathrm{c,c}} - M_{\mathrm{c,a}} - M_{\mathrm{c,b}} + M_{\mathrm{a,b}} = 354.4\mu\mathrm{H}. \end{aligned} \tag{4.4}$$

With this inductance values, the resonance capacitance values can be calculated. The transmitter side capacitance values are:

$$\begin{aligned} C_{\mathrm{A}} &= \frac{1}{\omega_0^2 \left(L_{\mathrm{A,A}} - M_{\mathrm{A,B}} - M_{\mathrm{A,C}} + M_{\mathrm{B,C}}\right)} = 22.9\mathrm{nF} \\ C_{\mathrm{B}} &= \frac{1}{\omega_0^2 \left(L_{\mathrm{B,B}} - M_{\mathrm{B,A}} - M_{\mathrm{B,C}} + M_{\mathrm{A,C}}\right)} = 22.6\mathrm{nF} \\ C_{\mathrm{C}} &= \frac{1}{\omega_0^2 \left(L_{\mathrm{C,C}} - M_{\mathrm{C,A}} - M_{\mathrm{C,B}} + M_{\mathrm{A,B}}\right)} = 22.46\mathrm{nF}. \end{aligned} \tag{4.5}$$

While the receiver resonance capacitance values are:

$$
\begin{aligned}
C_{\mathrm{a}} &= \frac{1}{\omega_0^2\left(L_{\mathrm{a,a}} - M_{\mathrm{a,b}} - M_{\mathrm{a,c}} + M_{\mathrm{b,c}}\right)} = 7.13\mathrm{nF} \\
C_{\mathrm{b}} &= \frac{1}{\omega_0^2\left(L_{\mathrm{b,b}} - M_{\mathrm{b,a}} - M_{\mathrm{b,c}} + M_{\mathrm{a,c}}\right)} = 6.95\mathrm{nF} \\
C_{\mathrm{c}} &= \frac{1}{\omega_0^2\left(L_{\mathrm{c,c}} - M_{\mathrm{c,a}} - M_{\mathrm{c,b}} + M_{\mathrm{a,b}}\right)} = 7.14\mathrm{nF}.
\end{aligned} \tag{4.6}
$$

Finally, in order to properly select the capacitors, the voltages must be calculated. The transmitter side capacitor voltages are given by:

$$
\begin{aligned}
\hat{v}_{C_{\mathrm{A}}} &= \frac{1}{\omega_0 C_{\mathrm{A}}}\hat{i}_{\mathrm{A}} = \frac{1}{2\pi 100\mathrm{k}\ 22.9\mathrm{n}}18.12 = 1.259\mathrm{kV} \\
\hat{v}_{C_{\mathrm{B}}} &= \frac{1}{\omega_0 C_{\mathrm{B}}}\hat{i}_{\mathrm{B}} = \frac{1}{2\pi 100\mathrm{k}\ 22.6\mathrm{n}}18.12 = 1.27\mathrm{kV} \\
\hat{v}_{C_{\mathrm{C}}} &= \frac{1}{\omega_0 C_{\mathrm{C}}}\hat{i}_{\mathrm{C}} = \frac{1}{2\pi 100\mathrm{k}\ 22.46\mathrm{n}}18.12 = 1.28\mathrm{kV}
\end{aligned} \tag{4.7}
$$

Whereas the receiver capacitor voltages are:

$$
\begin{aligned}
\hat{v}_{C_{\mathrm{a}}} &= \frac{1}{\omega_0 C_{\mathrm{a}}}\hat{i}_{\mathrm{a}} = \frac{1}{2\pi 100\mathrm{k}\ 7.13\mathrm{n}}15.7 = 3.5\mathrm{kV} \\
\hat{v}_{C_{\mathrm{b}}} &= \frac{1}{\omega_0 C_{\mathrm{b}}}\hat{i}_{\mathrm{b}} = \frac{1}{2\pi 100\mathrm{k}\ 6.95\mathrm{n}}15.7 = 3.59\mathrm{kV} \\
\hat{v}_{C_{\mathrm{c}}} &= \frac{1}{\omega_0 C_{\mathrm{c}}}\hat{i}_{\mathrm{c}} = \frac{1}{2\pi 100\mathrm{k}\ 7.14\mathrm{n}}15.7 = 3.49\mathrm{kV}
\end{aligned} \tag{4.8}
$$

Note that the receiver part voltage is much higher than the transmitter one. Apart from the capacitance, the clearances must be respected in order not to have any electric arc.

In order to select the capacitor array to withstand the maximum voltage, current ratings and reach the expected capacitance values with the least amount of capacitors, the following steps have been followed:

1. Select the single capacitance and voltage rating.

2. Calculate the number of capacitors in series to meet the voltage ratings.

3. Calculate the minimum number of parallel capacitors to meet the current ratings.

4. Add capacitors in parallel until the capacitance value is reached.

It can be seen that the first step is to select the single capacitor value and voltage rating. Many different solutions have been analyzed and the 4.7nF 900V capacitor was the best solution. It is important to know that the voltage rating decreases for higher frequencies. For the present work, at 100kHz, the voltage rating of the capacitor decreases to 600V.

It must be mentioned that getting the exact capacitance value is very complicated. For that reason, a value of 5% higher or lower is considered as a valid solution.

So for the transmitter capacitances, an array of 3 capacitances in series and 15 in parallel have been built. This leads to a total capacitance of 23.5nF with a voltage rating of 1800V and a current rating of 26.57A. Besides, at the receiver part 8 capacitors in series and 12 in parallel are placed. The total value is then 7.05nF, with a voltage rating of 4800V and a current rating of 106.31A.

With these values the following resonance frequencies are obtained:

Resonance frequencies

Phase	Variable	Value
A	$f_{A,0}$	98.77kHz
B	$f_{B,0}$	98.11kHz
C	$f_{C,0}$	97.76kHz
a	$f_{a,0}$	100.59kHz
b	$f_{b,0}$	99.3kHz
c	$f_{c,0}$	100.69kHz

Table 4.8: Resonance frequencies for the 9kW prototype.

4.4.3 Frequency adaptation

In the first experiment the input voltage was set to 200V, which ideally should have been an output power of 1.3kW. Due to the losses and the differences in the mutual inductances, the measured output power

was 1.07kW. In addition, the switching frequency was to close to the resonance, the turn-off current was not high enough and the output capacitance was not fully discharged, see Figure 4.20.

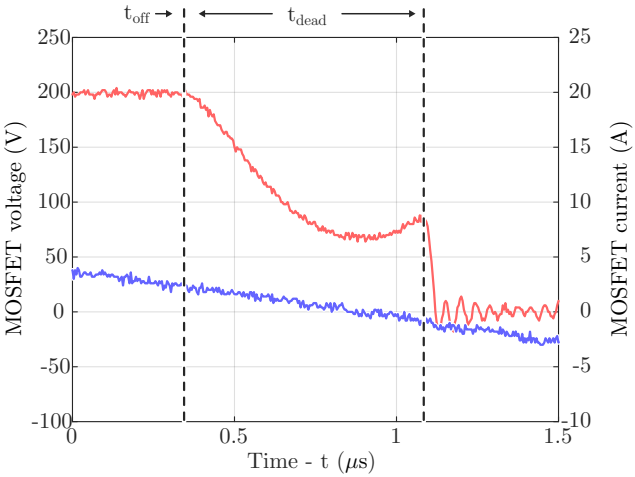

Figure 4.20: Turn-off commutation at 100kHz switching frequency. Even though the system is working in inductive zone, the current is too low to discharge the output capacitance of the MOSFET during the dead time.

It can be seen that even though the current is positive, the value is set around 2.5A and is not high enough to discharge the capacitor before the current sign is changed. In order to solve this problem the system has to be working in a more inductive zone. But it has already been analyzed in this thesis that the inductive zone can be in either higher or lower frequencies. The coupling coefficient must be checked to be lower than the limit. If exceeded the frequency must be reduced, otherwise it has to be increased.

So for the present prototype, k_{lim} is given by:

$$k_{\text{lim}} = \frac{6}{\pi^2} \frac{R_{2,\text{DC}}}{\omega_0 L_{\text{aa}}} = 0.106 \tag{4.9}$$

Whereas the average of the three couplings is

$$k = \frac{M}{\sqrt{L_{\text{T}} L_{\text{R}}}} = 0.105 \tag{4.10}$$

This means that the system is almost exactly at the limit. However the limit calculated in (4.9) corresponds to a system without losses. As explained in [Iruretagoyena et al., 2017a], for the real case due to losses in the wires occur the limit is higher and can be calculated with

$$k_{\text{lim}} = \frac{R_{\text{aa}} + \frac{6}{\pi^2} R_{2,\text{DC}}}{\omega_0 L_{\text{AA}}} = 0.109 \tag{4.11}$$

Working close to the bifurcation zone has another major effect. As it can be observed in 2.20, when the switching frequency is changed the transferred power exhibits to peaks, due to the interaction between the resonant tanks.

This fact is experimentally validated in Figure 4.21, where the output power is show for different switching frequencies. It can be seen that the aforementioned two peaks occur. Apart from achieving ZVS, this can be used as an advantage to adjust the system to actually deliver the designed power.

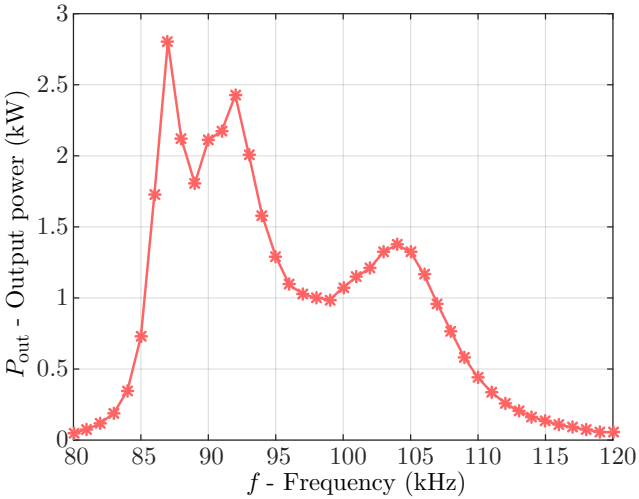

Figure 4.21: Output power vs. switching frequency. To peaks appear since the system is working close to the coupling coefficient limit. Frequencies above resonance (100kHz) are inductive zones and below are capacitive.

So, as a consequence, the working frequency has been changed from 100kHz to 104kHz. Here the desired 1.3kW are obtained at 200V, see

Figure 4.21 and in addition ZVS is achieved, see Figure 4.22. This is due to the fact that the switching current has been increased from 2.5 to 5A. Note that the main drawback is the increased voltage at the capacitors and at the coils. Nevertheless, the voltage rating of the capacitor array that has been built is sufficient.

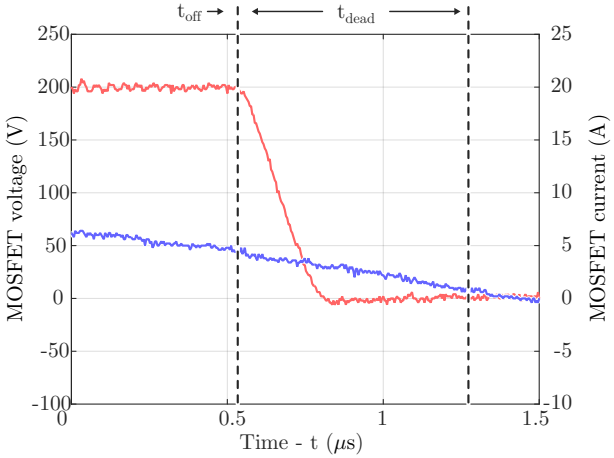

Figure 4.22: Turn-off commutation at 104kHz switching frequency. The system is working in a more inductive zone and the current is high enough to discharge the output capacitance.

Figure 4.23 depicts the efficiency of the system with respect to the switching frequency. As for the 50W prototype, the highest efficiency is achieved at the inductive zone close to the resonance frequency. For this prototype the most efficient frequency is 102kHz. Here the system is inductive enough to discharge the output capacitances. Nevertheless, as explained before, in order to reach the desired output 104kHz are used. At this frequency, the system efficiency is 0.9%, 0.01% lower than the maximum.

4.4.4 Output power and IPT efficiency over input voltage measurements

Figure 4.24 shows the measured output power and the efficiency for different input DC voltages. The desired 9.2kW is obtained for an input

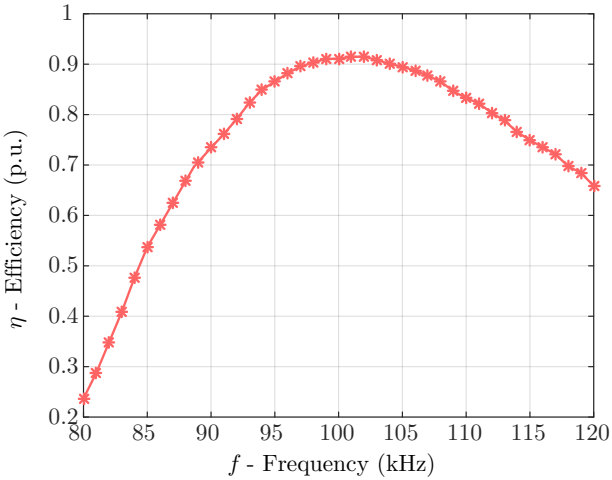

Figure 4.23: DC to DC efficiency vs. switching frequency for the 9kW prototype. The maximum is achieved at 102kHz, the inductive zone capable of discharging the output capacitance with the lowest current.

voltage of 520V. This means that, with a 39Ω resistor, the desired 600V are obtained at the receiver side. Being the load a resistance, as the receiver side voltage is no longer controlled, the output power becomes quadratic to the input voltage [Iruretagoyena et al., 2017b], given by

$$P_{\text{out}} = \frac{4}{\pi^2} \frac{|\text{G}| V_{\text{in}}^2}{\omega \hat{\text{M}}}, \tag{4.12}$$

where |G| is the voltage ratio of the designed point. If a controlled secondary was implemented, and set to a constant value, this output power would be linear to the input voltage as shown in Figure 3.12. This fact is verified in this experiment, where in Figure 4.24 is clearly visible that the power is indeed quadratic to the input voltage.

Besides, it can be observed that the efficiency is almost constant for all the power range. In addition, this value is close to the efficiency estimated in the optimization routine, where an efficiency of 91.1% was calculated. Note that the measured efficiency includes the losses at the inverter and the rectifier and the optimization does not. Nevertheless, it is known from [Rujas et al., 2017] that the efficiency of the inverter is higher than 98%, so the power reduction is minimal. Other causes of

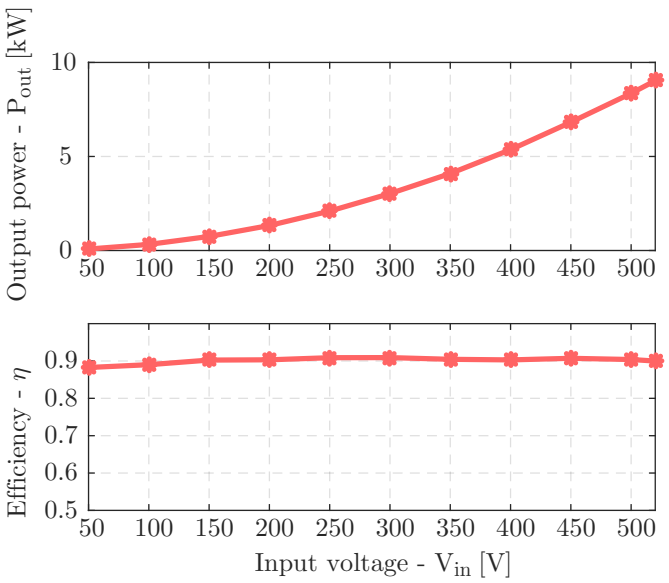

Figure 4.24: Measured output power and efficiency vs. input voltage for the optimized 9kW prototype.

this efficiency reduction are the terminals for the wire connection, and the increment of the switching frequency, that leads to higher losses at the ferrites and the aluminum. However, the accuracy is sufficient to consider the optimization valid, and that the three-phase IPT system a viable solution.

Figure 4.25 depicts the transmitter phase current when the system is delivering 9.2kW. It can be observed that due to the manufacturing tolerances, the currents are not equal. The current trough phase C is lower. As mentioned before in the mutual inductance measurements, the value of M for this phase is higher and this is reflected in the circulating current. However, compared to the ideal value of 18.52A this phase is actually the most proximate. This is another cause of the reduced efficiency compared to the optimization. Phases A and B are carrying more current than the expected one.

Besides, Figure 4.26 shows the voltage and the current of phase C. It can be observed that the system is working in the inductive zone and the output capacitor is correctly discharged during the dead time also

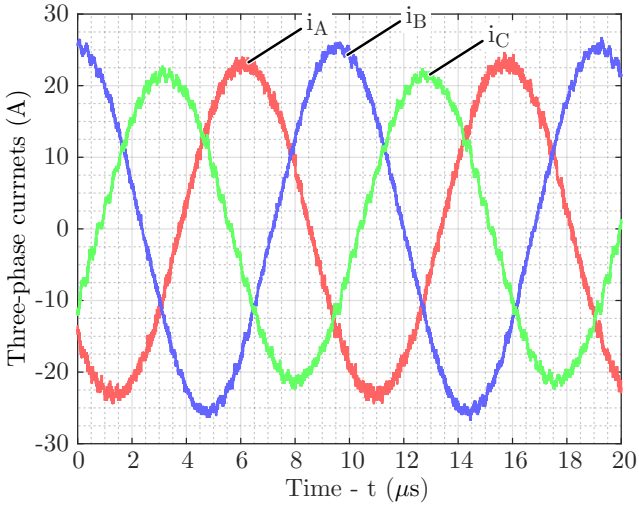

Figure 4.25: Measured transmitter coil currents with the IPT system transmitting 9kW. As the mutual inductance is lower at phase B, the current is slightly higher.

at 9.2kW. In this case, the transition is done with an inductive current of 10A.

It can be observed that, contrarily to the 50W prototype, no voltage spike appears at the square wave signal. This validates that the three currents are actually switching in an inductive zone with enough current to operate at ZVS.

4.4.5 Output power and IPT efficiency over position measurements

Finally, the last experiments consist on validating the power transmission over the charging lane. As previously done for the 50W prototype, the receiver is moved to different positions. In this case the measurements are carried out at 100mm spacings. Figure 4.27 depicts this experiments. A previously anticipated, due to the higher mutual inductance in the C transmitter coil a small power variation appears at x = 200mm and at x = 600mm. This corresponds to the alignment with the coil window C, one at the positive and the other in the negative

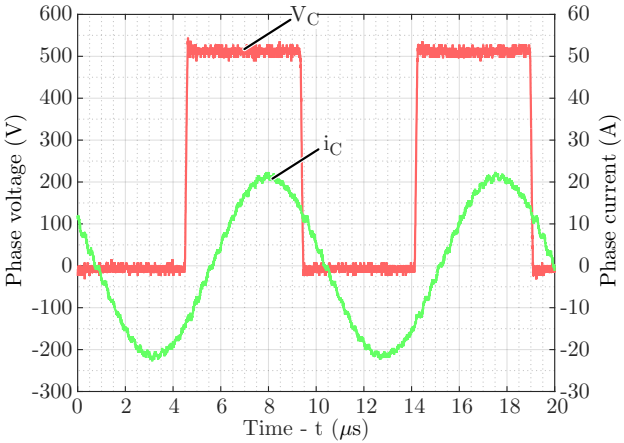

Figure 4.26: Phase C voltage and current. The system is working in a inductive zone to discharge the output capacitances of the MOSFET. This way the efficiency is improved.

part.

Nevertheless, this variation is caused due to manufacturing tolerances that could be solved by using a more restrictive coil former with tighter tolerances, as done in the 50W prototype. Despite this power variation, the efficiency practically has not been affected, it can be observed that the efficiency is approximately 90% for any receiver coil position.

4.5 Conclusions

In this chapter first the different optimization techniques have been summarized, making emphasize in the Pareto-Front optimization. Afterwards, the flow chart for the optimization for three-phase inductive power transfer system has been introduced. The goal of this optimization is to obtain the Pareto-Front for efficiency, weight, coil voltage and cost.

Subsequently, this routine has been applied to an specific case of a 9kW system, oriented to railway transportation. The main conclusion of this optimization is that there are two counteracting performances. Very small coils, with few turns, have a small coil voltage. But as a

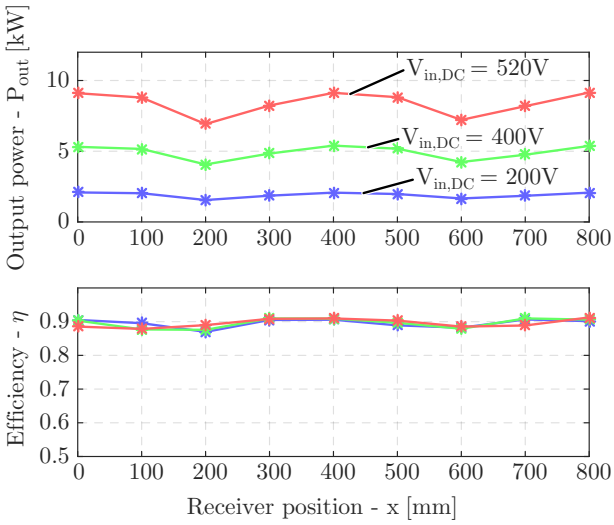

Figure 4.27: Output power and efficiency for various receiver positions for the 9kW prototype, for input voltages, 200V, 400V and 520V.

drawback, they require a large amount of ferrites to reach the mutual inductance value, and therefore, heavy and costly solutions. In the opposite side, large coils do no need many ferrites, but the size is bigger and they require a big amount of turns, so a high voltage is generated. Therefore, a function has been presented with equal weighting factors for the aforementioned performances. Here the optimal solution is to select a 'middle solution'.

Finally, one of these solutions has been selected and experimentally validated. A 90% efficiency has been achieved and the power transmission is practically constant. Even though there are some power oscillations due to the constructive differences between phases.

Chapter 5

Conclusions and Future Work

5.1 Summary and Conclusions

An optimization methodology for three-phase IPT systems employing meander type coils has been presented in this thesis.

For that purpose, first, the basic principles of transformers have been briefly analyzed. In the following step, this theory has been extended to medium frequency application ranges, with the single phase Isolated Conductive Charger. The equations that model the Single Active Bridge have been derived,and a smooth transition to IPT has been done. Here, the differences in the power transmission have been pointed out and the requirement of using compensation topologies has become evident. Afterwards, the series-series and series-parallel compensation topologies have been studied and the modeling equations have been derived. The issues regarding pole-splitting have been detected and experimentally validated. Thus, a new design criteria has been introduced to prevent/avoid the pole-splitting: the inductance ratio limit.

Once the single phase system analyzed, the meander coil principles has been introduced. Thanks to the sinusoidal magnetic field, the potential of achieving constant power transmission has been demonstrated. For that purpose, a multi-phase system is required. In the following, the three-phase IPT system has been analyzed and modeled. Thanks to the derived models, a single phase equivalence has been de-

veloped simplifying the analysis. The previous pole-splitting analysis and design criteria have been extended to this new three-phase system. In addition, with this simplification and design criteria, a new design procedure has been proposed and experimentally validated in a 50W demonstrator. The constant power feature has been satisfactorily demonstrated, with an overall efficiency of 70%.

After the validation, an optimization flow-chart has been introduced. The objective of this optimization has been to obtain the most efficient solution with the smallest, lightest and the cheapest system. As it has been demonstrated, this objective counteract each other and a Pareto-Front has been created. This Pareto-Front has been analyzed for different parameters and a cost function has been introduced using some weighting factors. The optimization procedure has been used for the design of a 9kW system. Finally, this system has been experimentally validated. Once again, constant power transmission has been obtained, in this case with an efficiency of 90%.

5.2 Contributions

The main contributions of this thesis are:

- **Demonstration of the potential of meander type coils for inductive power transmission in railway applications** .

  Inductive power transmission can be one of the technologies that could be used in near future to supply public transportation systems. Specially, railway transportation seems to be the most promising application. Being the catenary and the pantograph the most vulnerable and damaged parts, with the use of IPT, this components could be fully removed. Thus, the power could be transmitted from a coil buried beneath the ground to another receiver coil mounted in the floor of the vehicle.

  One of the main challenges of dynamic IPT is the power variation with the position of the receiver and the complex control that it requires. In this work, it has been demonstrated that using meander type coils, constant power transmission can be achieved. This way, the control is considerably simplified and minor communication is required.

- **Proposal of a new design criteria to prevent from pole-splitting.**

  One of the biggest problems in IPT systems is the pole-splitting or bifurcation. This effect is generated due to the interaction between transmitter side and receiver side resonant tanks. It is a major problem since zero voltage switching is desired. This is typically achieved by increasing the switching frequency slightly above the resonant one. However, if the system has bifurcation, this will lead to a capacitive zone, further increasing the losses.

  In the literature, the limit of pole-splitting is analyzed calculating the maximum coupling coefficient or maximum power. In this work a different approach has been analyzed. The importance of the self inductance ratio has been highlighted. As shown, any IPT system can be free of pole-splitting if the proposed inductance ratio limit is respected.

- **Development of the three-phase to the single phase IPT equivalence equations.**

  It has been demonstrated that the minimum number of transmitter phases has to be three in order to create the traveling wave, and as a consequence, to achieve constant power transmission. Also, the fact that three receivers are necessary to get a balanced system has been pointed out. However, this means that a six coil system is necessary, with the consequent large coil combinations.

  In this work, the equivalent equations that relate the three-phase system with the single-phase IPT system have been developed. This enables the simplification to a single mutual inductance value that is capable of modeling the behavior of the entire system.

- **Proposal of a design procedure for a three-phase railway IPT power supply with fixed voltage.**

  Thanks to the previous two contributions, a design procedure to calculate the different components of the three-phase IPT system has been proposed. First, with the initial voltage and power and the geometric specifications, the required mutual inductance inductance and the coupling coefficient are calculated. Afterwards, with this coupling value and the self inductance limit, the value of inductance of each coil is calculated. Finally, knowing the inductances and the resonance frequency, the resonance capacitors are

calculated taking special care with the voltage rating. Working in such a high frequency creates a very high voltage at the inductor and capacitor ends.

- **Proposal of an optimization methodology for a three-phase railway IPT power supply based on cost functions.**

  Based on the previous design procedure, a design methodology and its flow chart has been proposed. Different aspects like coil width, coil length, wire space and number of ferrites have been analyzed in order to achieve the most efficient solution. In order to make the selection, performance indicators such as size, weight, coil voltage and cost have been considered. It has been demonstrated that a trade-off exists between theses indicators. Smaller coils tend to be heavier and more expensive. Besides with low cost, the coils are typically big and with a large voltage, with the consequent insulation problems.

  In order to select the best solution, a function has been introduced applying weighting factors to the aforementioned performance indicators. In this work since all indicators were set to an equal value, the 'middle' solution stands out as optimal.

- **Implementation and experimental validation of a three-phase IPT system with meander coil.**

  A 9kW optimized three-phase IPT system has been developed, implemented and tested in simulation and validated experimentally. The correlation between the simulation tests and the experimental results validate the modeling of the IPT system. In addition, the solution has a DC/DC efficiency of 90%, lower but proximate to other conductive and static IPT systems. This shows the technological viability of meander type coils for future railway transportation systems.

5.3 Future Work

Within this thesis, a three-phase inductive power transfer system has been modeled, designed and also validated. However, there are still some modeling issues that could be added to the proposed design. In the following paragraphs some of these issues are listed:

- Train floor simulation. The chassis of almost all vehicles are made of metallic materials. Using meander type coils, in the parts where there is not a receiver coil the magnetic field seen by the chassis is worth to be considered. This field will generate Eddy currents, and as a consequence the efficiency of the system will decrease.
- Magnetic field exposure. The ICNIRP sets a maximum human exposure to the magnetic field. It would be interesting to add a design step where the field is calculated and afterwards verify if the limits are respected.
- Thermal model. The heating analysis of the materials could also be added to the design process. As addressed in [Mühlethaler, 2012], the models that determine the thermal resistance of litz wire are still not developed.
- High frequency voltage insulation. During this thesis, DC insulation tests have been carried out. For the used litz wire the maximum voltage was been measured to be 4.5kV. However, in the first experimental test, even though the voltage was much lower <2.5kV, a voltage-arc occurs. This means that the insulation decreases with the frequency. It would be interesting to analyze how the increased frequency reduces the insulation, specially in litz wires.

List of Figures

List of Tables

Bibliography

[Badstuebner et al., 2011] Badstuebner, U., Biela, J., Christen, D., and Kolar, J. W. (2011). Optimization of a 5-kW Telecom Phase-Shift DC/DC Converter With Magnetically Integrated Current Doubler. *IEEE Transactions on Industrial Electronics*, 58(10):4736–4745.

[Bolger et al., 1978] Bolger, J., Rsten, F., and Ng, L. (1978). Inductive power coupling for an electric highway system. In *Vehicular Technology Conference, 1978. 28th IEEE*, volume 28, pages 137–144. IEEE.

[Bombardier, 2010] Bombardier (2010). Primove contactless and catenary-free operation. *EcoActive Technologies*.

[Bosshard, 2015] Bosshard, R. (2015). *Multi-Objective Optimization of Inductive Power Transfer Systems for EV Charging*. PhD thesis, ETH Zurich.

[Bosshard et al., 2016] Bosshard, R., Iruretagoyena, U., and Kolar, J. W. (2016). Comprehensive evaluation of rectangular and double-d coil geometry for 50 kw/85 khz ipt system. *IEEE Journal of Emerging and Selected Topics in Power Electronics*, 4(4):1406–1415.

[Bosshard and Kolar, 2016a] Bosshard, R. and Kolar, J. W. (2016a). All-sic 9.5 kw/dm3 on-board power electronics for 50 kw/85 khz automotive ipt system. *IEEE Journal of Emerging and Selected Topics in Power Electronics*, PP(99):1–1.

[Bosshard and Kolar, 2016b] Bosshard, R. and Kolar, J. W. (2016b). Multi-objective optimization of 50 kw/85 khz ipt system for public transport. *IEEE Journal of Emerging and Selected Topics in Power Electronics*, 4(4):1370–1382.

[Bosshard et al., 2015] Bosshard, R., Kolar, J. W., Mühlethaler, J., Stevanovic, I., Wunsch, B., and Canales, F. (2015). Modeling and η - α - pareto optimization of inductive power transfer coils for electric vehicles. *IEEE Journal of Emerging and Selected Topics in Power Electronics*, 3(1):50–64.

[Budhia et al., 2013] Budhia, M., Boys, J. T., Covic, G. A., and Huang, C.-Y. (2013). Development of a single-sided flux magnetic coupler for electric vehicle ipt charging systems. *Industrial Electronics, IEEE Transactions on*, 60(1):318–328.

[Budhia et al., 2011a] Budhia, M., Covic, G. A., and Boys, J. T. (2011a). Design and optimization of circular magnetic structures for lumped inductive power transfer systems. *IEEE Transactions on Power Electronics*, 26(11):3096–3108.

[Budhia et al., 2011b] Budhia, M., Covic, G. A., Boys, J. T., and Huang, C.-Y. (2011b). Development and evaluation of single sided flux couplers for contactless electric vehicle charging. In *Energy Conversion Congress and Exposition (ECCE), 2011 IEEE*, pages 614–621. IEEE.

[Burkart and Kolar, 2017] Burkart, R. M. and Kolar, J. W. (2017). Comparative life cycle cost analysis of si and sic pv converter systems based on advanced *eta- rho-sigma* multiobjective optimization techniques. *IEEE Transactions on Power Electronics*, 32(6):4344–4358.

[Cai and Siek, 2017] Cai, A. Q. and Siek, L. (2017). A 2-kw, 95 % efficiency inductive power transfer system using gallium nitride gate injection transistors. *IEEE Journal of Emerging and Selected Topics in Power Electronics*, 5(1):458–468.

[Chéron, 1992] Chéron, Y. (1992). Soft commutation. In *Soft Commutation*, pages 45–59. Springer.

[Chigira et al., 2011] Chigira, M., Nagatsuka, Y., Kaneko, Y., Abe, S., Yasuda, T., and Suzuki, A. (2011). Small-size light-weight transformer with new core structure for contactless electric vehicle power transfer system. In *2011 IEEE Energy Conversion Congress and Exposition*, pages 260–266.

[Chinthavali et al., 2013] Chinthavali, M. S., Onar, O. C., Miller, J. M., and Tang, L. (2013). Single-phase active boost rectifier with power factor correction for wireless power transfer applications. In *2013 IEEE Energy Conversion Congress and Exposition*, pages 3258–3265.

[Choi et al., 2013] Choi, S.-M., Huh, J., Lee, W. Y., Lee, S., and Rim, C. T. (2013). New cross-segmented power supply rails for roadway-powered electric vehicles. *Power Electronics, IEEE Transactions on*, 28(12):5832–5841.

[Choi et al., 2015] Choi, S. Y., Jeong, S. Y., Gu, B. W., Lim, G. C., and Rim, C. T. (2015). Ultraslim s-type power supply rails for roadway-powered electric vehicles. *Power Electronics, IEEE Transactions on*, 30(11):6456–6468.

[Conductix Wampfler, 2012] Conductix Wampfler (2012). 10 years of electric buses with ipt charge. Available: http://www.conductix.com/en/news/2012-05-31/10-years-electric-buses-iptr-charge [Accessed: Apr. 28, 2017].

[Covic and Boys, 2013] Covic, G. A. and Boys, J. T. (2013). Modern trends in inductive power transfer for transportation applications. *Emerging and Selected Topics in Power Electronics, IEEE Journal of*, 1(1):28–41.

[Dai and Ludois, 2015] Dai, J. and Ludois, D. C. (2015). A survey of wireless power transfer and a critical comparison of inductive and capacitive coupling for small gap applications. *IEEE Transactions on Power Electronics*, 30(11):6017–6029.

[Desire et al., 2015] Desire, B., Boedt, S., and Lischke, S. (2015). Inductive pick-up arrangement for an electric vehicle and method of operating an electric vehicle. US Patent App. 14/400,109.

[Dubey and Santoso, 2015] Dubey, A. and Santoso, S. (2015). Electric vehicle charging on residential distribution systems: Impacts and mitigations. *IEEE Access*, 3:1871–1893.

[Dujic and Mogorovic, 2017] Dujic, D. and Mogorovic, M. (2017). High Power Medium Frequency Transformer Design Optimization. TUTORIAL at EPE'17 ECCE Europe, European Conference on Power

Electronics and Applications, Warsaw, Poland, September, 11-15, 2017.

[Dusmez et al., 2011] Dusmez, S., Cook, A., and Khaligh, A. (2011). Comprehensive analysis of high quality power converters for level 3 off-board chargers. In *2011 IEEE Vehicle Power and Propulsion Conference*, pages 1–10.

[Eghtesadi, 1990] Eghtesadi, M. (1990). Inductive power transfer to an electric vehicle-analytical model. In *Vehicular Technology Conference, 1990 IEEE 40th*, pages 100–104. IEEE.

[Elliott et al., 1995] Elliott, G., Boys, J., and Green, A. (1995). Magnetically coupled systems for power transfer to electric vehicles. In *Power Electronics and Drive Systems, 1995., Proceedings of 1995 International Conference on*, pages 797–801. IEEE.

[Esser, 1995] Esser, A. (1995). Contactless charging and communication for electric vehicles. *Industry Applications Magazine, IEEE*, 1(6):4–11.

[Ferreira, 1992] Ferreira, J. (1992). Analytical computation of ac resistance of round and rectangular litz wire windings. In *IEE Proceedings B (Electric Power Applications)*, volume 139. IET.

[Flankl et al., 2017] Flankl, M., Tüysüz, A., and Kolar, J. W. (2017). Cogging torque shape optimization of an integrated generator for electromechanical energy harvesting. *IEEE Transactions on Industrial Electronics*, 64(12):9806–9814.

[Gao, 2007] Gao, J. (2007). Traveling magnetic field for homogeneous wireless power transmission. *Power Delivery, IEEE Transactions on*, 22(1):507–514.

[Garcia Bediaga, 2014] Garcia Bediaga, A. (2014). *Optimal Design of Medium Frequency High Power Converters*. PhD thesis, STI, Lausanne.

[Gati et al., 2017] Gati, E., Kampitsis, G., and Manias, S. (2017). Variable frequency controller for inductive power transfer in dynamic conditions. *IEEE Transactions on Power Electronics*, 32(2):1684–1696.

[Global EV outlook, 2016] Global EV outlook (2016). Beyond one million electric cars. Available: www.iea.org/publications/freepublications/publication/Global_EV_Outlook_2016.pdf [Accessed: Apr. 24, 2017].

[Gonzalez-Hernando et al., 2017] Gonzalez-Hernando, F., Iruretagoyena, U., Arias, M., and Villar, I. (2017). Dynamic ipt system with lumped coils for railway application. In *2017 19th European Conference on Power Electronics and Applications (EPE'17 ECCE Europe)*, pages P.1–P.9.

[Herrera et al., 2016] Herrera, V., Milo, A., Gaztañaga, H., Etxeberria-Otadui, I., Villarreal, I., and Camblong, H. (2016). Adaptive energy management strategy and optimal sizing applied on a battery-supercapacitor based tramway. *Applied Energy*, 169:831–845.

[Herrera et al., 2015] Herrera, V. I., Gaztanaga, H., Milo, A., Saez-de Ibarra, A., Etxeberria-Otadui, I., and Nieva, T. (2015). Optimal energy management of a battery-supercapacitor based light rail vehicle using genetic algorithms. In *Energy Conversion Congress and Exposition (ECCE), 2015 IEEE*, pages 1359–1366. IEEE.

[Huang et al., 2015] Huang, L., Li, Y., He, Z., Gao, S., and Yu, J. (2015). Improved robust controller design for dynamic ipt system under mutual-inductance uncertainty. In *2015 IEEE PELS Workshop on Emerging Technologies: Wireless Power (2015 WoW)*, pages 1–6.

[Huber, 2016] Huber, J. E. (2016). *Conceptualization and Multi-Objective Analysis of Multi-Cell Solid-State Transformers*. PhD thesis, ETH Zurich.

[Huh et al., 2010] Huh, J., Lee, S., Park, C., Cho, G.-H., and Rim, C.-T. (2010). High performance inductive power transfer system with narrow rail width for on-line electric vehicles. In *Energy Conversion Congress and Exposition (ECCE), 2010 IEEE*, pages 647–651. IEEE.

[Huh et al., 2011] Huh, J., Lee, S. W., Lee, W. Y., Cho, G. H., and Rim, C. T. (2011). Narrow-width inductive power transfer system for online electrical vehicles. *Power Electronics, IEEE Transactions on*, 26(12):3666–3679.

[IRENA, 2017] IRENA (2017). Electric vehicles: technology brief. Inernational Renewable Energy Agency, Abu Dabhi. Available: http://www.irena.org/DocumentDownloads/Publications/IRENA_Electric_Vehicles_2017.pdf [Accessed: Apr. 24, 2017].

[Iruretagoyena et al., 2017a] Iruretagoyena, U., Garcia-Bediaga, A., Mir, L., Camblong, H., and Villar, I. (2017a). Bifurcation phenomenon limits for three phase ipt systems with constant coupling coefficient. In *Energy Conversion Congress and Exposition (ECCE), 2017 IEEE*. IEEE.

[Iruretagoyena et al., 2017b] Iruretagoyena, U., Garcia-Bediaga, A., Rujas, A., Camblong, H., and Villar, I. (2017b). Operation boundaries of single/three phase inductive power transfer systems with series-series compensation. In *2017 19th European Conference on Power Electronics and Applications (EPE'17 ECCE Europe)*, pages P.1–P.9.

[Iruretagoyena et al., 2017c] Iruretagoyena, U., Villar, I., Garcia-Bediaga, A., Mir, L., and Camblong, H. (2017c). Design and characterization of a meander type dynamic inductively coupled power transfer coil. *IEEE Transactions on Industry Applications*, PP(99):1–1.

[Kasper et al., 2016] Kasper, M., Burkart, R. M., Deboy, G., and Kolar, J. W. (2016). Zvs of power mosfets revisited. *IEEE Transactions on Power Electronics*, 31(12):8063–8067.

[Khaligh and Dusmez, 2012] Khaligh, A. and Dusmez, S. (2012). Comprehensive topological analysis of conductive and inductive charging solutions for plug-in electric vehicles. *IEEE Transactions on Vehicular Technology*, 61(8):3475–3489.

[Knecht and Kolar, 2017] Knecht, O. and Kolar, J. W. (2017). Comparative evaluation of ipt resonant circuit topologies for wireless power supplies of implantable mechanical circulatory support systems. In *Applied Power Electronics Conference and Exposition (APEC), 2017 IEEE*, pages 3271–3278. IEEE.

[Kolar et al., 2010] Kolar, J. W., Biela, J., Waffler, S., Friedli, T., and Badstuebner, U. (2010). Performance trends and limitations of power electronic systems. In *2010 6th International Conference on Integrated Power Electronics Systems*, pages 1–20.

[Kolar et al., 2007] Kolar, J. W., Drofenik, U., Biela, J., Heldwein, M. L., Ertl, H., Friedli, T., and Round, S. D. (2007). Pwm converter power density barriers. In *2007 Power Conversion Conference - Nagoya*, pages P–9–P–29.

[Lammeraner and Štafl, 1966] Lammeraner, J. and Štafl, M. (1966). *Eddy currents*. CRC Press.

[Lee et al., 2014] Lee, K., Pantic, Z., and Lukic, S. M. (2014). Reflexive field containment in dynamic inductive power transfer systems. *Power Electronics, IEEE Transactions on*, 29(9):4592–4602.

[Lin et al., 2010] Lin, J., Saunders, R., Schulmeister, K., Söderberg, P., Swerdlow, A., Taki, M., Veyret, B., Ziegelberger, G., Repacholi, M. H., Matthes, R., et al. (2010). Icnirp guidelines for limiting exposure to time-varying electric and magnetic fields (1 hz to 100 khz). *Health Physics*, 99:818–836.

[Liu et al., 2016] Liu, H., Huang, X., Tan, L., Guo, J., and Wang, W. (2016). Switching control optimisation strategy of segmented transmitting coils for on-road charging of electrical vehicles. *IET Power Electronics*, 9(11):2282–2288.

[Lukic and Pantic, 2013] Lukic, S. and Pantic, Z. (2013). Cutting the cord: Static and dynamic inductive wireless charging of electric vehicles. *Electrification Magazine, IEEE*, 1(1):57–64.

[Meins and Struve, 2013] Meins, J. and Struve, C. (2013). Transferring electric energy to a vehicle. US Patent 8,590,682.

[Meins and Vollenwyder, 2013] Meins, J. and Vollenwyder, K. (2013). System and method for transferring electric energy to a vehicle. US Patent 8,360,216.

[Mühlethaler, 2012] Mühlethaler, J. (2012). *Modeling and multi-objective optimization of inductive power components*. PhD thesis, ETH Zurich. Diss., Eidgenössische Technische Hochschule ETH Zürich, Nr. 20217, 2012.

[Mir et al., 2009] Mir, L., Etxeberria-Otadui, I., Arenaza, D., Perez, I., Sarasola, I., and Nieva, T. (2009). A supercapacitor based light rail vehicle: system design and operations modes. In *Energy Conversion*

Congress and Exposition, 2009. ECCE 2009. IEEE, pages 1632–1639. IEEE.

[Mogorovic and Dujic, 2017] Mogorovic, M. and Dujic, D. (2017). Medium frequency transformer design and optimization. In *PCIM Europe 2017; International Exhibition and Conference for Power Electronics, Intelligent Motion, Renewable Energy and Energy Management*, pages 1–8.

[Nagatsuka et al., 2010] Nagatsuka, Y., Ehara, N., Kaneko, Y., Abe, S., and Yasuda, T. (2010). Compact contactless power transfer system for electric vehicles. In *The 2010 International Power Electronics Conference - ECCE ASIA -*, pages 807–813.

[Nagendra et al., 2017] Nagendra, G. R., Covic, G. A., and Boys, J. T. (2017). Sizing of inductive power pads for dynamic charging of evs on ipt highways. *IEEE Transactions on Transportation Electrification*, 3(2):405–417.

[Ning et al., 2013] Ning, P., Onar, O., and Miller, J. (2013). Genetic algorithm based coil system optimization for wireless power charging of electric vehicles. In *2013 IEEE Transportation Electrification Conference and Expo (ITEC)*, pages 1–5.

[Nussbaumer et al., 2009] Nussbaumer, T., Raggl, K., and Kolar, J. W. (2009). Design guidelines for interleaved single-phase boost pfc circuits. *IEEE Transactions on Industrial Electronics*, 56(7):2559–2573.

[Nykvist and Nilsson, 2015] Nykvist, B. and Nilsson, M. (2015). Rapidly falling costs of battery packs for electric vehicles. *Nature Climate Change*, 5(4):329–332.

[Onar et al., 2013a] Onar, O. C., Campbell, S., Ning, P., Miller, J. M., and Liang, Z. (2013a). Fabrication and evaluation of a high performance sic inverter for wireless power transfer applications. In *Wide Bandgap Power Devices and Applications (WiPDA), 2013 IEEE Workshop on*, pages 125–130. IEEE.

[Onar et al., 2013b] Onar, O. C., Miller, J. M., Campbell, S. L., Coomer, C., White, C. P., and Seiber, L. E. (2013b). A novel wireless power transfer for in-motion ev/phev charging. In *2013 Twenty-Eighth Annual IEEE Applied Power Electronics Conference and Exposition (APEC)*, pages 3073–3080.

[Ongayo and Hanif, 2015] Ongayo, D. and Hanif, M. (2015). An overview of single-sided and double-sided winding inductive coupling transformers for wireless electric vehicle charging. In *Future Energy Electronics Conference (IFEEC), 2015 IEEE 2nd International*, pages 1–6. IEEE.

[Ortiz, 2014] Ortiz, G. (2014). *High-power DC-DC converter technologies for smart grid and traction applications*. PhD thesis, ETH ZURICH.

[Panasonic, 2010] Panasonic (2010). Rechargeable li-ion oem battery products. Available: https://na.industrial.panasonic.com/ [Accessed: May. 09, 2017].

[Raggl et al., 2009] Raggl, K., Nussbaumer, T., Doerig, G., Biela, J., and Kolar, J. W. (2009). Comprehensive design and optimization of a high-power-density single-phase boost pfc. *IEEE Transactions on Industrial Electronics*, 56(7):2574–2587.

[Rujas et al., 2014] Rujas, A., Garcia, G., Etxeberria-Otadu, I., Larrañaga, U., and Nieva, T. (2014). Design and experimental validation of a high frequency gate driver for silicon carbide power modules. In *2014 IEEE Energy Conversion Congress and Exposition (ECCE)*, pages 5729–5735.

[Rujas et al., 2017] Rujas, A., López-Martín, V., Mir, L., and Nieva, T. (2017). Gate driver for high power sic modules. design considerations, development and experimental validation. *IET Power Electronics*.

[Safaee et al., 2015] Safaee, A., Woronowicz, K., and Dickson, T. (2015). Reactive power compensation in three phase high output inductive power transfer. In *Electrical Power and Energy Conference (EPEC), 2015 IEEE*, pages 375–380. IEEE.

[Sampath et al., 2016] Sampath, J. P. K., Vilathgamuwa, D. M., and Alphones, A. (2016). Efficiency enhancement for dynamic wireless power transfer system with segmented transmitter array. *IEEE Transactions on Transportation Electrification*, 2(1):76–85.

[San-Sebastian et al., 2013] San-Sebastian, J., Etxeberria-Otadui, I. d., and Barrena Bruña, J. A. d. (2013). *PEBB based medium voltage converter optimized design methodology. Documento científico*

MGEP. Arrasate Mondragon Unibertsitatea. Mondragon Goi Eskola Politeknikoa 2013.

[Sato et al., 1999] Sato, F., Adachi, S., Matsuki, H., and Kikuchi, S. (1999). The optimum design of open magnetic circuit meander coil for contactless power station system. In *Magnetics Conference, 1999. Digest of INTERMAG 99. 1999 IEEE International*, pages GR09–GR09. IEEE.

[Sato et al., 1998] Sato, F., Matsuki, H., Kikuchi, S., Seto, T., Satoh, T., Osada, H., and Seki, K. (1998). A new meander type contactless power transmission system-active excitation with a characteristics of coil shape. *Magnetics, IEEE Transactions on*, 34(4):2069–2071.

[Sato et al., 1996] Sato, F., Murakami, J., Matsuki, H., Kikuchi, S., Harakawa, K., and Satoh, T. (1996). Stable energy transmission to moving loads utilizing new clps. *Magnetics, IEEE Transactions on*, 32(5):5034–5036.

[Steinmetz, 1892] Steinmetz, C. P. (1892). On the law of hysteresis. *Transactions of the American Institute of Electrical Engineers*, 9(1):1–64.

[Subotic et al., 2016] Subotic, I., Gammeter, C., Tüysüz, A., and Kolar, J. W. (2016). Weight optimization of an axial-flux pm machine for airborne wind turbines. In *2016 IEEE International Conference on Power Electronics, Drives and Energy Systems (PEDES)*, pages 1–6.

[Swain et al., 2014] Swain, A. K., Devarakonda, S., and Madawala, U. K. (2014). Modeling, sensitivity analysis, and controller synthesis of multipickup bidirectional inductive power transfer systems. *IEEE Transactions on Industrial Informatics*, 10(2):1372–1380.

[Tejeda et al., 2017] Tejeda, A., Carretero, C., Boys, J. T., and Covic, G. A. (2017). Ferrite-less circular pad with controlled flux cancelation for ev wireless charging. *Power Electronics, IEEE Transactions on*, 32(11):8349—-8359.

[Tesla, 1914] Tesla, N. (1914). Apparatus for transmitting electrical energy. US Patent 1,119,732.

[The Boston Consulting Group, 2009] The Boston Consulting Group (2009). The comeback of the electric car? Available: https://www.bcg.com/documents/file15404.pdf [Accessed: Apr. 25, 2017].

[The Boston Consulting Group, 2010] The Boston Consulting Group (2010). Batteries for electric cars: Challenges, opportunities, and the outloook to 2020. Available: https://www.bcg.com/documents/file36615.pdf [Accessed: Apr. 25, 2017].

[Thrimawithana and Madawala, 2013] Thrimawithana, D. J. and Madawala, U. K. (2013). A generalized steady-state model for bidirectional ipt systems. *Power Electronics, IEEE Transactions on*, 28(10):4681–4689.

[Turki et al., 2015] Turki, F., Staudt, V., and Steimel, A. (2015). Dynamic wireless ev charging fed from railway grid: Magnetic topology comparison. In *2015 International Conference on Electrical Systems for Aircraft, Railway, Ship Propulsion and Road Vehicles (ESARS)*, pages 1–8.

[Van Schuylenbergh and Puers, 2009] Van Schuylenbergh, K. and Puers, R. (2009). *Inductive powering: basic theory and application to biomedical systems*. Springer Science & Business Media.

[Vandevoorde and Puers, 2001] Vandevoorde, G. and Puers, R. (2001). Wireless energy transfer for stand-alone systems: a comparison between low and high power applicability. *Sensors and Actuators A: Physical*, 92(1):305–311.

[Villa et al., 2012] Villa, J. L., Sallan, J., Osorio, J. F. S., and Llombart, A. (2012). High-misalignment tolerant compensation topology for icpt systems. *Industrial Electronics, IEEE Transactions on*, 59(2):945–951.

[Villar, 2010] Villar, I. (2010). *Multiphysical Characterization of Medium-Frequency Power Electronic Transformers*. PhD thesis, STI, Lausanne.

[Villar et al., 2015] Villar, I., Iruretagoyena, U., Rujas, A., Garcia-Bediaga, A., and de Arenaza, I. P. (2015). Design and implementation of a sic based contactless battery charger for electric vehicles. In *2015 IEEE Energy Conversion Congress and Exposition (ECCE)*, pages 1294–1300.

[Vollenwyder et al., 2014] Vollenwyder, K., Meins, J., and Struve, C. (2014). Inductively receiving electric energy for a vehicle. US Patent 8,827,058.

[Wakiwaka et al., 1996a] Wakiwaka, H., Nishizawa, M., Yanase, S., and Maehara, O. (1996a). Analysis of impedance characteristics of meander coil. *Magnetics, IEEE Transactions on*, 32(5):4332–4334.

[Wakiwaka et al., 1996b] Wakiwaka, H., Yanase, S., and Nihizawa, M. (1996b). Characteristics of meander coil impedance with opened scale coil for linear sensor. In *Industrial Electronics, Control, and Instrumentation, 1996., Proceedings of the 1996 IEEE IECON 22nd International Conference on*, volume 1, pages 487–492. IEEE.

[Wang et al., 2004] Wang, C.-S., Covic, G. A., and Stielau, O. H. (2004). Power transfer capability and bifurcation phenomena of loosely coupled inductive power transfer systems. *Industrial Electronics, IEEE Transactions on*, 51(1):148–157.

[Wang et al., 2005] Wang, C.-S., Stielau, O. H., and Covic, G. A. (2005). Design considerations for a contactless electric vehicle battery charger. *Industrial Electronics, IEEE Transactions on*, 52(5):1308–1314.

[Winter et al., 2013] Winter, J., Mayer, S., Kaimer, S., Seitz, P., Pagenkopf, J., and Streit, S. (2013). Inductive power supply for heavy rail vehicles. In *Electric Drives Production Conference (EDPC), 2013 3rd International*, pages 1–9. IEEE.

[Wu et al., 2011] Wu, H. H., Gilchrist, A., Sealy, K., Israelsen, P., and Muhs, J. (2011). A review on inductive charging for electric vehicles. In *Electric Machines & Drives Conference (IEMDC), 2011 IEEE International*, pages 143–147. IEEE.

[Wu et al., 2012] Wu, H. H., Gilchrist, A., Sealy, K. D., and Bronson, D. (2012). A high efficiency 5 kw inductive charger for evs using dual side control. *IEEE Transactions on Industrial Informatics*, 8(3):585–595.

[Wu and Masquelier, 2015] Wu, H. H. and Masquelier, M. P. (2015). An overview of a 50kw inductive charging system for electric buses. In *Transportation Electrification Conference and Expo (ITEC), 2015 IEEE*, pages 1–4.

[Yilmaz and Krein, 2013] Yilmaz, M. and Krein, P. T. (2013). Review of battery charger topologies, charging power levels, and infrastructure for plug-in electric and hybrid vehicles. *IEEE Transactions on Power Electronics*, 28(5):2151–2169.

Curriculum Vitae

Personal Data

Name	Ugaitz Iruretagoyena Alustiza
Date of Birth	28.02.1990
Nationality	Spanish
Citizen of	Bergara, Gipuzkoa, Spain
Contact	uiruretagoyena@ikerlan.es

Education

2014-2018	**PhD Thesis** "Desing and Optimization of a Three Phase Inductive Power Transfer System" under the supervision of Prof. Hartiza Camblong and Dr. Irma Villar in the Power Electronics Area at IK4-IKERLAN research center in collaboration with EHU/UPV.
2013-2014	**Master Thesis** "Analysis, simulation and development of an induction based heating system" in the Power Electronics Area at IK4-IKERLAN research center in collaboration with Mondragón Unibertsitatea.
2012-2014	**Master** in Energy and Power Electronics in Mondragón Unibertsitatea, Mondragón Spain.

2011-2012	**Bachelor Thesis** "Characterization, modeling and simulation of a solar panel" in Mondragón Unibertsitatea, Mondragón Spain.
2008-2012	**Bachelor** in Industrial Electonics Engineering in Mondragón Unibertsitatea, Mondragón Spain.

Work Experience

2018-present	**Researcher** at the Power Electronics Area, IK4-IKERLAN research center, Mondragón, Spain.
2015 (Jan.-Jul.)	**PhD guest** at the Power Electronics Systems department, ETH, Zürich, Switzerland.
2014-2018	**PhD assistant** at the Power Electronics Area, IK4-IKERLAN research center, Mondragón, Spain.
2012-2014	**Research assistant** at the Power Electronics Area, IK4-IKERLAN research center, Mondragón, Spain.

Languages

Basque	Native
Spanish	Native
English	Advanced, C1 level (University of Cambridge certificate)

eman ta zabal zazu

Universidad del País Vasco
Euskal Herriko Unibertsitatea

RESUMEN TESIS DOCTORAL

Diseño y Optimización de un sistema Trifásico de Transferencia de Potencia Inductiva

Presentada por: **Ugaitz Iruretagoyena Alustiza**

Supervisada por: Dr. Haritza Camblong (UPV-EHU) y
Dr. Irma Villar (IK4-IKERLAN)

El concepto de transporte sostenible dentro de las ciudades debe ser reconsiderado para poder así tener áreas urbanas más saludables. Es un hecho bien conocido que en las grandes ciudades sufren de grandes problemas de contaminación. Principalmente, debido a los vehículos de combustión interna, con grandes emisiones de CO_2. Estos representan más del 50% de los vehículos utilizados diariamente. Es por ello que el transporte público debe ser estimulado. Particularmente hablando, el transporte ferroviario es muy atractivo, ya que no se producen emisiones directas.

Los sistemas de transporte ferroviario, como los tranvías y los metros, son muy ventajosos en términos de eficiencia, precio del usuario, seguridad y comodidad. Sin embargo, en comparación con un vehículo de combustión interna, los costos iniciales y de mantenimiento son muy altos. El alto costo inicial se debe principalmente al precio de las baterías. Por otro lado, el mantenimiento se ve enormemente afectado por la corrosión y la exposición ambiental que sufre parte del sistema de alimentación, el pantógrafo y las catenarias, siendo estos los componentes más críticos. Además, en las grandes ciudades, con muchas líneas de tranvía, las catenarias tienen un gran impacto visual. Para

solucionar estos problemas, una de las opciones más prometedoras es dotar al vehículo ferroviario de un sistema de transferencia inductiva (IPT). De esta forma, la catenaria podría eliminarse y la carga se realizará de forma inalámbrica con las bobinas del transmisor enterradas en el suelo.

Entre los diferentes sistemas posibles de IPT, este trabajo se centra en los sistemas de transferencia de energía inductiva dinámica (DIPT), es decir, cuando se está cargando mientras el vehículo se está moviendo. En concreto, esta tesis se adentra en el diseño de bobinas tipo meandro. El objetivo de este trabajo es proponer un método para diseñar sistemas de carga inductiva trifásicos.

CAPÍTULO 1. Introducción

El objetivo de este capítulo es el de, por un lado, presentar el contexto y la motivación por el cual se observa el gran potencial de los sistemas de transferencia de energía inductivos como incentivo para la irrupción de los vehículos eléctricos en el mercado actual y por otro lado, en análisis de los trabajos que actualmente se están realizando en esta temática tanto en las universidades como en la industria.

A pesar del creciente número de vehículos eléctricos (EV por sus siglas en inglés), el número absoluto de EV todavía está lejos de los vehículos de combustión interna (ICE). Los EV representan menos del 1% de la cuota total de mercado. En las dos economías más grandes del mundo, el EV representa el 0,7% en los Estados Unidos y el 1% en China del total de automóviles vendidos en 2015. En otros países tecnológicamente punteros, como Japón y Corea del Sur, la cuota de mercado es aún menor, siendo de 0.6% y de 0.2% respectivamente. Solo cuatro países superan la barrera del 1% en el mundo, Dinamarca con un 2,2%, Suecia con un 2,4%, los Países Bajos con un 9,7% y en una posición destacada Noruega con un 23,3%.

La razón detrás de esta diferencia entre los países escandinavos y el resto del mundo no es tecnológica, sino principalmente económica. La razón viene del alto precio de compra de vehículos eléctricos. Aunque en el largo plazo los EV son amortizados, dado que los costos de combustible se reducen al mínimo, el costo inicial es considerablemente mayor, lo que persuade su venta. En países como Noruega, los gobiernos están imponiendo políticas fiscales que benefician a las tecnologías

respetuosas con el medio ambiente, reduciendo los impuestos, otorgando fondos con condiciones beneficiosas y penalizando a los grandes contaminantes.

Por lo tanto, para impulsar aún más la irrupción del EV en el resto de los países, se deben abordar tres cuestiones:

- Reducción del costo inicial
- Aumento del kilometraje
- Mejora en comodidad del proceso de carga

Se puede observar que los principales inconvenientes de los EV están relacionados principalmente con el sistema de almacenamiento, es decir, las baterías. Su capacidad de almacenamiento de energía es baja (en comparación con la gasolina), necesitan un largo período para cargarse completamente y son caros. Por estos motivos, las recientes investigaciones se centran en este elemento en particular, ya sea mejorando la batería en sí (mejor química) o reduciendo su uso (otras fuentes de suministro, por ejemplo, hibridación).

La transferencia de energía inductiva puede ser la solución a los problemas antes mencionados. El precio de compra de los EV se vería disminuido considerablemente, ya que parte de las baterías podrían reemplazarse por una bobina receptora, mucho más barata. El automóvil no necesitará llevar toda la energía necesaria, después de todo, podría cargarse en cualquier parada, por ejemplo, semáforos, estacionamientos ... Este término se conoce en la literatura como *carga oportuna*. Por lo tanto, el problema del kilometraje también se vería resuelto parcialmente. Mientras haya puntos de carga, el rango puede considerarse infinito. Finalmente, también se mejorará el proceso de carga. El usuario no necesitará enchufar el vehículo. Colocar el automóvil sobre la bobina del transmisor iniciaría automáticamente el proceso de carga.

Para los sistemas IPT estáticos, desde el punto de vista del diseño, la academia está buscando formas de reducir el tamaño y las emisiones magnéticas y aumentar la eficiencia del equipo receptor, ya sea mejorando el diseño magnético con estructuras de bobina mejoradas, como bobinas *Double-D* (DD), o alternativamente, buscando la mayor densidad de potencia del convertidor. Se afirma que las soluciones IPT

estáticas actuales para una eficiencia similar, requieren bobinas 10 a 100 veces menores en comparación con los sistemas de hace 15 años.

La tendencia con respecto a la carga dinámica de IPT (denominado D-IPT) ha tomado dos caminos claramente definidos. Por un lado, están los sistemas segmentados o distribuidos. Aquí, los sistemas se construyen concatenando topologías de carga estáticas, creando un carril de carga. Cada una de las bobinas es encendida cuando la bobina receptora, es decir, el vehículo, cuando se coloqua encima. Es por ello que la mayor parte de la investigación se centra en el control y no tanto en el diseño de estos sistemas. Por otro lado, las soluciones de bobina única extienden el tamaño de la bobina del transmisor para que la bobina receptora siempre esté dentro del campo magnético. En este caso, la bobina del transmisor siempre entregará energía independientemente de donde se coloque la bobina receptora, sólo si el receptor está dentro del campo magnético. En este último caso, la investigación es similar a la de los cargadores estáticos, maximizar eficiencia y reducir el campo magnético.

En la industria, aparte de tener los mismos objetivos que la academia, la alta densidad de potencia y la eficiencia, se le añade la reducción del coste. Todas las soluciones se basan en tecnologías establecidas. El tipo de convertidor es siempre un puente completo y los dispositivos SiC no se utilizan, debido a su alto precio en comparación con los semiconductores Si. Se han reportado sistemas de carga inalámbrica superiores a 50kW con eficiencias próximas al 90%.

CAPÍTULO 2. Principios de la transferencia de energía inductiva

En el segundo capítulo se introducen los principios básicos de la transferencia de potencia inductiva. El objetivo de este capítulo es trasladar de manera comprensiva el conocimiento de la carga por conducción a la carga inalámbrica.

Para ello la primera sección empieza detallando los principios básicos del transformador. En esta sección se muestran las distintas características que comparten los transformadores con los cargadores inalámbricos. Por un lado está la bobina transmisora, denominado primario. La bobina crea un campo magnético que circula por un núcleo. Este campo magnético atraviesa el bobinado receptor, denominado secundario, en

el cual se induce una tensión. Este mismo efecto es el utilizado para transferir energía en un IPT; con la diferencia de que en vez de tener un núcleo, el campo magnético circula por el aire. Por esta razón, el circuito equivalente es compartido por las dos tecnologías. En el segundo apartado de este capítulo, el circuito equivalente T es presentado. Este circuito modela tanto la energía transferida (con la inductancia magnetizante) como la desperdiciada (con las inductancias de fugas).

Una vez presentado el circuito equivalente, en la próxima sección se aborda la descripción de los cargadores conductivos aislados (ICC por sus siglas en ingles). Como es sabido, aumentar la frecuencia reduce el tamaño de los elementos magnéticos. Es por ello que en los ICC se trabaja en el rango de los kHz para poder así reducir el tamaño del transformador. Para cambiar e incrementar la frecuencia de trabajo se utilizan convertidores electrónicos. En esta tesis se analiza el funcionamiento del 'single active bridge'. Este circuito consta de un inversor 'full-bridge' conectado al primario y de un puente a diodos en el secundario. Para modelar el sistema, se obtienen las ecuaciones en Fourier. Se describe la modulación cuadrada y se muestran las formas de onda.

Una vez analizados los ICC, en la siguiente sección se traslada el análisis a los sistemas de transferencia de energía por inducción. Primero se presenta y analiza el circuito equivalente de tensiones. Aunque el modelo y las equaciones sean las mismas, los sistemas IPT se pueden analizar más fácilmente con este circuito. En vez de tener una inductancia de fugas y una magnetizante como en el circuito equivalente T, en este caso el modelo describe la inductancia propia y la mutual.

Ya que en los sistemas IPT el acoplamiento entre las bobinas es mucho más bajo, se observa que para el mismo circuito analizado en el ICC, la potencia transferida es mucho menor. Es por ello que es necesario añadir un condensador y así convertir el circuito en un sistema resonante. En los sistemas IPT las cuatro topologías de compensación más comunes son la serie-serie, serie-paralelo, paralelo-serie y la paralelo-paralelo. Para este caso, al ser la alimentación una fuente de tensión y no de corriente, solamente las compensaciones serie-serie y serie-paralelo se pueden utilizar.

El la siguientes dos secciones, se aborda el análisis de los sistemas de compensación serie-serie y serie-paralelo. Se observa que existen límites de potencia y de acoplamiento que hacen que el sistema tenga más de

una resonancia. Este efecto es conocido como 'pole-splitting' o bifurcación. Si un sistema tiene bifurcación, la impedancia que ve el inversor puede ser capacitiva aunque se trabaje por encima de la frecuencia de resonancia. Como es sabido, trabajar en zona capacitiva hace que aumenten las pérdidas de encendido considerablemente, reduciendo así la eficiencia. Por ello, es muy importante que un sistema IPT este diseñado de tal manera que no haya bifurcación. En este apartado se derivan donde están los limites de potencia y de acoplamiento y además se añade un límite más, el ratio de inductancias. Se demuestra que dependiendo de las tensiones de trabajo y el ratio de las inductancia el sistema puede tener bifurcación aunque se trabaje con un acoplamiento muy bajo.

Una vez analizado la bifurcación, en la siguiente sección, se analiza la conmutación en cero tensión (ZVS). Se calcula el límite de tiempo muerto y de corriente necesaria para descargar el condensador de salida y así reducir las pérdidas.

El análisis realizado se valida en un prototipo de 3.3kW. Este prototipo es forzado a trabajar en bifurcación y se observa como la mayor eficiencia se obtiene por debajo de la frecuencia de resonancia.

En la última sección de este capítulo se aborda el análisis de las pérdidas en los distintos componentes. Primero se analizan las pérdidas en la transmisión de energía. Es decir, las pérdidas en el hilo de las bobinas, las ferritas, en el aluminio y en los condensadores. Finalmente, se analizan las pérdidas en el inversor, tanto las de conducción como las de conmutación, considerando dos tecnologías de semiconductor silicio y silicio carburo.

CAPÍTULO 3. Sistemas de transferencia de energía inductiva trifásica

Una vez que se han presentado los conceptos básicos de los sistemas IPT monofásicos, en el capítulo 3 se analiza el sistema IPT trifásico dinámico utilizando bobinas de tipo meandro.

En la primera sección se analizan los principios de funcionamiento de las bobinas tipo meandro. Se observa que a lo largo del bobinado el campo magnético es sinusoidal. Lo que conlleva que la inductancia mutua vista por un receptor, sea también sinusoidal.

Sabido esto, se analiza la opción de tener más de una fase. Se verifica que al construir la bobina transmisora con más de tres fases y alimentando cada bobina con una corriente equilibrada, la tensión inducida es la misma para cada posición. Es decir, la transferencia de energía es uniforme a lo largo del bobinado.

En la siguiente sección se analiza el funcionamiento de un sistema con tres bobinas transmisoras. Se deduce que es necesario también utilizar tres bobinas receptoras para que el sistema sea equilibrado. Para ello se opta por una representación matricial de las ecuaciones. Se comprueba que el sistema trifásico puede ser modelado como un sistema monofásico con una inductancia mutua 1.5 veces mayor.

Una vez obtenido este resultado se analiza el sistema SAB trifásico. Al tener una carga equilibrada este inversor también puede ser modelado como una única rama. Por lo tanto el desarrollo llevado a cabo en el anterior capítulo, con unas pequeñas adaptaciones, sirve también para analizar el sistema trifásico.

En la siguiente sección, se vuelve a analizar las compensaciones serie-serie y serie-paralelo para el sistema trifásico. Una vez más se observa que la problemática de la bifurcación también aparece. Por ello, se vuelven a calcular los límites de potencia, acoplamiento y ratio de inductancias, teniendo en cuenta que también existe acoplamiento entre las propias bobinas transmisoras y entre las propias bobinas receptoras.

Finalmente, en el último apartado de este capítulo se presenta un procedimiento para poder diseñar un sistema de transferencia de potencia inductiva trifásica. La cual es aplicada y experimentalmente verificada en un prototipo de pequeña escala de 50W a 100kHz y una distancia entre las bobinas transmisoras y receptoras de 50mm. Se observa que, aunque existan pequeñas variaciones en las corrientes, la potencia transferida es uniforme a lo largo de toda la bobina, con una eficiencia de aproximadamente 70%.

CAPÍTULO 4. Diseño, optimización y validación experimental de un sistema de transferencia inductiva trifásica de 9kW

Los cálculos presentados en el capítulo anterior formarán la base para la optimización del sistema de IPT trifásico de 9kW desarrollado en este capítulo. En comparación con el prototipo anterior de 50W

donde todas las dimensiones se definieron previamente y solo el número de vueltas del transmisor y las bobinas receptoras se calcularon, en este nuevo diseño se analizan diferentes aspectos como el tamaño de la bobina, la ventana de la bobina y el número de núcleos de ferrita .

En la primera sección de este capítulo se analizan distintos métodos de optimización: a priori, progresivos y a posteriori. Al usar los métodos *a priori* o *progresivos*, cualquier formulación multiobjetivo con muchos indicadores de rendimiento se puede convertir en un problema con un único objetivo. Luego, la optimización encontrará una solución óptima única, que dependerá de los valores asignados a los factores de ponderación. Establecer esos factores de ponderación no siempre es una tarea fácil y depende en gran medida de la aplicación y la experiencia del diseñador. Por otro lado, al usar el método *a posteriori*, es decir, la optimización de Pareto-Front, se presentan todas las soluciones factibles y la selección óptima se realiza después, conociendo toda la información. El Pareto-Front es la línea o superficie que repesenta toda las soluciones óptimas. Para mejorar un indicador de rendimiento, otro empeora. Teniendo esto en cuenta, se opta por utilizar el Pareto-Front como método de optimización. Para ello se crea un diagrama de flujo, siendo los indicadores la eficiencia, el peso, el tamaño, el coste y las tensiones de las bobinas.

Este diagrama de flujo es aplicado en la optimización de un sistema IPT trifásico de 9kW/100kHz y una distancia entre las bobinas transmisoras y receptoras de 100mm. Siguiendo el mismo procedimiento que en el capitulo anterior, primero se calculan tanto las corrientes, tensiones y la inductancia mutua requerida para transmitir la potencia deseada. Una vez hecho esto, se selecciona el hilo que minimice las perdidas en el bobinado.

En la siguiente sección se muestran los Pareto-Front obtenidos en la simulación. Se observa que las soluciones más eficientes son las que tienen el mayor número de núcleos de ferrita. Se producen dos efectos principales agregando más núcleos. Por un lado, con más núcleos hay un mejor uso del campo magnético, es decir, más campo llega a la bobina receptora. Esto implica que el acoplamiento se mejore. Por otro lado, aparte de la reducción de pérdida en el bobinado, el campo que atraviesa los núcleos está mejor distribuido, por lo que las pérdidas en las ferritas también se reducen. Como consecuencia, la eficiencia es claramente mejorada. Otra ventaja importante de aumentar el

acoplamiento, y como resultado la disminución del número de vueltas en la bobina receptora, es la reducción del voltaje generado en los terminales de la bobina. Sin embargo, añadir ferritas también tiene algunos inconvenientes. Entre ellos, el más notable es el aumento de peso. La contribución de peso más significativa para todo el sistema proviene de los núcleos de ferrita. Agregar demasiados núcleos hace que el sistema sea mucho más pesado. Teniendo en cuenta que se trata de un sistema embarcado, es un gran hándicap. Además del inconveniente de peso, agregar más núcleos de ferrita encarece el sistema. Al final, el costo está estrechamente asociado a la cantidad del material que se está utilizando. Por ello, se decide analizar el sistema ponderando los factores equitativamente. La solución escogida no es la mejor ni la peor en ningún indicador, pero tiene muy buenas prestaciones en todos ellos.

Posteriormente, se procede a diseñar el sistema en detalle: banco de condensadores, aislamiento, materiales ...

Una vez diseñado el sistema, en la última sección, se valida experimentalmente el prototipo. Se observa que el sistema está demasiado cerca de la frecuencia de resonancia, esto hace que la corriente de conmutación no sea suficiente para descargar el condensador de salida de los MOSFET. Por ello, se decide aumentar la frecuencia de resonancia de 100kHz a 104kHz, siendo este a su vez el punto de operación más eficiente. Finalmente, se valida el funcionamiento del sistema para distintas potencias y distintas posiciones del receptor. Se observa como la eficiencia se mantiene prácticamente constante para todo el rango de operaciones, siendo su valor aproximadamente del 90%.

Como conclusión general se puede decir que el trabajo desarrollado a lo largo de esta tesis ha contribuido al desarrollo de los sistemas de carga inductiva dinámica. Se ha demostrado que los sistemas trifásicos con bobinados tipo meandro son capaces de transmitir potencia constante a lo largo de todo el bobinado, lo que simplifica al máximo el control. Además se ha propuesto una metodología de optimización teniendo en cuenta factores como la eficiencia, peso y costo. Finalmente se ha demostrado el potencial en un prototipo funcional de 9.2kW con una eficiencia del 90%.